Article:

Walkley, B. orcid.org/0000-0003-1069-1362 and Provis, J.L. orcid.org/0000-0003-3372-8922 (2019) Solid-state nuclear magnetic resonance spectroscopy of cements. Materials Today Advances, 1. 100007. ISSN 2590-0498

https://doi.org/10.1016/j.mtadv.2019.100007

Materials Today Advances 1 (2019) 100007

Contents lists available at ScienceDirect

Materials Today Advances

journal homepage: www.journals.elsevier.com/materials-today-advances/

Solid-state nuclear magnetic resonance spectroscopy of cements

B. Walkley**, J.L. Provis*

Department of Materials Science and Engineering, The University of Sheffield, Sheffield S1 3JD, United Kingdom

ARTICLE INFO

Article history:
Received 19 January 2019
Received in revised form
22 March 2019
Accepted 26 March 2019
Available online 3 May 2019

Keywords:
Solid-state NMR spectroscopy
Portland cement
Calcium aluminate cements
Calcium sulfoaluminate cements
Magnesia-based cements
Alkali-activated cements

ABSTRACT

Cement is the ubiquitous material upon which modern civilisation is built, providing long-term strength, impermeability and durability for housing and infrastructure. The fundamental chemical interactions which control the structure and performance of cements have been the subject of intense research for decades, but the complex, crystallographically disordered nature of the key phases which form in hardened cements has raised difficulty in obtaining detailed information about local structure, reaction mechanisms and kinetics. Solid-state nuclear magnetic resonance (SS NMR) spectroscopy can resolve key atomic structural details within these materials and has emerged as a crucial tool in characterising cement structure and properties. This review provides a comprehensive overview of the application of multinuclear SS NMR spectroscopy to understand composition–structure–property relationships in cements. This includes anhydrous and hydrated phases in Portland cement, calcium aluminate cements, calcium sulfoaluminate cements, magnesia-based cements, alkali-activated and geopolymer cements and synthetic model systems. Advanced and multidimensional experiments probe ^{1}H, ^{13}C, ^{17}O, ^{19}F, ^{23}Na, ^{25}Mg, ^{27}Al, ^{29}Si, ^{31}P, ^{33}S, ^{35}Cl, ^{39}K and ^{43}Ca nuclei, to study atomic structure, phase evolution, nanostructural development, reaction mechanisms and kinetics. Thus, the mechanisms controlling the physical properties of cements can now be resolved and understood at an unprecedented and essential level of detail.

1. Introduction

Modern society is heavily reliant on cementitious materials in constructing our built environment. Second only to water in terms of commodity use [1,2], the worldwide production of concrete exceeds 10 billion tonnes per annum. The most common cement used to produce concrete is Portland cement (PC) [3], a complex material made up of multiple calcium-rich mineral phases that react with water and harden to provide strength, impermeability and resistance to thermal, mechanical and chemical stresses over long timescales [4]. The excellent physical properties of PC have resulted in its incorporation into virtually all of the modern built environment.

However, PC production results in large associated CO_2 emissions, approximately 0.73–0.99 t CO_2/t PC, which is ~8% of current global anthropological CO_2 emissions when considering a PC production volume around 4 Gt per annum [5,6]. Consequently, low-CO_2 cementitious materials have emerged as attractive, more sustainable alternatives to PC [4]. Supplementary cementitious materials (SCMs) such as coal fly ash (FA), blast furnace slag, calcined clays, finely ground limestone and silica fume are widely used in concrete. By blending PC with SCMs, it is possible to enhance and control physical properties, e.g. strength, durability, phase formation and reaction kinetics, and also to improve sustainability by reducing associated CO_2 emissions and valorising industrial wastes [7]. PC-free binders such as calcium aluminate cements (CACs) and calcium sulfoaluminate (CSA) cements, magnesia-based cements, alkali-activated materials (AAMs) and geopolymers, among others, have also received significant attention from academia and industry due to the enhanced technical properties and/or sustainability that they can provide, when compared with PC [4].

The complex chemical nature of cement systems, which often involve crystallographically disordered phases and which continue to evolve as a function of time for many years after initial mixing, has caused significant difficulty in understanding their atomic structure. Nuclear magnetic resonance (NMR) spectroscopy has become a key tool which offers the opportunity to clarify many of these important structural details. NMR spectroscopy involves the detection of interactions between nuclei with intrinsic magnetic

---

* Corresponding author.
** Corresponding author.
E-mail addresses: b.walkley@sheffield.ac.uk (B. Walkley), j.provis@sheffield.ac.uk (J.L. Provis).

https://doi.org/10.1016/j.mtadv.2019.100007

moments (i.e. non-zero spin) and applied magnetic fields and enables determination of the local chemical environments of NMR-active nuclei, regardless of the level of crystallographic order or disorder, and this is essential in its application to the study of cements. In cements, nuclei of interest include ^{1}H, ^{13}C, ^{17}O, ^{19}F, ^{23}Na, ^{25}Mg, ^{27}Al, ^{29}Si, ^{31}P, ^{33}S, ^{35}Cl, ^{39}K and ^{43}Ca (Table 1). Solid-state (SS) NMR is ideally suited to study both anhydrous and hydrated solid phases in cementitious materials. Its application to cement samples of different ages is invaluable in resolving the reaction mechanisms, kinetics and structural evolution that dictate the properties and performance of cements (and thus also concretes made using these cements). NMR can also be applied as a powerful tool probing the dynamics of mobile ions and water within cementitious materials, in particular through the use of ^{1}H NMR relaxometry which provides information about water mobility and pore size distribution [8,9]. These various applications and nuclei will be discussed in detail in the sections which follow.

2. Solid-state NMR spectroscopy

An NMR experiment involves holding a sample in a magnetic field (denoted B_0) and applying pulses of radiofrequency radiation to induce precession of the nuclear spin and measuring the electromagnetic response produced as the nuclei relax back to their equilibrium states. The electromagnetic signal is measured as a free induction decay, which is then converted to an NMR spectrum by applying a Fourier transform. The NMR spectrum contains resonances characteristic of near-neighbour atomic environments [10,11]. Terms representing the magnetic dipolar interaction, chemical shielding and quadrupolar interactions between the nucleus and its environment are of particular interest in the study of cements.

NMR spectra of solids are broadened (compared to those of liquids) due to dipolar interactions, anisotropy of the chemical shielding and quadrupolar interactions between the intrinsic nuclear electric quadrupolar moment and the surrounding electric field gradient [10]. This necessitates the application of sample spinning methods to reduce broadening.

Magic angle spinning (MAS) requires spinning a sample at an angle of $\cos^2(\theta_{MAS}) = 1/3$ ($\theta_{MAS} \approx 54.74°$) with respect to the static magnetic field (B_0) so that dipolar interactions are suppressed, and both chemical shielding anisotropy and first-order quadrupolar interactions are removed [10,11], narrowing spectral lineshapes. This means that the local chemical environments of spin $S = ½$ nuclei (which do not experience second-order quadrupolar interactions) can be represented in terms of the isotropic chemical shift (δ_{iso}) in MAS NMR spectra. Quadrupolar nuclei ($S > ½$) experience additional second-order quadrupolar interactions, so the quadrupolar interaction term of the Hamiltonian is non-zero under MAS conditions. This limits spectral resolution due to anisotropic broadening of the signals. However, these second-order quadrupolar interactions are inversely proportional to the strength of B_0 and can thus be reduced through the use of high magnetic fields [10,11]. Owing to the disordered structure of many cementitious phases, significant line broadening occurs at all practically achievable MAS rates, and so the spectra for relevant nuclei are often poorly resolved. This is exacerbated in quadrupolar nuclei such as ^{17}O ($S = 5/2$), ^{23}Na ($S = 3/2$), ^{25}Mg ($S = 5/2$), ^{27}Al ($S = 5/2$), ^{33}S ($S = 3/2$), ^{39}K ($S = 3/2$), and ^{43}Ca ($S = 7/2$) [12].

The presence of paramagnetic species within cementitious materials can limit the applicability of SS NMR for their characterisation; these species influence the relaxation and chemical shift of nearby nuclear spins, which can severely dampen and shift the NMR signal of these nuclei [10]. This is particularly problematic in standard ‘grey’ PC and in ferrite-containing sulfoaluminate cements, which each contain tetracalcium aluminoferrite ($4CaO \cdot Al_2O_3 \cdot Fe_2O_3$, C_4AF), as well as in binders containing coal FA (containing Fe_2O_3) [13]. The use of Fe_2O_3-free cement systems for spectroscopic analysis [14–16] can, therefore, be advantageous.

Recent advances in this understanding of the chemistry and materials science of cements, in which the application of SS NMR has played a pivotal role, are discussed in the following section.

3. Terminology used in defining the local structure of silicates and aluminates

Si sites are generally identified using notation of the type $Q^n(m\mathrm{Al})$ with $0 \le m \le n \le 4$, where Si in tetrahedral coordination (represented by Q) is bonded to n other tetrahedral atoms (m of which are Al) via oxygen bridges. $Q^n(m\mathrm{Al})$ Si sites within cementitious materials typically resonate in the region from −60 ppm to −120 ppm relative to tetramethyl silane, with significant overlap between the broad resonances observable in disordered solid phases, but a more negative chemical shift induced by a higher connectivity (i.e. higher n) (Fig. 1) [11,16–18]. Each additional tetrahedral Al atom which replaces an Si neighbouring a $Q^n(m\mathrm{Al})$ silicon site also increases the chemical shift by approximately 5 ppm [11], and this provides an important point of differentiation between $Q^n(m\mathrm{Al})$ sites as a function of n and m, although the effects of the two parameters cannot always straightforwardly be discriminated without application of multinuclear NMR techniques.

Aluminium sites are generally differentiated by the coordination number, with tetrahedral Al species identified using q^n notation, where q represents Al in tetrahedral coordination linked to n tetrahedral silicon sites via oxygen bridges, and $0 \le n \le 4$. Bridges between two tetrahedral Al sites are disfavoured (a crystallographic and thermodynamic observation known as ‘Loewenstein's principle’ [19]). Tetrahedral and octahedral Al sites typically resonate within the regions 80–50 ppm and 20 - 0 ppm, respectively, relative to $Al(H_2O)_6^{3+}(aq)$, while resonances assigned to five-coordinated Al and highly distorted tetrahedral Al environments have been observed in the region 50–20 ppm, Fig. 2 [11,17,20–22].

4. Characterisation of cementitious materials

4.1. MAS NMR of anhydrous cementitious materials

4.1.1. Portland cement

PC primarily comprises the ‘clinker’ phases tricalcium silicate ($3CaO \cdot SiO_2$, C_3S, in numerous polymorphs), dicalcium silicate ($2CaO \cdot SiO_2$, C_2S; the α and β polymorphs of this composition are preferred in cements due to their hydraulic nature, whereas γ-C_2S is unreactive), tricalcium aluminate ($3CaO \cdot Al_2O_3$, C_3A) and tetracalcium aluminoferrite. This assemblage of clinker minerals is produced from limestone and silicate minerals in a rotary kiln, then rapidly cooled and interground with calcium sulphate to form PC [23]. Among these clinker minerals, tricalcium silicate (or a slightly impure form of this phase, containing Al and/or Mg among other substituents, which is commonly described as ‘alite’ in the cements literature [24]) is the predominant constituent of modern PC, defining its hydraulic nature and high early strength development upon cement hydration. The expected values of δ_{obs}, δ_{iso} and C_Q for different nuclei in various phases in PC are shown in Table 2 and discussed in the following text.

4.1.1.1. Tricalcium silicate (alite, hartrurite). C_3S is known to exist in seven polymorphs: three triclinic, three monoclinic and one trigonal. The alite present in PC crystallises from the melt in a trigonal form and upon rapid cooling, transforms into metastable

Table 1
Nuclei, associated key NMR parameters [437] and phases of interest in analysis of cement materials.

Isotope	Natural abundance (%)	Nuclear spin (*S*)	Magnetogyric ratio (γ) (10^7 rad/T.s)	Quadrupole moment (10^{28}Q/m^2)	Resonance frequency[a] (MHz)	Relative sensitivity[b]	Absolute sensitivity[b]	Relevant anhydrous phases[c]	Relevant hydrous phases[c]	Relevant cements
^{1}H	99.98	1/2	26.7519	0	500	1	1	Gypsum	C-S-H, C-A-S-H, C-(N,K)-(A)-S-H, (N,K)-A-S-H, CAH_{10}, C_2AH_8, C_3AH_6, AH_3, M-S-H, M-A-S-H, brucite, struvite-K, portlandite, AFt, AFm, third aluminate hydrate (TAH), hydrotalcite, hydrogarnets	PC, PC–SCM blends, SCMs, calcium aluminate cement (CAC), calcium sulfoaluminate (CSA)–containing cements, magnesia-based cements, alkali-activated materials (AAMs), geopolymers
^{13}C	1.108	1/2	6.7283	0	125.721	0.0159	0.000176	$CaCO_3$, gypsum	AFm, hydrotalcite	PC–SCM blends, SCM, AAM
^{17}O	0.037	5/2	−3.6279	−28	67.784	0.037	0.0000108	C_3S, β-C_2S, C_3A, C_4AF, $CaCO_3$, gypsum, slag, fly ash, metakaolin, silica fume, CA, CA_2, $C_{12}A_7$, ye'elimite, MgO	C-S-H, C-A-S-H, C-(N,K)-(A)-S-H, (N,K)-A-S-H, CAH_{10}, C_2AH_8, C_3AH_6, AH_3, M-S-H, M-A-S-H, brucite, struvite-K, portlandite, AFt, AFm, TAH, hydrotalcite, hydrogarnets	PC, PC–SCM blends, SCM, CAC, CSA, magnesia-based cements, AAM, geopolymers
^{19}F	100	1/2	25.181	0	470.385	0.83	0.83	C_3S, β-C_2S	–	PC
^{23}Na	100	3/2	7.0801	0.1	132.256	0.0925	0.0925	–	C-(N,K)-(A)-S-H, N-A-S-H	PC–SCM blends, SCM, AAM
^{25}Mg	10.13	5/2	−1.639	0.22	30.597	0.00267	0.000271	MgO	M-S-H, M-A-S-H, brucite, struvite-K, hydrotalcite	Magnesia-based cements
^{27}Al	100	5/2	6.976	0.15	130.287	0.21	0.21	C_3A, C_4AF, slag, FA, metakaolin, CA, CA_2, $C_{12}A_7$, ye'elimite	C-A-S-H, C-(N,K)-(A)-S-H, (N,K)-A-S-H, CAH_{10}, C_2AH_8, C_3AH_6, AH_3, M-A-S-H, AFt, AFm, TAH, hydrotalcite, hydrogarnets	PC, PC–SCM blends, SCM, CAC, CSA, magnesia-based cements, AAM, geopolymers
^{29}Si	4.7	1/2	−5.3188	0	99.325	0.00784	0.000369	C_3S, β-C_2S, slag, fly ash, metakaolin, silica fume	C-S-H, C-A-S-H, C-(N,K)-(A)-S-H, (N,K)-A-S-H, M-S-H, M-A-S-H, AFt, AFm, hydrogarnets	PC, PC–SCM blends, SCM, magnesia-based cements, AAM, geopolymers
^{31}P	100	1/2	10.841	0	202.404	0.0663	0.0663	C_3S, β-C_2S	–	PC
^{33}S	0.76	3/2	2.055	−57	38.348	0.00226	0.0000172	ye'elimite, gypsum	Ettringite, AFm	PC–gypsum blends, CSA
^{39}K	93.1	3/2	1.2498	0.049	23.333	0.000508	0.000473	–	C-(N,K)-(A)-S-H, K-A-S-H, struvite-K	AAM, geopolymers
^{43}Ca	0.145	7/2	−1.8025	0.2	33.641	0.0064	0.00000928	C_3S, β-C_2S, C_3A, C_4AF, $CaCO_3$, gypsum, slag, CA, CA_2, $C_{12}A_7$, ye'elimite	C-S-H, C-A-S-H, C-(N,K)-(A)-S-H, CAH_{10}, C_2AH_8, C_3AH_6, portlandite	PC, PC–SCM blends, SCM, CAC, CSA, AAM,

PC, Portland cement; NMR, nuclear magnetic resonance; SCM, supplementary cementitious material.

[a] At 11.744T (500 MHz for ^{1}H).

[b] Relative to ^{1}H = 1.00.

[c] In these columns and elsewhere in this article, cement chemistry abbreviations are used to represent oxide constituents: S, SiO_2; A, Al_2O_3; C, CaO; F, Fe_2O_3; N, Na_2O; M, MgO; H, H_2O; C, CO_2; \$, SO_3. AFt and AFm represent families of calcium aluminoferrite (AF) hydrates; AFm phases are the hydrocalumite-like ‘mono’ group and AFt phases are the ettringite-like ‘tri’ group. Hyphenation indicates a non-stoichiometric compound.

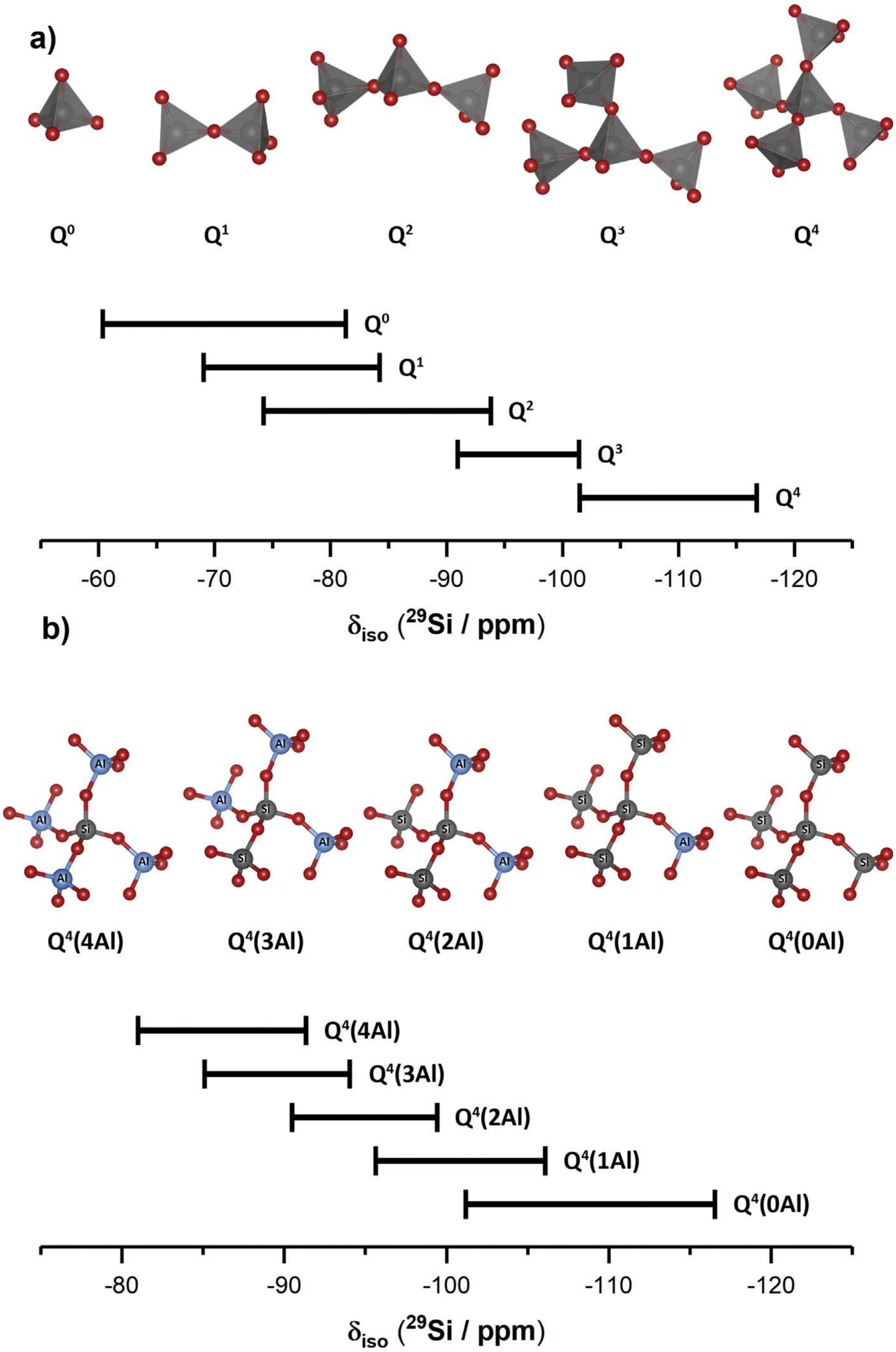

Fig. 1. Typical ranges of ^{29}Si chemical shifts for (a) Q^n and (b) Q^4(*m*Al) sites in solid silicates [11]. Si, Al and O atoms are represented by grey, blue and red spheres, respectively.

polymorphs, predominantly, the two monoclinic polymorphs M_I and M_{III} [25]. ^{29}Si MAS NMR analysis of the M_I polymorph of alite has shown that Si exists within nine crystallographically distinct sites, approximately within the range from −69 to −75 ppm [26,27], while ^{29}Si MAS NMR spectra of the M_{III} polymorph exhibit overlapping resonances between −66 and −78 ppm corresponding to eighteen distinct SiO_4 tetrahedra (Fig. 3) [27,28].

The calcium silicate chains in alite can accommodate a number of guest ions which substitute for silicon (e.g. AlO_4^{5-} or PO_4^{3-} for SiO_4^{4-} [30–32]) or oxygen (e.g F$^-$ for O^{2-} [31]). Substitution of AlO_4^{5-} for SiO_4^{4-} in C_3S chains has been identified crystallographically since the 1950s [24,33] and was first subjected to NMR analysis in 1994 by Skibsted et al. [34] using ^{27}Al MAS NMR [30], then later confirmed unambiguously using ^{27}Al multiple quantum (MQ)MAS NMR.

Reduction of the temperature at which alite forms, which is desirable for both economic and environmental reasons in cement production, is often achieved by adding ‘mineralising’ additives such as fluoride and phosphate, which substitute into the alite structure. Tran et al. [31] used ^{29}Si and ^{27}Al MAS, ^{19}F-^{29}Si cross polarisation (CP) MAS and ^{19}F-^{29}Si CP rotational-echo double-resonance (REDOR) MAS NMR techniques to show that F$^-$ substitutes for O^{2-} ions in the alite phase alone, according to a coupled substitution mechanism $SiO_4^{4-} + O^{2-} \rightarrow AlO_4^{5-} + F^-$ [35], with a

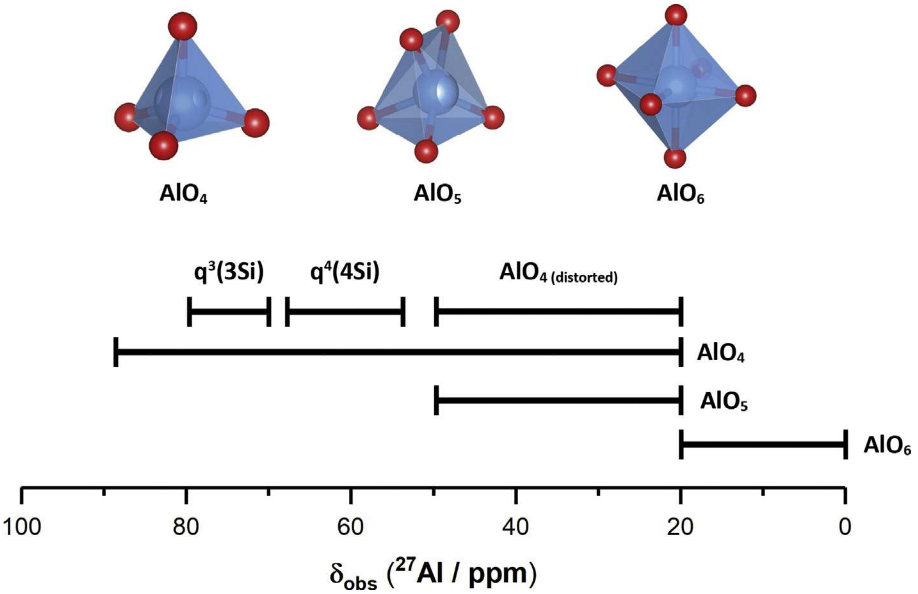

Fig. 2. Typical ranges of ^{27}Al chemical shifts for different aluminium sites in aluminates and aluminosilicates [11]. Al and O atoms are represented by blue and red spheres, respectively.

Table 2
Coordination states, δ_{obs}, δ_{iso} and C_Q for different nuclei in the major constituents of Portland cement.

Phase	Nucleus	Site	Coordination	δ_{obs} (ppm)	δ_{iso} (ppm)	C_Q (MHz)	Magnetic field (T)	Reference
Tricalcium silicate (C_3S)[a]	^{29}Si	Q^0 ($Si^{IV}{}_{1\text{-}9}$) in M_I	4	−69 to −75	−69 to −75	–	4.70, 7.5 and 8.45	[26,27]
		Q^0 ($Si^{IV}{}_{1\text{-}18}$) in M_{III}	4	−66 to −78	−66 to −78	–	7.5	[27]
	^{43}Ca	Ca in M_I	–	60–110	–	–	21.1	[38]
		Ca in M_{III}	–	60–110	–	–	21.1	[38]
Dicalcium silicate (β-C_2S)	^{17}O	Si-$\underline{\mathrm{O}}$-Ca (NBO)	2	116.2	116.2	–	11.7	[43]
	^{29}Si	Si-$\overline{(\mathrm{O}}$Ca$)_4$	4	−71.3	−71.3	–	7.5, 11.7	[27,42–44]
	^{43}Ca	Ca_1	–	–	33.7	2.41	21.1	[38]
		Ca_2	–	–	53.8	2.98	21.1	[38]
Tricalcium aluminate (C_3A)	^{27}Al	$Al^{IV}{}_1$	4	–	79.5	8.69	7.1, 9.4 and 11.7	[52]
	^{43}Ca	Ca	4	–	78.3	9.3	7.1, 9.4 and 11.7	[52]
Tetracalcium aluminoferrite (C_4AF)	^{27}Al	$Al^{IV}{}_1$	4	61–71	–	–	9.4	[55]
		$Al^{VI}{}_1$	6	0–20	–	–	9.4	[55]
Gypsum (C$\underline{\$}$$H_2$)	^{33}S	S	–	328	–	–	19.6	[59]
	^{43}Ca	Ca	–	−28	–	–	8.6	[40]

[a] M_I and M_{III} are the monoclinic polymorphs of alite comprising nine and eighteen crystallographically distinct Si sites, respectively.

strong preference for F^- substitution into interstitial oxygen sites not involved in covalent Si-O bonds. Poulsen et al. [32] showed via ^{31}P and inversion recovery ^{31}P MAS NMR that PO_4^{3-} ions substitute for SiO_4^{4-} tetrahedra in alite; a substitution level of 1.3 mol. % was identified in the sample studied. This substitution may be charge balanced by a coupled substitution mechanism where Ca^{2+} is partially replaced by Fe^{3+}, via $SiO_4^{4-} + 2Ca^{2+} \rightarrow PO_4^{3-} + Fe^{3+} + \square_{Ca}$ (where $\square_{Ca}$ represents a Ca^{2+} vacancy) [32]. Skibsted et al. [36] extended this work by applying ^{19}F-^{27}Al CP MAS and ^{19}Fe^{29}Si CP MAS NMR spectroscopy to a series of CaF_2-modified PCs containing between 0.23 and 0.77 wt% fluorine, demonstrating that increased fluorine content drives increased fluorine substitution into alite via a double substitution mechanism and that F^- and Al^{3+} ions in alite are likely to be clustered together.

Recently, ^{17}O–^{29}Si CP heteronuclear correlation (CP-HETCOR) MAS NMR was used to resolve oxide ion sites bonded to one Si^{4+} from those bonded to Ca^{2+} in synthetic tricalcium silicate for the first time [37]. Oxide ion sites bonded to Ca^{2+} play an important role in the structure and reactivity of C_3S but have proven difficult to resolve. ^{43}Ca MAS NMR analysis of alite was first reported by Moudrakovski et al. [38], with the high-field (21.14 T) natural abundance ^{43}Ca MAS NMR spectrum of the monoclinic polymorph showing a broad, asymmetric resonance consistent with overlapping ^{43}Ca resonances from the 36 non-equivalent sites for Ca in this phase and deviations from a perfect lattice (Fig. 4) [28]. This contrasts with the ^{43}Ca MAS NMR spectrum of the triclinic polymorph, which exhibited well-separated ^{43}Ca resonances despite the 29 non-equivalent sites for Ca in this phase [39], suggesting that some of these non-equivalent sites are quite similar. This work demonstrates the power of SS ^{43}Ca MAS NMR to resolve polymorphism, which is valuable in identification, characterisation and quantification of metastable polymorphs within cement systems, although the time and instrumentation required to collect high-resolution ^{43}Ca spectra may prove to be a limitation in a practical sense. Differences in ^{43}Ca MAS NMR spectra have also been exploited for spectroscopic analysis of the $CaCO_3$ polymorphs calcite, aragonite and vaterite [40,41], which are also present in many cement systems.

4.1.1.2. Dicalcium silicate (belite, larnite). The ^{29}Si and ^{17}O MAS NMR analysis of β-C_2S (also known as belite and the dominant polymorph of dicalcium silicate found in PCs) has shown that Si

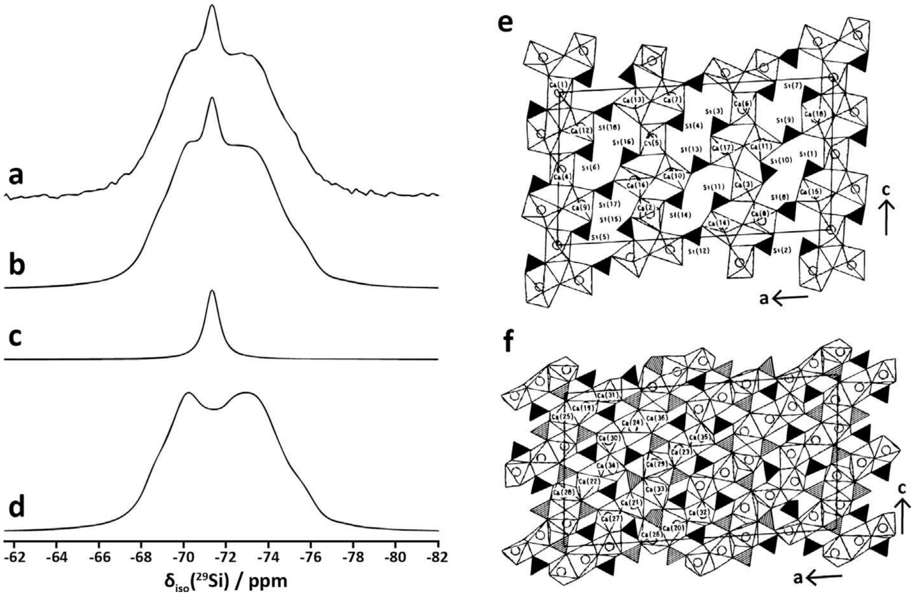

Fig. 3. ^{29}Si MAS NMR spectrum (9.4 T, spinning speed $\nu_R = 13.0$ kHz) of (a) grey PC and (b) its deconvolution, which is composed of the subspectra for belite and alite shown in (c) and (d). Adapted from Poulsen et al. [29]. Parts (e) and (f) show two different sections taken through the monoclinic superstructure of the M_{III} polymorph of alite, viewed down the *b* axis, showing polyhedra located in (e) and above (f) the a,0,c plane. Adapted from Nishi et al. [28].

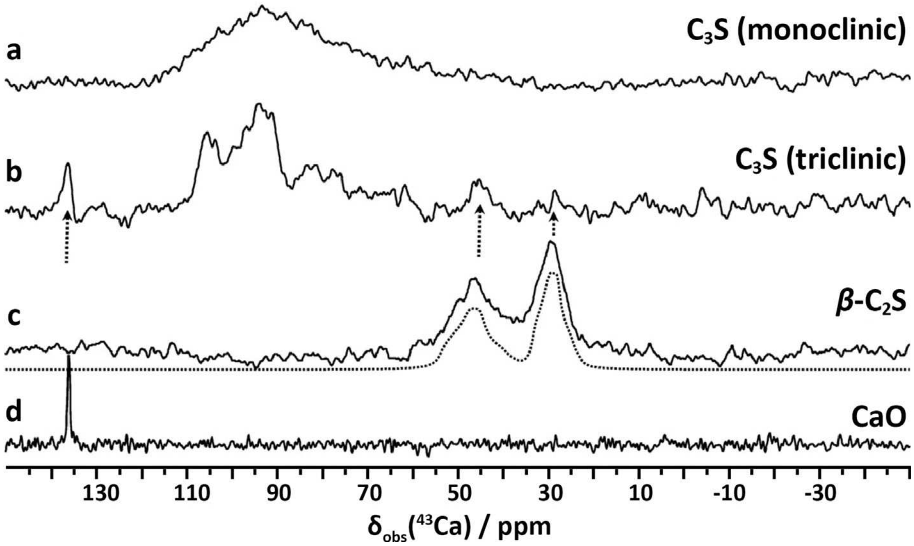

Fig. 4. Natural abundance ^{43}Ca MAS NMR spectra (21.4 T) of (a) monoclinic C_3S, (b) triclinic C_3S, (c) β-C_2S and (d) CaO. The dotted line below spectrum (c), for β-C_2S, shows the spectral simulation for the second-order quadrupolar interactions. The vertical arrows below spectrum (b), for triclinic C_3S, indicate the positions of the signals due to CaO and β-C_2S impurities. Adapted from Moudrakovski et al. [38].

exists within a single Q^0 (isolated SiO_4 tetrahedron) environment which exhibits a single ^{29}Si resonance at −71.3 ppm [27,42–44], coordinated to calcium via four Si-$\underline{O}$-Ca linkages [43]. Some PCs also contain the α polymorphs of C_2S, but these do not appear to have been analysed specifically by high-resolution SS NMR in the available body of literature, so the focus here will be on the β form.

Despite the fact that there are four crystallographically distinct oxygen sites within β-C_2S [42], a single broad resonance is observed in the ^{17}O MAS NMR spectrum [43], suggesting that there is some degree of disorder in this phase. As for the case of alite, substitution of Al^{3+} for Si^{4+} in C_2S has been identified crystallographically since the 1950s [45,46]. In 1994, ^{27}Al MAS NMR was used to provide the first detailed spectroscopic understanding of Al substitution for Si in C_2S in PC [30], which has significant consequences for the dissolution and hydration reactions of this phase, given the thermodynamic preference for dissolution of Al from calcium aluminosilicates [47]. Skibsted et al. [30] determined quadrupole coupling parameters and the isotropic chemical shift for this unique Al^{3+} guest ion in belite, which exhibited the most deshielded chemical shift ($\delta_{iso} = 96.1$ ppm) yet reported for a tetra-coordinated Al environment bonded to four oxygen atoms, further highlighting its potential importance in defining belite reactivity.

As in alite, tetrahedral Si sites within β-C_2S can accommodate both aluminium and phosphate ions [32,48]. Poulsen et al. [32] utilised ^{31}P and inversion recovery ^{31}P MAS NMR to show that PO_4^{3-} ions can substitute for SiO_4^{4-} tetrahedra in belite (in 2.1% of the

SiO_4^{4-} tetrahedra for the sample studied) in PCs containing between 0.08 and 0.45 wt % P_2O_5, with a similar coupled substitution charge balancing mechanism proposed as described previously for alite, where Ca^{2+} is partially replaced by Fe^{3+} via $SiO_4^{4-} + 2Ca^{2+} \rightarrow PO_4^{3-} + Fe^{3+} + \square_{Ca}$.

The ^{43}Ca MAS NMR spectrum of belite was first reported by Moudrakovski et al. [38], Fig. 4. The high-field (21.14 T) natural abundance ^{43}Ca MAS spectrum exhibited two distinct resonances consistent with the crystal structure of this phase and calculations from density functional theory (DFT) (Table 2). Both sites exhibited extensive asymmetry in Ca-O bond lengths.

4.1.1.3. Tricalcium aluminate. The investigation of C_3A by ^{27}Al MAS and MQMAS NMR at multiple fields has shown that it contains two inequivalent Al tetrahedral sites, which resonate at $\delta_{iso} = 79.5$ ppm and 78.25 ppm, respectively, arranged in six-membered rings of AlO_4 tetrahedra in the cubic (pure) polymorph of C_3A (Fig. 5) [34,49]. δ_{iso} values within ±6 ppm of those determined by Skibsted et al. [49] have also been reported for these Al^{IV} sites within C_3A by other workers, although with some variability in reported resonance positions [50–52]. Four of the six crystallographically nonequivalent calcium sites in C_3A were resolved using high-field (21.1 T) single-pulse 1D^{43}Ca MAS NMR by Moudrakovski et al. [38].

4.1.1.4. Tetracalcium aluminoferrite (brownmillerite). The analysis of C_4AF by NMR, and particularly by ^{27}Al MAS NMR, is constrained by the nuclear-unpaired electron dipolar couplings between the ^{27}Al nucleus and paramagnetic Fe^{3+} ions [53–55], which severely broaden the ^{27}Al MAS NMR spectra and dampen the signal [52,55] as demonstrated in a study by ^{27}Al MAS NMR (9.4T, $11.5 \leq \nu_R \leq 17.5$ kHz) [55], examining $Ca_2Al_xFe_{2-x}O_5$ with x = 0.93, 1 and 1.33 (Fig. 6). Increasing Fe content dramatically dampened and broadened the observed resonances, but despite these difficulties, it was possible to observe that the central transitions showed a dominant resonance for Al^{IV} species at $61 \leq \delta_{obs} \leq 71$ ppm, with increased shielding at higher Fe content, and Al^{VI} species at $0 \leq \delta_{obs} \leq 20$ ppm.

As mentioned in section 2, the presence of C_4AF in PC also has significant implications for acquisition of ^{29}Si MAS NMR data for C_3S and C_2S phases. A dramatic decrease in the longitudinal relaxation time, T_1, in grey PC has been attributed to the close proximity of these diamagnetic phases to paramagnetic C_4AF [56,57]. However, Poulsen et al. [29] attributed this effect primarily to Fe^{3+} ions incorporated as guest ions within C_3S and C_2S phases, rather than intermixing with ferrite phases. These effects need to be considered carefully when attempting to quantify C_3S and C_2S phases in PC via deconvolution of ^{29}Si MAS NMR spectra as preferential incorporation of Fe^{3+} ions within either of the silicate phases will result in a dampening of the ^{29}Si MAS NMR signal for that phase and consequently lead to incorrect quantification [57]. Further discussion of methods to mitigate this issue is provided in section 4.3.

4.1.1.5. Gypsum. Gypsum ($CaSO_4 \cdot 2H_2O$, $C\underline{\$}H_2$), and/or its partially dehydrated forms, is interground with PC clinker in small quantities to control the setting rate of the hydrating cement. During PC hydration, C_3A reacts with gypsum to form ettringite (AFt) which is subsequently converted (in part or in full) to monosulfoaluminate (AFm), starting a few hours after initial hydration [23]. In the absence of gypsum, C_3A would hydrate rapidly and setting could occur within minutes (i.e. 'flash setting').

The first application of NMR to any of the cement phases discussed in this article was undertaken by Pake, who in 1948 applied ^{1}H NMR to single crystals and powdered hydrates of gypsum, demonstrating that the splitting observed in the spectrum (the Pake doublet) reflects the dipolar coupling of two ^{1}H nuclei and therefore the internuclear distance between H atoms within the water molecules of gypsum [58]. Natural abundance ^{43}Ca MAS NMR (8.6 T, $\nu_R = 2$ kHz) has revealed a single Ca site in gypsum resonating at approximately $\delta_{obs} = -28$ ppm [40]. ^{33}S MAS NMR studies of gypsum (both natural abundance and enriched with ^{33}S) revealed a single S site in gypsum resonating at $\delta_{iso} = 328$ ppm (Fig. 7) [59]. However, it was noted that acquisition of natural abundance ^{33}S MAS NMR spectra for PC samples is not practical due to extremely long acquisition times, and consequently, this technique does not appear useful for field samples or those without isotopic enrichment.

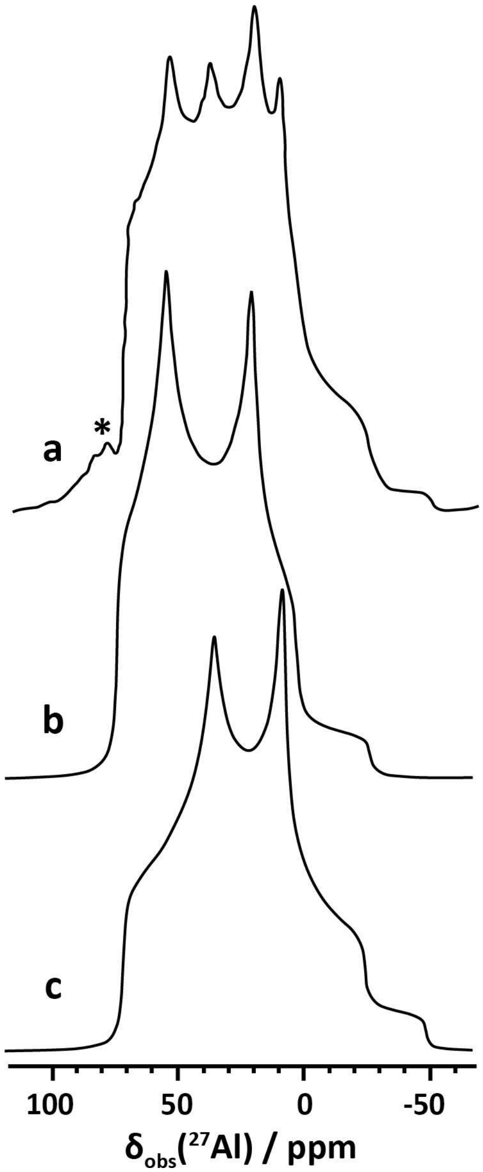

Fig. 5. ^{27}Al MAS NMR spectra (9.4 T, $\nu_R = 18.0$ kHz) of cubic C_3A ($3CaO \cdot Al_2O_3$): (a) showing the resonance from the central transition. Simulations for each of the two AlO_4 sites are shown in (b) and (c). *Resonances from satellite transitions. Adapted from Skibsted et al., 1991 [49].

4.1.2. Innovation in cements to reduce CO_2 emissions

Commercially produced cements contain a worldwide average of ~20%, but up to 95% in some cases, replacement of PC clinker by

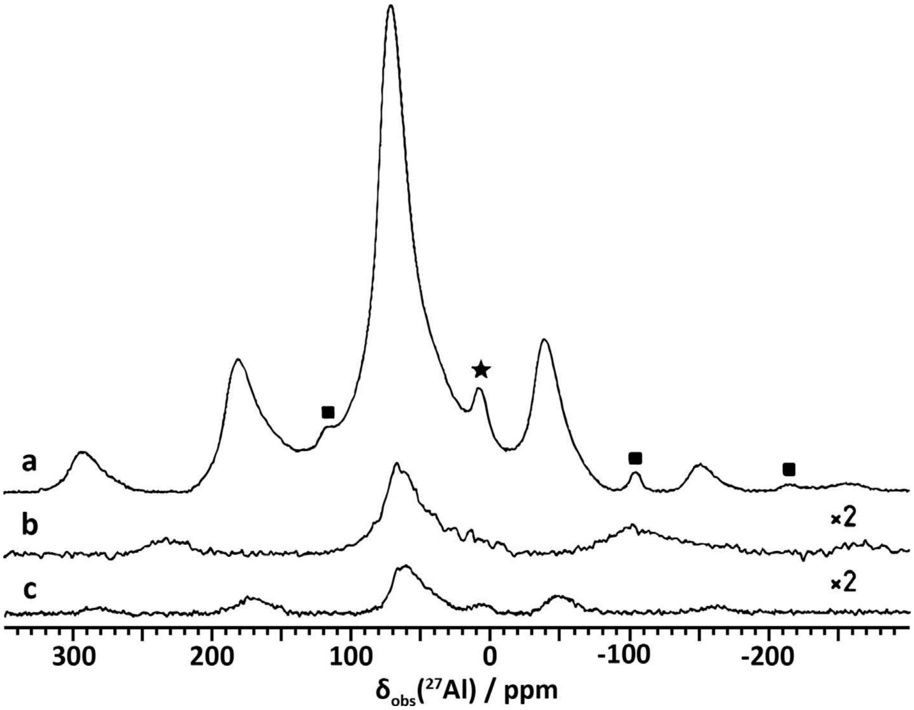

Fig. 6. ^{27}Al MAS NMR spectra (9.4 T) for the synthetic ferrites (a) $Ca_2Al_{1.33}Fe_{0.67}O_5$, (b) Ca_2AlFeO_5 and (c) $Ca_2Al_{0.93}Fe_{1.07}O_5$, acquired using between 18,000 and 76,000 scans and spinning speeds of 11.6, 17.5 and 11.5 kHz, respectively. The spectra in (b) and (c) are shown on identical intensity scales, which correspond to a vertical expansion by a factor of two relative to the spectrum in (a). The asterisk and squares in (a) indicate the resonance from the central transition and spinning sidebands for the Al^{VI} site. Adapted from Skibsted et al. [55].

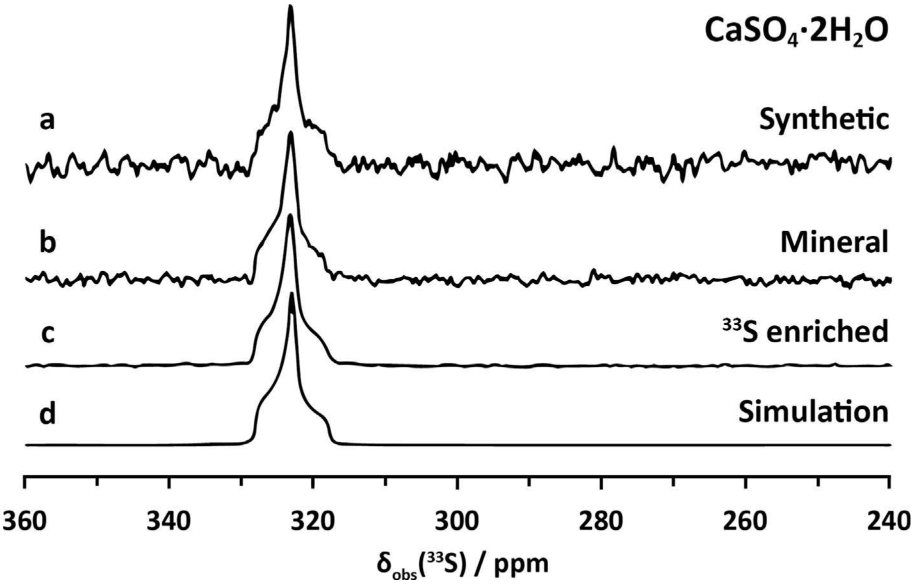

Fig. 7. ^{33}S MAS NMR spectra (19.6 T, $\nu_R = 6-8$ kHz) of (a) synthetic, (b) mineral and (c) ^{33}S-enriched gypsum ($CaSO_4 \cdot 2H_2O$) and (d) a second-order quadrupolar model of the central transition adjusted to the experimental data using DMFIT [60] and the NMR parameters reported in Ref. [59]. Adapted from d'Espinose de Lacaillerie et al. [59].

SCMs, while maintaining similar performance to existing cements [61]. The SCMs used are primarily fine limestone, ground granulated blast-furnace slags (GGBFSs), coal FAs and silica fume, with recent developments also focussing on ternary blends, e.g. those containing both calcined clays and ground limestone [61]. The use of non-PC hydraulic clinkers such as CACs, CSA cements, belite-ye'elimite-ferrite clinkers and magnesia-based cements, as well as non-clinker–based cements such as AAMs, can also offer significant reductions in CO_2 emissions.

The materials used as SCMs are often crystallographically disordered, compositionally variable and multiphase in nature. SS NMR has consequently been instrumental in characterising the local structure of these materials, which are used both as SCMs in blends with PC and also as precursors for alternative cements. The expected δ_{obs}, δ_{iso} and C_Q for different nuclei in the main phases found in common SCMs are shown in Table 3 and discussed in the following text.

4.1.2.1. Supplementary cementitious materials

4.1.2.1.1. Limestone. Limestone used as an SCM comprises primarily the $CaCO_3$ polymorphs calcite and aragonite, as well as some dolomite ($CaMg(CO_3)_2$). Calcite and aragonite, as well as the additional $CaCO_3$ polymorph vaterite, are also generated within cements in service as the calcium-rich cement hydrate phases react with atmospheric CO_2 in a process known as carbonation [62]. ^{43}Ca MAS NMR analysis of calcite, aragonite and vaterite [40,41] has revealed substantially different chemical shifts and quadrupolar coupling constants for each polymorph, δ_{iso} = 21.6, 12.6 and −26 ppm and C_Q = 1.39, 3.7 and 0.68 MHz for calcite, vaterite and aragonite, respectively. ^{13}C MAS NMR spectra of crystallographically pure calcite and aragonite show single resonances in each phase at approximately δ_{iso} = 168 ppm and 170 ppm, respectively [63,64], while crystallographically pure vaterite exhibits two ^{13}C MAS NMR resonances at δ_{iso} = 170 ppm and 169 ppm [65].

4.1.2.1.2. Blast furnace slag. GBFS GGBFS is generated as a secondary product of pig iron production in a blast furnace; the liquid silicate slag is tapped from the furnace, rapidly cooled by granulation and then ground to a particle size similar to that of PC. It can be blended with PC at replacement ratios as high as 95% under current European standards (EN 197-1) [66] and is also a primary precursor for low-CO_2 cements [4].

GGBFS consists primarily of depolymerised calcium silicate glasses, as well as small amounts of low-crystallinity phases within the melilite group [18,67–70]. The composition of GGBFS is dependent on the characteristics of the iron produced and ore used, as well as the operational details of the blast furnace [69], with CaO, Al_2O_3, SiO_2 and MgO contents typically varying between 35–42 wt %, 7–13 wt %, 34–36 wt % and 6–15 wt % respectively [67–69,71–73]. The Al in the depolymerised silicate glass is charge balanced mainly by Ca^{2+} cations, with excess calcium cations contributing to the depolymerisation of the aluminosilicate framework [67–69]. As in most glasses, the reactivity of GGBFS is dependent on the level of depolymerisation of the aluminosilicate framework [67,68]. ^{29}Si and ^{27}Al MAS NMR studies of GGBFS were interpreted as indicating that silicon is present mainly as a dimeric tetrahedral species, and Al is present in tetrahedral coordination [74]. Shimoda et al. [75–78] examined local structures in an amorphous synthetic slag using isotopic enrichment and multinuclear MAS and MQMAS NMR, probing ^{27}Al, ^{29}Si, ^{25}Mg, ^{17}O and ^{43}Ca nuclei (Fig. 8), and showed that the amorphous slag framework structure can be generally described as a depolymerised chain-like network of SiO_4 tetrahedra branched with AlO_4 tetrahedra, with oxygen atoms occupying structurally inequivalent sites (dependent on their bonding nature), and multisite occupancy of Mg and Ca ions. These observations are supported by molecular dynamics simulations [79]. The structure and chemical characteristics of GGBFS are analogous to those of numerous other calcium aluminosilicate glasses which have been examined in detail using MAS NMR [80–86].

4.1.2.1.3. Coal FA. Coal FA, a by-product of thermoelectric coal combustion, comprises primarily Al_2O_3 and SiO_2 within an assemblage of aluminosilicate glassy phases, with some additional minor crystalline constituents, which can include quartz, mullite, ferrite spinels, calcium aluminates and others [87–89]. The characteristics of coal FAs (composition, extent of heterogeneity in the glass and the local structure of each phase within the ash) vary widely between sources and as a function of time and are dependent on the type of coal used and the combustion process through which it passes [90–92]. Mineral constituents in coal (mostly silicates and aluminosilicates) are melted as the coal is burned, become entrained in the flue gas as small droplets and are then cooled and collected as a fine powder, by electrostatic precipitators in the chimney stacks of the power station. FA is blended with PC at replacement fractions up to ~50% in many parts of the world as its reactive silicate fraction can react with calcium hydroxide through

Table 3
Coordination type and expected δ_{obs}, δ_{iso} and C_Q ranges for different nuclei in various supplementary cementitious materials.

Phase	Nucleus	Site	Coordination	δ_{obs} (ppm)	δ_{iso} (ppm)	C_Q (MHz)	Magnetic field (T)	Reference
Limestone	^{13}C	$CaCO_3$ (calcite)	4	168	168	–	8.45, 9.4	[63,64]
		$CaCO_3$ (aragonite)	4	170	170	–	8.45, 9.4	[63,64]
		$CaCO_3$ (vaterite) site 1	4	169	169	–	8.45, 9.4	[65]
		$CaCO_3$ (vaterite) site 2	4	170	170	–	8.45, 9.4	[65]
	^{43}Ca	$CaCO_3$ (calcite)	6	–	21.6	1.39	8.45, 11.75, 21.1	[40,41]
		$CaCO_3$ (aragonite)	9	–	12.6	3.7	8.45, 14.1, 18.8	[40,41]
		$CaCO_3$ (vaterite)	–	–	−26	0.68	8.45, 11.75, 21.1	[40,41]
Blast furnace slag	^{17}O	Mg-NBO	2	–	55	2.2	16.4	[75]
		(Mg,Ca)-NBO	2	–	66	2.4	16.4	[75]
		Si-$\underline{\text{O}}$-Al	2	–	68	3.3	16.4	[75]
		(Ca,Mg)-NBO	2	–	81	2.8	16.4	[75]
		(Ca,Mg)-NBO	2	–	92	2.7	16.4	[75]
		Ca-NBO	2	–	120	2.9	16.4	[75]
	^{25}Mg	$(MgO_6)_1$	6	–	17	2.7	16.4	[75]
		$(MgO_6)_2$	6	–	10	4.6	16.4	[75]
	^{27}Al[a]	Al^{IV}	6	55–68	76	4.3	9.4, 14.1, 16.4	[18,20,73,75,199,438]
	^{29}Si[a]	Q^1	1	−73–−91	−73–−91	–	7.05, 9.4, 14.1, 16.4	[18,20,71–73,75,199,206,438]
	^{43}Ca	Ca	–	25	–	–	16.4	[75]
Coal fly ash	^{27}Al	Al^{IV}	4	40–60	–	–	14.1	[20,88,103–105]
		Al^{VI}	6	−10 to 10	–	–	14.1	[20,88,103–105]
	^{29}Si	$Q^4(m\text{Al})$, $m = 0$ - 4	4	−90 to −120	–	–	14.1	[20,88,103–105]
Metakaolin	^{27}Al	Al^{IV}	4	56–60	–	–	7.05, 11.7	[107,110–113]
		Al^{V}	5	30–40	–	–	7.05, 11.7	[107,110–113]
		Al^{VI}	6	0–10	–	–	7.05, 11.7	[107,110–113]
	^{29}Si	Q^4(1Al)	4	−103	−103	–	11.7	[110]
Silica fume	^{29}Si	Q^4	4	−110	−110	–	7.1, 9.4	[8,119,120]

[a] The distribution of ^{27}Al and ^{29}Si MAS NMR resonances for slag typically spans between 60 and 80 ppm; for clarity, only the resonance in this distribution exhibiting the maximum intensity is provided.

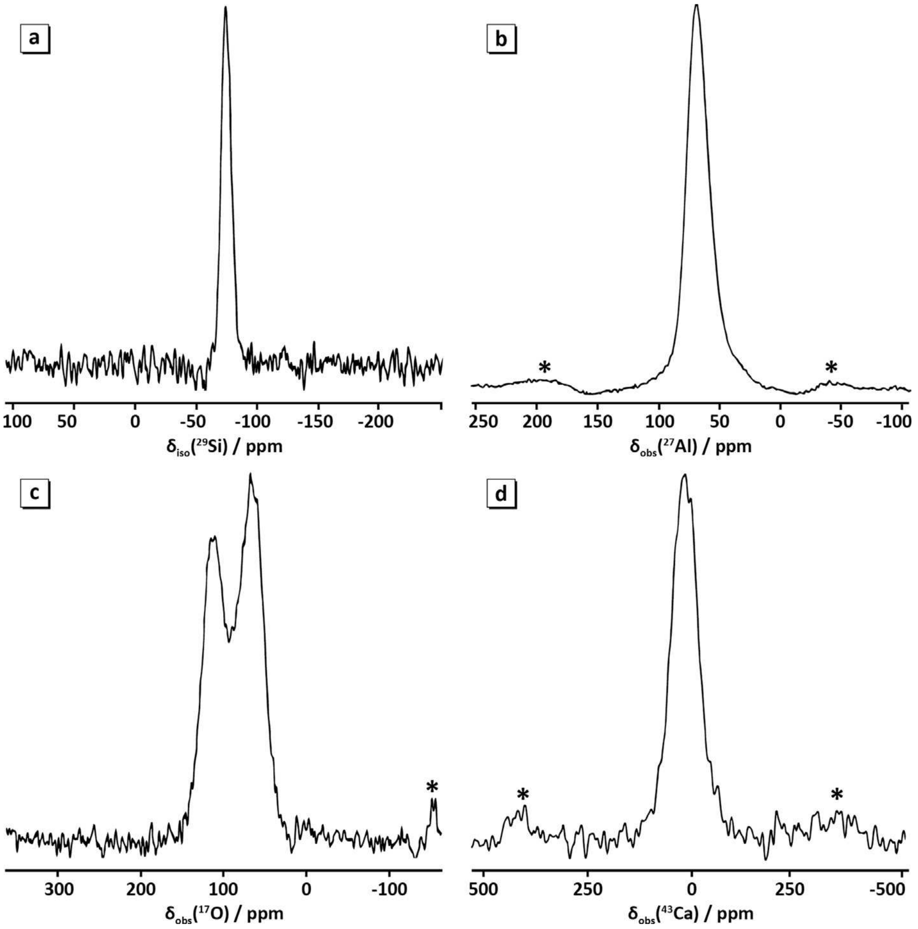

Fig. 8. (a) ^{29}Si, (b) ^{27}Al, (c) ^{17}O and (d) ^{43}Ca MAS NMR spectra (16.4 T, $\nu_R = 18$ kHz) of synthetic slag enriched in ^{17}O and ^{43}Ca. Adapted from Shimoda et al., 2008 [75]. *Spinning sidebands.

the 'pozzolanic' reaction ($Ca(OH)_2$ + reactive silicates → calcium silicate hydrate) to produce desirable binding phases, while reducing the overall environmental impact of the cement and also valorising this ash which would otherwise be a problematic high-volume waste requiring landfilling.

Phase segregation upon cooling occurs over the majority of the relevant compositional range for aluminosilicate glasses, and so as the molten aluminosilicate materials are quenched rapidly as the flue gas cools, the various phases formed are finely interspersed within the FA particles. The result is a highly heterogeneous material, as different FA particles cool at different rates and are derived from different mineral matter entrained in the coal [93], resulting in both inter- and intra-particle variation in local phase composition [94]. As a result, FA reactivity when used as an SCM (i.e. blended with PC) or as a precursor for AAM varies significantly between ashes, and between phases within each particular ash [95–102].

The crystalline phases present in FA occur in small amounts; in the low-calcium ashes which are considered most desirable for blending with PC, these phases (predominantly quartz, mullite and ferrite spinels) are relatively unreactive when compared to the aluminosilicate glassy phase. Consequently, knowledge of the composition of the glassy phase is important for correct formulation when designing cements containing FA, and SS MAS NMR (used in conjunction with electron microscopy) is a key technique that can provide this information, as long as the ash is not too rich in iron.

^{29}Si and ^{27}Al MAS NMR studies of FA have shown that the vitreous aluminosilicate phase contains a distribution of $Q^4(m\text{Al})$ Si species, with aluminium mainly present in poorly ordered tetrahedral coordination, and also revealed the presence of a small amount of Al in octahedral coordination in mullite-like crystallites and glasses (Fig. 9) [20,88,103–105]. The quantity of each $Q^4(m\text{Al})$ Si species, as well as the distribution of Al^{IV} and Al^{VI} sites, is dependent on the local phase chemical composition. ^{17}O MAS NMR studies have shown that alkali and alkali earth metals (mainly Na and K in FA) can act as network modifiers and form non-bridging oxygen sites if present in high enough concentrations in aluminosilicate glasses [106] which are analogous to the glassy phase in FA.

4.1.2.1.4. Metakaolin. Metakaolin is a layered aluminosilicate material which is used in cements as a pozzolanic additive and is produced by dehydroxylation of kaolinite clay at temperatures of 500––800 °C [107,108]. It is frequently used as an SCM in blends with PC [61,109]. ^{29}Si and ^{27}Al MAS NMR studies of metakaolin have shown that it consists of alternating buckled silicate and aluminate layers [68], with silicon in tetrahedral coordination (Fig. 10a) [110] and aluminium in a distribution of tetrahedral, pentahedral and octahedral coordination (Fig. 10b and c) [107,110–113], with each site exhibiting a significant degree of asymmetry in the local electric field gradient [113]. It has been suggested that metakaolin contains approximately equal amounts of tetrahedral (Al^{IV}), octahedral (Al^{VI}) and pentahedral Al (Al^{V}) [111,114,115]; however others have found through crystallographic analysis that some of the Al is tricoordinated [116].

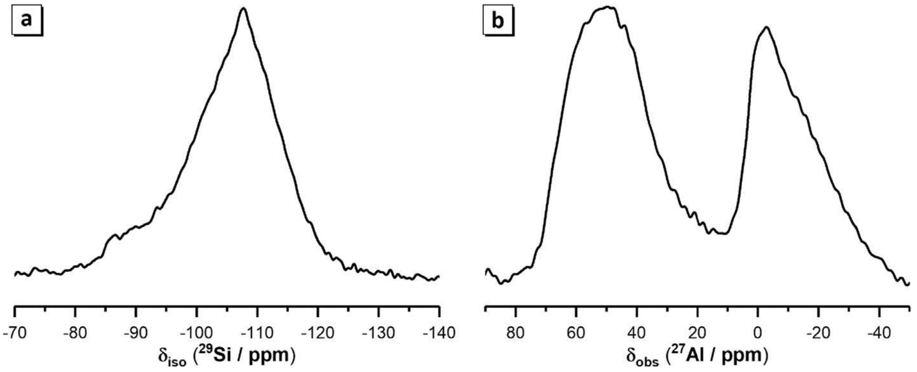

Fig. 9. (a) ^{29}Si and (b) ^{27}Al MAS NMR spectra (14.1 T, $\nu_R = 10$ kHz) of fly ash. Adapted from Bernal et al. [20]. Note that the spectra are significantly broadened by the presence of iron (5.2 wt% represented as Fe_2O_3 by X-ray fluorescence analysis) in the ash.

4.1.2.1.5. Silica fume. Silica fume is an amorphous form of SiO_2 with extremely small (tens of nm) particle size, produced as a byproduct of semiconductor Si manufacture [118]. It is commonly blended with PC at relatively low levels (up to 10 wt%) to promote strength development and durability. Published work examining silica fume via NMR is focussed on ^{29}Si MAS NMR of PC-silica fume blends, which has shown that silica fume comprises a distribution of Si atoms in tetrahedral coordination (Q^4 units), connected by oxygen bridges [8,119,120]. Because silica fume is a pure silica source with a ^{29}Si resonance that is clearly distinct from that of either PC or any of its hydration products, it is possible to accurately determine the extent of reaction of silica fume within a blended cement through ^{29}Si MAS NMR; this is much more accurate for silica fume than for any other siliceous SCMs, as the other SCMs have resonances which at least partially overlap the signal due to the PC or its reaction products [121].

4.1.2.2. Non-PC hydraulic clinkers

4.1.2.2.1. Calcium aluminate cement. CACs consist primarily of monocalcium aluminate ($CaAl_2O_4$, CA), which typically accounts for 40–60% wt. % of commercial CACs, along with smaller quantities of $C_{12}A_7$ and CA_2 [23,122]. While considerably more expensive than PC, these cements are intended for use in applications where rapid hardening is useful and/or when resistance to thermal stresses, chemical (particularly acid) attack and impact or abrasion is desired [122], e.g. refractory concretes, cements and concretes for effluent treatment infrastructure, blended cements for marine applications and other demanding service environments. CACs are now restricted from bulk use in structural concrete due to a series of material failures in past decades [123], but this does not limit their use in specialist applications. The expected δ_{obs}, δ_{iso} and C_Q for different nuclei in CAC are shown in Table 4 and discussed in the following text.

4.1.2.2.1.1. Monocalcium aluminate, $CaAl_2O_4$

Monocalcium aluminate, CA, is the principal reactive phase which controls the performance of CAC. The crystal structure of CA consists of AlO_4 tetrahedra forming six-membered rings in a tridymite-like structure [124]. ^{27}Al MAS NMR isotropic chemical shifts and quadrupolar coupling parameters for each of the six non-equivalent AlO_4 tetrahedra in CA have been determined by ^{27}Al MAS NMR at multiple fields (7.1, 9.4 and 11.7 T in Refs. [50,52] and 18.8 T in Ref. [84]), giving 81.9 ppm $\leq \delta_{iso} \leq$ 83.8 ppm and

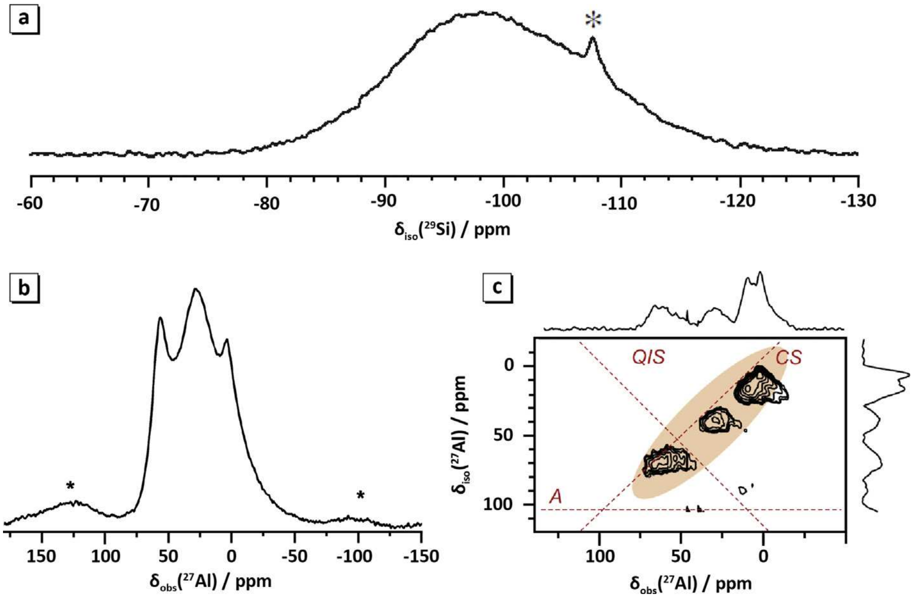

Fig. 10. (a) ^{29}Si MAS NMR (9.4 T, $\nu_R = 6$ kHz, adapted from Dai et al. [117]), where * indicates a resonance from a quartz impurity), (b) ^{27}Al MAS NMR (11.7 T, $\nu_R = 15$ kHz, adapted from Duxson et al. [111]) and (c) ^{27}Al triple quantum (3Q) MAS NMR (11.7 T, adapted from Kobera et al. [113]) spectra of metakaolin.

Table 4
Coordination, expected δ_{obs}, δ_{iso} and C_Q for different nuclei in calcium aluminate cements.

Phase	Nucleus	Site	Coordination	δ_{obs} (ppm)	δ_{iso} (ppm)	C_Q (MHz)	Magnetic field (T)	Reference
Monocalcium aluminate (CA)	^{27}Al	$Al^{IV}{}_1$	4	–	81.9	2.50	7.1, 9.4 and 11.7	[52]
		$Al^{IV}{}_2$	4	–	83.8	2.60	7.1, 9.4 and 11.7	[52]
		$Al^{IV}{}_3$	4	–	86.2	2.60	7.1, 9.4 and 11.7	[52]
		$Al^{IV}{}_4$	4	–	82.7	3.32	7.1, 9.4 and 11.7	[52]
		$Al^{IV}{}_5$	4	–	81.6	3.37	7.1, 9.4 and 11.7	[52]
		$Al^{IV}{}_6$	4	–	81.2	4.30	7.1, 9.4 and 11.7	[52]
Calcium dialuminate (CA_2)	^{27}Al	$Al^{IV}{}_1$	4	–	75.5	6.25	7.1, 9.4 and 11.7	[52]
		$Al^{IV}{}_2$	4	–	69.5	9.55	7.1, 9.4 and 11.7	[52]
Mayenite ($C_{12}A_7$)	^{27}Al	$Al^{IV}{}_1$	4	–	85.9	9.7	7.1, 9.4 and 11.7	[52]
		$Al^{IV}{}_2$	4	–	80.2	3.8	7.1, 9.4 and 11.7	[52]

2.5 MHz $\leq C_Q \leq$ 4.3 MHz by deconvolution of both the resonance from the central transition and the spinning sidebands. Variations in the geometry of the AlO_4 tetrahedra (primarily differences in Al-O bond lengths [124]) are primarily reflected in the ^{27}Al MAS NMR quadrupolar parameters rather than in chemical shifts. This work contrasted earlier assertions that the resonance from the central transition could be simulated with a single set of quadrupolar parameters and two isotropic chemical shifts [51].

High-field (18.8 T) ^{17}O MAS NMR of CA has resolved eight resonances due to O atoms in Al^{IV}-$\underline{O}$-Al^{IV} linkages [84] with chemical shifts between 50 and 90 ppm and C_Q values less than 2 MHz, with the tricluster oxygen site exhibiting the largest C_Q (Fig. 11). This work demonstrated the benefits of utilising high fields which can narrow resonances sufficiently to resolve additional sites; eight of the twelve crystallographically distinct ^{17}O sites in CA were able to be resolved at 18.8 T [84], while only five of these ^{17}O sites could be resolved at 14.1 T [125].

4.1.2.2.1.2. Calcium dialuminate, $CaAl_4O_9$

Calcium dialuminate (CA_2) is found in relatively alumina-rich CAC clinkers that are used as refractory cements and is a slowly reacting cement constituent. Its structure comprises two tetrahedrally coordinated Al atoms; one AlO_4 tetrahedron contains two tricoordinated oxygen atoms and the other contains a single tricoordinated oxygen atom, with the remaining oxygens each connected to two Al atoms (Fig. 12) [126,127]. ^{27}Al MAS NMR data collected at multiple fields (7.1 T, $\nu_R = 18.0$ kHz; 9.4 T, $\nu_R = 18.0$ kHz and 11.7 T, $\nu_R = 15.2$ kHz) resolved single resonances for each tetrahedrally coordinated Al atom, with $\delta_{iso} = 75.5$ ppm and 69.5 ppm [52], and significant C_Q values (6.25 MHz and 9.55 MHz, respectively) due to electric field gradient (EFG) asymmetry caused by the nearby tricoordinated oxygens. Earlier work by Müller et al. [51] determined similar δ_{iso} and C_Q values for the site neighbouring two tricoordinated oxygens compared to those obtained by Skibsted et al. [52], but those for the AlO_4 tetrahedra containing a single tricoordinated oxygen atom exhibited larger discrepancies, likely because of the insufficient resolution and notable distortion of the central transition caused by the much lower spinning speed utilised in those early experiments.

^{17}O MAS NMR (18.8 T) resolved four distinct oxygen sites in CA, resonating between 40 and 72 ppm [84], including a tricluster oxygen atom with three Al^{IV} neighbours (i.e. an $O(Al^{IV}{}_3)$ site) resonating at approximately 40.6 ppm and with quadrupolar parameters $C_Q = 2.5$ and $\eta = 0.4$.

4.1.2.2.1.3. Dodecacalcium hepta-aluminate (mayenite), $C_{12}A_7$

Mayenite, ($Ca_{12}Al_{14}O_{33}$, $C_{12}A_7$), is generally present as a minor phase in more calcium-rich CAC clinkers. It has also been discussed in the past as a potential constituent of PC clinkers but is now considered unlikely to form under realistic commercial PC production conditions [23]. ^{27}Al MAS NMR at high spinning speed (17.8 kHz) resolved two distinct Al^{IV} sites within $C_{12}A_7$, with $\delta_{iso} = 85.9$ and 80.2 ppm, respectively, in close agreement with the known crystal structure [129] and other ^{27}Al MAS NMR investigations of this phase [50,51]. Differences between the δ_{iso} and quadrupolar parameters (3.8 MHz and 9.7 MHz) of these two Al^{IV} sites arise due to distortions in one of the tetrahedra [50], which result in oxygen mobility [130]. Consequently (although maybe

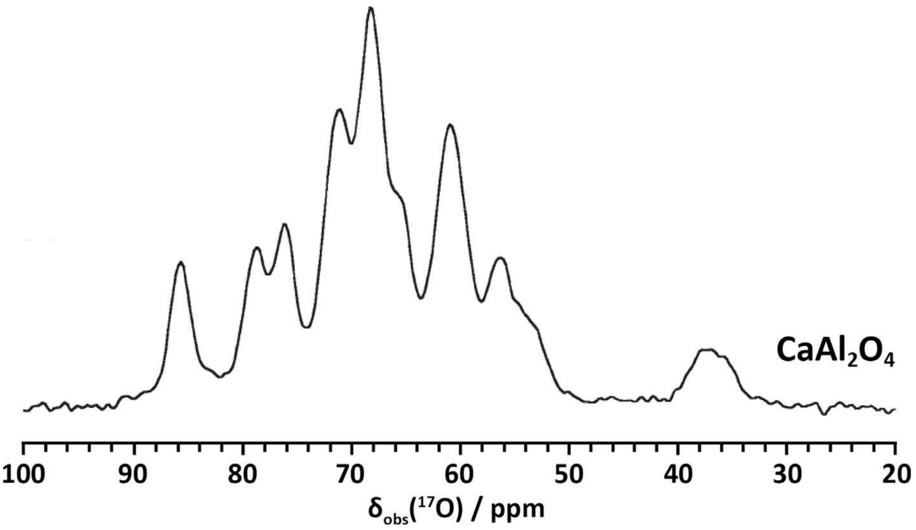

Fig. 11. ^{17}O MAS spectrum of $CaAl_2O_4$ at 18.8 T. Adapted from Stebbins et al. [84].

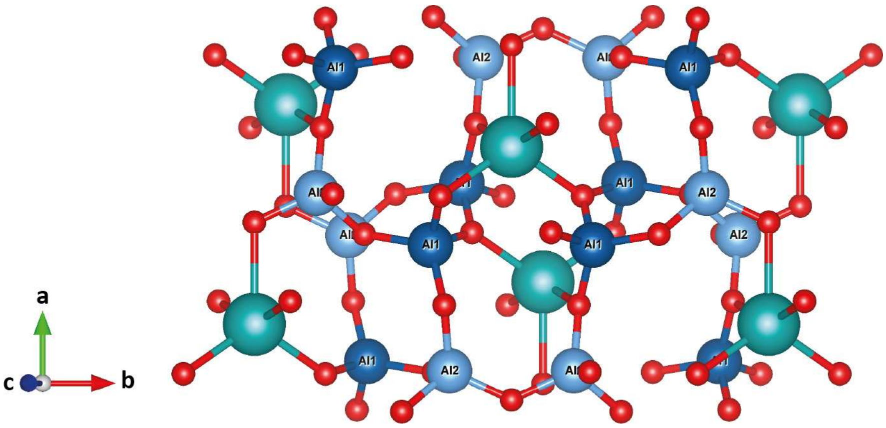

Fig. 12. Illustration of the local environments in the crystal structure of CA_2, based on information obtained from single-crystal diffraction data [127]. The two AlO_4 tetrahedra are denoted by Al1 (containing two tricoordinated oxygen atoms) and Al2 (containing a single tricoordinated oxygen atoms). Ca atoms are represented by cyan spheres, Al atoms are represented by dark and light blue spheres (denoting Al1 and Al2, respectively) and O atoms are represented by red spheres. Prepared using the VESTA software package [128].

incidentally in the context of cement chemistry), mayenite has also received significant attention as a high-performance oxygen ion conductor [131].

4.1.2.2.2. CSA cements. CSA cements comprise calcium sulfoaluminate (ye'elimite, $Ca_4(AlO_2)_6SO_4$, $C_4A_3\$$) and other clinker phases such as belite, C_4AF, ternesite ($C_5S_2\$$) and/or calcium aluminates and are typically blended with calcium sulphate to regulate the rate of their setting [61,132]. ^{27}Al MAS NMR investigations of commercially produced CSA and synthetic ye'elimite showed nearly identical spectra, consisting of a single peak (with maximum intensity at approximately 68 ppm) with two high-field shoulders at approximately 60 and 52 ppm [34,133–135]. Evidence enabling discrimination of two of the eight non-equivalent Al sites present in the crystal structure of ye'elimite (which is an aluminate analogue of the sodalite framework) [136] was identified in this broad peak [133]. Recent work by Skibsted et al. [137] reported that the ^{27}Al MAS NMR spectral region for Al^{IV} in ye'elimite (~80–50 ppm) is dominated by overlapping resonances from the eight different Al sites. Isotropic projections from ^{27}Al MQMAS NMR spectra obtained by the same authors revealed four distinct resonances with very similar isotropic chemical shifts and quadrupole coupling parameters [34,138].

Ternesite, sometimes also called sulfospurrite, is a common minor constituent in modern CSA cements that is now being understood to have some hydraulic activity but also forms within PC kilns as an undesirable deposit on the refractory that reduces kiln performance. Ternesite exhibits a single, well-defined ^{29}Si MAS NMR resonance at -73.0 ppm [139], consistent with its crystal structure [140] in which double layers of silicate tetrahedra alternate with single layers of sulphate tetrahedra, with calcium 7-coordinated to oxygen atoms.

The application of NMR spectroscopy to the belite and tetracalcium aluminate phases present in CSA cements has been discussed in detail in sections 4.1.1.2 and 4.1.1.4, respectively.

4.1.2.2.3. Magnesia-based cements. Magnesium silicate hydrate (M-S-H) cements are typically formed from a source of magnesium and a source of highly reactive silica, such as silica fume [141]. The magnesium source is typically light-burned MgO, and $Mg(OH)_2$ can also be used [142]. Although M-S-H was initially identified as a degradation product in PC exposed to chemically aggressive conditions [141,143], subsequent work has shown that M-S-H gels can also form a cementitious mass to generate high compressive strength [144–148]. These gels will be discussed in detail in section 4.2.6.

The ^{25}Mg MAS NMR spectrum of polycrystalline MgO exhibits a single sharp resonance at $\delta_{iso} = 26$ ppm [149,150], while the ^{17}O MAS NMR spectrum of this compound enriched with ^{17}O contains a single sharp resonance at 47 ppm [150,151], consistent with octahedral MgO_6 sites in the cubic crystal structure of this phase, and in good agreement with first-principles calculations using DFT [152]. The ^{25}Mg MAS NMR spectrum of $Mg(OH)_2$ (brucite) exhibits a typical quadrupolar resonance with $\delta_{iso} = 14.1$ ppm and $C_Q = 3.15$ MHz [153]. Application of NMR spectroscopy to silica fume has been discussed in detail in section 4.1.2.1.5. Many other magnesia-based cements also exist, including those based on magnesium carbonates, phosphates and oxysalts (both chloride and sulphate) [141]; MgO is the primary Mg source used in the production of most of these cements.

4.2. MAS NMR of key cementitious binding phases

The vast majority of SS MAS NMR investigations of cementitious binding phases, which are often complex, disordered silicates [17,18,20,21,104,154,155], have probed ^{29}Si and ^{27}Al nuclei, yielding information about the coordination states of Al and the connectivity of Si (via oxygen bridges to Si or Al or to non-bridging oxygen sites). The low natural abundance of ^{29}Si (4.7%) results the need for long data acquisition times for non-enriched samples, but the wealth of information obtainable from this technique has meant that it is nonetheless widely used [22].

4.2.1. Calcium silicate hydrate gels

Calcium silicate hydrate (C-S-H) is the main product of PC hydration. It displays low crystallinity and variable composition and comprises (in general terms) Q^2 Si chains of varying lengths with Q^1 Si sites at chain termination points, as shown by ^{29}Si MAS NMR [17,54,156,157]. These silicate chains are flanked by an interlayer containing confined H_2O molecules, aqueous cationic species (Ca^{2+} and H^+ in pure C-S-H, but with scope for substitution, particularly by alkali metals) and a calcium oxide sheet (Fig. 13) [158,159]. The silicate chains are arranged in a 'dreierketten' structure, based on a repeating chain unit of three tetrahedral sites, two 'pairing' and one 'bridging', where vacancies in the bridging sites lead to characteristic chain lengths of $(3n-1)$ for integer values of n [160]. The two pairing Si^{IV} units ($Q^2(p)$) are linked with the calcium oxide sheet [159]. The expected δ_{obs}, δ_{iso} and C_Q for different nuclei in C-S-H, aluminium-substituted C-S-H (C-(A)-S-H) and alkali- and

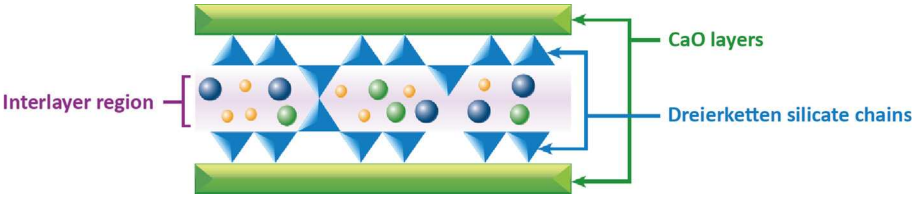

Fig. 13. Schematic representation of the structural features of calcium-silicate hydrate (C-S-H) gels, adapted from Provis and Bernal [4]. Tetrahedral Si sites and CaO layers are shown by blue triangles and green rectangles, respectively. Circles denote various interlayer species (water or cations).

aluminium-substituted C-S-H (C-(N,K)-A-S-H) are shown in Table 5 and discussed in the following text.

Numerous structural models for C-S-H have been proposed, including those based on jennite [161,162] and tobermorite [159,163], with recent SS NMR work probing both ^{29}Si [164–167] and ^{17}O [168] nuclei indicating strong structural similarity of C-S-H with a distorted tobermorite-like structure. ^{29}Si MAS NMR spectroscopy in combination with other techniques has shown that C-S-H forms a structural series which shows both continuity and diversity, with phase-pure C-S-H exhibiting Ca/Si ratios at least between 0.55 and 2.0 [167,169,170]. Recent work combining dynamic nuclear polarisation–enhanced (^{29}Si)^{29}Si double quantum coherence (the Incredible Natural Abundance Double Quantum Transfer Experiment, INADEQUATE) and (^{1}H)^{29}Si HETCOR MAS NMR analysis approaches, with atomistic modelling, determined a series of atomic level structures for C-S-H based on defective tobermorite with Ca/Si ratios of 1.25–2.0 [170]. These models include a structurally important interlayer calcium site which bridges Q^1 silicate species and is associated with strong hydrogen bonding that stabilises the C-S-H, allowing high Ca/Si ratios to be reached in a phase-pure C-S-H.

Despite experimental and analytical difficulties arising from the low natural abundance and large quadrupole moment of ^{17}O, MAS NMR spectroscopy probing this nucleus has revealed valuable information regarding the role of oxygen species in C-S-H gels. Cong et al. [43,168] used ^{17}O MAS NMR to study C-S-H in both synthetic gels and hydrated β-C_2S, identifying two non-bridging oxygen sites (linking a Si atom with two or three Ca^{2+} ions, Si-$\underline{\text{O}}$-Ca^{2+}), a single bridging oxygen site (linking two Si atoms, Si-$\underline{\text{O}}$-Si), oxygen atoms within surface hydroxyl groups linked with either Ca^{2+} (Ca-OH) or framework Si atoms (Si-OH) and a single site corresponding to oxygen within interlayer H_2O molecules. The observations of these ^{17}O MAS NMR resonances (and their relative intensities) support the Richardson and Groves [159] defect-tobermorite model for C-S-H. Both non-bridging and bridging oxygen sites were observed to become less shielded with increasing Ca/Si ratio and decreasing polymerisation, indicating a decrease in the average Si-$\underline{\text{O}}$-Si bond angles, consistent with previous observations of a decrease in the *b* axis of the pseudo-unit cell of C-S-H [167] at a higher Ca/Si ratio.

As mentioned previously, natural abundance ^{43}Ca MAS NMR experiments face inherent difficulties due to the low natural abundance (0.145%), high quadrupole moment and small magnetogyric ratio of this nucleus, Table 1. Consequently, very few studies probing ^{43}Ca in C-S-H via MAS NMR have been performed. Moudrakovski et al. [38] used ^{43}Ca MAS NMR to study a series of C-S-H gels of differing Ca/Si ratios, as well as C-S-H produced by hydrating triclinic C_3S, crystalline 11 Å tobermorite and portlandite (Fig. 14). The coordination state of Ca^{2+} in C-S-H is complex and not yet fully resolved, but the work of Richardson [171] indicates the expectation that the most probable coordination numbers in plausible C-S-H structures are 6 or 7 depending on the site type and occupancy.

Paired SiO_4 chain sites (Q^2(p)) and bridging SiO_4 chain sites (Q^2(b)) in C-S-H in hydrated PC exhibit overlapping ^{29}Si MAS NMR resonances [16,172] and therefore cannot be resolved individually

Table 5
Coordination states and expected δ_{obs}, δ_{iso} and C_Q values for different nuclei in C-S-H, C-(A)-S-H and C-(N,K)-(A)-S-H.

Nucleus	Site	Coordination	δ_{obs} (ppm)	δ_{iso} (ppm)	C_Q (MHz)	Magnetic field (T)	Reference
^{1}H	Ca-OH	1	1.0	–	–	7.04, 9.4, 11.7	[164,180–182,310]
	Si-OH	1	4.5	–	–	7.04, 9.4, 11.7	[164,180–182,310]
	H_2O	1	5.2			7.04, 9.4, 11.7	[164,180–182,310]
^{17}O	Si-$\underline{\text{O}}$-Ca	2	–	104–112	2.4	11.74	[43,168]
	Si-$\underline{\text{O}}$-Si	2	–	60–82	4.5	11.74	[43,168,366]
	Si-$\underline{\text{O}}$-Al	2		45.5	0.5	14.1	[366]
	Ca-OH	2	–	70	6.5–7.2	11.74	[43,168]
	Si-OH	2	–	4–10	4.4–5.6	11.74	[168]
	Interlayer H_2O	2	–	0	0	11.74	[43,168]
^{23}Na	Interlayer Na^+	–	−3	−3.7	1.0	14.10	[14,366]
^{27}Al	q^2 charge balanced by interlayer Ca^{2+}, Na^+ or H^+ cations	4	66	–	–	9.4, 17.5	[190,193]
	q^2 charge balanced by interlayer or surface Al^{V} or Al^{VI} cations	4	–	74.6	4.5	17.5	[193]
	q^3	4	65	60	4.1	9.4, 11.7, 14.1	[14,20,188,201,366]
	Interlayer Al^{IV}	5	–	39.9	9.1	7.1, 9.39 and 17.5	[192–194]
^{29}Si	Q^1	4	−80 ± 4	−80 ± 4	–	7.1, 9.4	[17,157]
	Q^{2}[a]	4	−85 ± 4	−85 ± 4	–	7.1, 9.4	[16,17,172]
	Q^2(1Al)[a]	4	−80 ± 4	−80 ± 4	–	9.4, 14.1	[20,21,199]
	Q^2(b)	4	−83.4	−83.4	–	9.4, 11.7, 17.5	[15,172,188,190,193]
	Q^2(p)	4	−85.3	−85.3	–	9.4	[15,172,188,190,193]
	Q^2(p)(1Al)		−80.5–−82.0	−80.5–−82.0	–	9.4	[15,172,188,190,193]
	Q^3	4	−95 ± 4	−95 ± 4	–	7.1, 9.4, 14.1	[20,188,199]
	Q^3(1Al)	4	−90 ± 4	−90 ± 4	–	9.4, 14.1	[20,21,199]
^{43}Ca	Ca-O sheet	6	10–45	–	–	21.14	[38]
	Interlayer Ca^{2+}	~7	35–85	–	–	21.14	[38]

[a] Q^2 resonances in these studies are not specified as bridging or pairing tetrahedra.

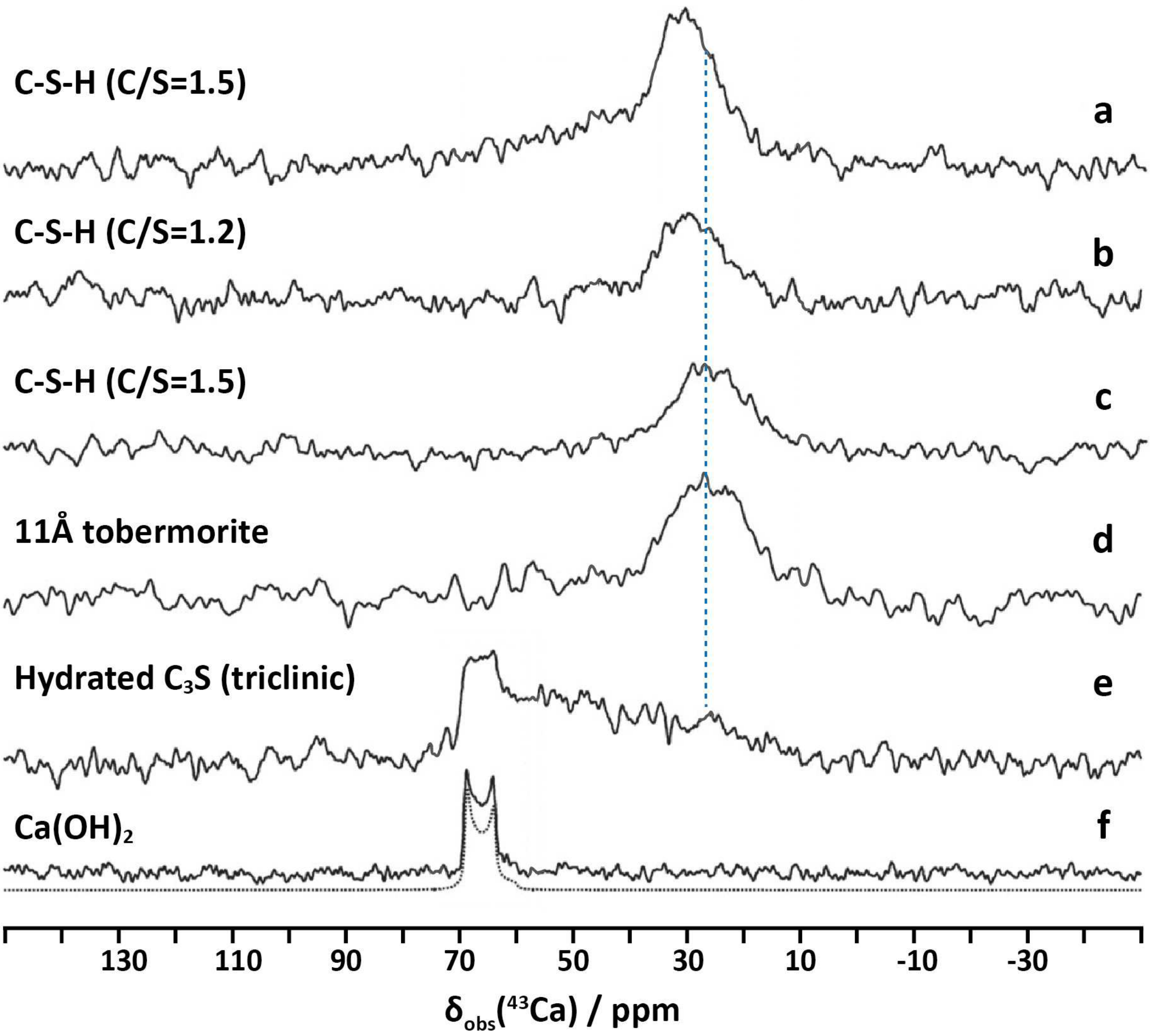

Fig. 14. Natural abundance ^{43}Ca MAS NMR spectra of (a) C-S-H (Ca/Si = 1.5), (b) C-S-H (Ca/Si = 1.2), (c) C-S-H (Ca/Si = 1.2), (d) 11 Å tobermorite, (e) hydrated triclinic C_3S and (f) portlandite ($Ca(OH)_2$). The dotted line below the spectrum of $Ca(OH)_2$ is the simulation for the second-order quadrupolar interactions, and the blue vertical line indicates the centreband position of 11 Å tobermorite. Adapted from Moudrakovski et al. [38].

using this technique; however, these sites can often be resolved by their differing ^{29}Si MAS NMR chemical shifts in synthetic C-S-H gels (Fig. 15) [173–177].

^{43}Ca MAS NMR spectra of the synthetic C-S-H gels show broad resonances at approximately 27–31 ppm, very similar to the spectrum of 11 Å tobermorite [178]. An increased Ca/Si ratio leads to decreased shielding of ^{43}Ca ions (i.e. resonances move to higher chemical shift), consistent with a decrease in the mean chain length (MCL) of the silicate, and also in good agreement with ^{29}Si MAS NMR data [167].

The ^{43}Ca MAS NMR spectrum of hydrated triclinic C_3S contains a broad resonance across a chemical shift range that includes that of the main resonances from C-S-H gels with $0.8 \leq Ca/Si \leq 1.5$, indicating that C-S-H in hydrated cement systems may contain various locally different chemical compositions [38]. Combining these observations with analysis of ^{43}Ca MAS NMR signal intensity vs. delay time, Moudrakovski et al. [38] proposed that Ca in the Ca-O sheets resonates at $10\ \text{ppm} \leq \delta_{obs} \leq 45\ \text{ppm}$ and interlayer Ca^{2+} ions resonate at $35\ \text{ppm} \leq \delta_{obs} \leq 85\ \text{ppm}$ at a field B_0 of 21.14 T.

Bowers and Kirkpatrick [179] used natural abundance ^{43}Ca MAS NMR to demonstrate that despite broad spectra, six-coordinate Ca (as present in jennite) and seven-coordinate Ca (as present in 11 Å tobermorite) may be resolved by differences in chemical shift (δ_{obs} = 24 ppm vs. −9 ppm, at 21.1 T). By using this approach, it may be possible to resolve the various locally different chemical compositions (i.e. those with differing Ca/Si ratios) within C-S-H gels.

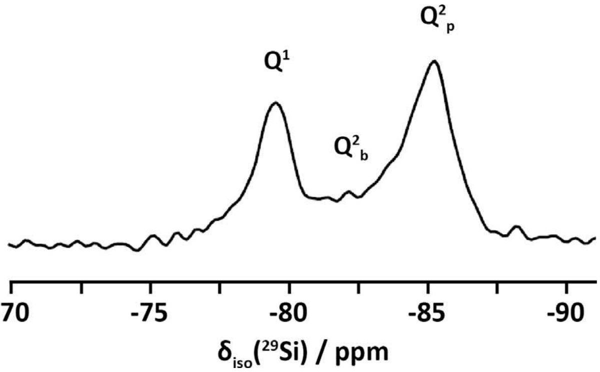

Fig. 15. ^{29}Si MAS NMR spectra of synthetic C-S-H (Ca/Si = 1) showing resonances from pairing (Q^2(p)) and bridging (Q^2(b)) silicon tetrahedra. Adapted from Lothenbach et al., 2015 [177].

Despite severe line broadening in ^{1}H MAS NMR spectra which results from ^{1}H-^{1}H dipolar couplings, the high sensitivity of ^{1}H, and the development of multipulse decoupling sequences which reduce line broadening, have led to the application of this technique to study proton environments in C-S-H [157]. However, the information obtainable from ^{1}H MAS NMR spectra of C-S-H is generally limited, due to the distribution of protons across many chemical sites and the small chemical shift range (approximately 20 ppm) over which ^{1}H in solid phases can resonate [157]. ^{1}H MAS and combined rotation and multiple pulse sequence (CRAMPS) NMR techniques have been used to monitor hydration of synthetic C_3S during the early stages of hydration and at longer intervals up to 28 days of curing [180–182]. It was demonstrated that it is possible to resolve a resonance from protons in Ca-OH at $\delta_{obs} = 5.2$ from the overlapping broad resonances of protons in Si-OH and mobile water molecules at $\delta_{obs} = 0.5–1$ ppm ($B_0 = 7.04$ and 9.44 T). Recently, quantitative ^{29}Si MAS and ^{1}H-^{29}Si CPMAS NMR experiments have been used to monitor hydration of ^{29}Si-enriched triclinic C_3S *in-situ* over the first 24 h of reaction [183]. These results were correlated with isothermal calorimetry measurements to identify the previously unobserved phenomenon of partial passivation of the surface of C_3S which drives deceleration of the reaction.

4.2.1.1. C-(A)-S-H gels. ^{29}Si MAS NMR has revealed important information regarding incorporation of Al in C–S–H (i.e. forming C-(A)-S-H) in hydrated PC [16,57,167,172,184–186], PC–SCM blends [117,187,188] and 2000-year old Roman seawater harbour concrete [189]. Application of ^{29}Si MAS NMR has allowed observation of resonances from Q^1, Q^2 and $Q^2(1Al)$ sites which make up the silicate chains in the C-(A)-S-H gel [16,167,172]. The MCL can be calculated from the intensities of $Q^n(m\mathrm{Al})$ resonances obtained from ^{29}Si MAS NMR spectral deconvolutions by using equation (1), while the degree of Al-Si substitution in the tetrahedral chains can be obtained from the intensities of the Q^1, Q^2 and $Q^2(1Al)$ resonances (equation (2)), as demonstrated by Richardson et al. [184,185] and Andersen et al. [186].

$$\mathrm{MCL}_{\mathrm{aluminosilicate}} = \frac{2\left[Q^{1} + Q^{2} + \frac{3}{2}Q^{2}(1\mathrm{Al})\right]}{\frac{1}{2}Q^{1}} \qquad (1)$$

$$\frac{Al^{IV}}{Si} = \frac{\frac{1}{2}Q^{2}(1\mathrm{Al})}{\left[Q^{1} + Q^{2} + Q^{2}(1\mathrm{Al})\right]} \qquad (2)$$

Using ^{29}Si MAS NMR, Andersen et al. [186] showed that the Al^{IV}/Si ratio in C-(A)-S-H in hydrated white PC is dependent on the availability of dissolved Al^{3+} ions, but independent of hydration time. Richardson et al. [190] used ^{29}Si MAS NMR to determine that Al preferentially substitutes into $Q^2(b)$ sites and that the MCL of aluminosilicate chains in C-(A)-S-H is dependent on both the availability of Al^{3+} ions in solution and hydration time, findings that were subsequently confirmed by Andersen et al. [184,186]. It has also been suggested that Al may substitute for Si in small amounts in pairing sites [188,191,192], although this is thermodynamically disfavoured compared to the bridging sites [191].

Al readily substitutes for Si in the bridging position in aluminosilicate chains in C-(A)-S-H up to a ratio of $Al/Si \leq 0.1$, while at higher Al/Si ratios, katoite and/or strätlingite are also formed [15]. Analysis by ^{29}Si and ^{27}Al MAS NMR has shown that the Al^{IV}/Si ratio in C-(A)-S-H in hydrated PC can be increased significantly by the presence of alkali cations (Na^+ or K^+) [16] via a mechanism in which the charge deficit introduced by Al-Si substitution is balanced by adsorption or bonding of alkali cations in the interlayer region. The role of alkalis in these structures will be discussed further in section 4.2.1.2.

^{27}Al MAS NMR experiments, particularly at high field ($B_0 \geq 14.1$ T), have proven particularly useful in gaining detailed structural information regarding the role of Al in C-(A)-S-H, in both synthetic gels and hydrated PC. ^{27}Al MAS NMR experiments at multiple fields (e.g. Fig. 16) have shown in synthetic gels and hydrated PC that the Al^{IV} bridging sites in C-(A)-S-H are charge balanced by interlayer Ca^{2+}, Na^+ or H^+ ions ($\delta_{obs} = 66$ ppm, $B_0 = 17.5$ T) [190,193] or by interlayer or surface Al^{V} or Al^{VI} ions ($\delta_{iso} = 74.6$ ppm, $C_Q = 4.5$ MHz) [193]. Al^{V} sites in the C-(A)-S-H interlayer can potentially substitute for Ca^{2+} ions ($\delta_{iso} = 39.9$ ppm, $C_Q = 5.1$ MHz) [192–194]. From these studies, and others, it was concluded that Al does not enter the Ca-O sheet, nor the pairing tetrahedral sites in the silicate chains of C-(A)-S-H [22,172,184,190,193,194].

4.2.1.2. C-(N,K)-A-S-H gels. Synthesis of C-(A)-S-H gels in an environment containing high alkali metal concentrations, such as in the production of AAMs from GGBFS [154,160], yields a C-(N,K)-A-S-H gel. This is structurally similar to C-S-H, but with Al substitution

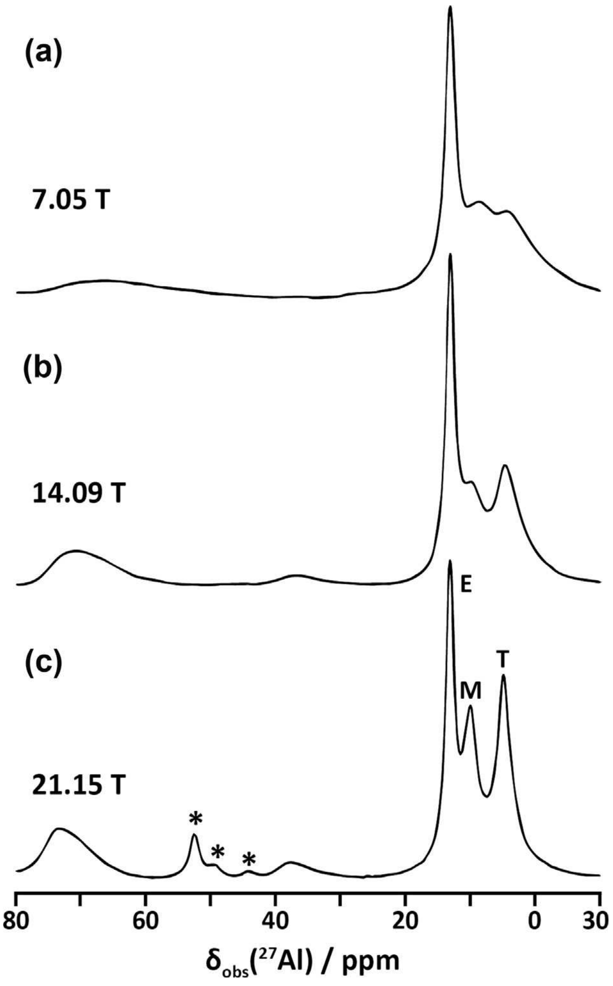

Fig. 16. ^{27}Al MAS NMR spectra of the central transition for white PC hydrated for 12 weeks recorded at (a) 7.05 T ($\nu_R = 13.0$ kHz), (b) 14.09 T ($\nu_R = 13.0$ kHz) and (c) 21.15 T ($\nu_R = 9.5$ kHz), using ^{1}H decoupling. Spinning sidebands are indicated by *. The resonances from the central transition of ettringite, monosulphate and the third aluminate hydrate phase (described in section 4.2.8) are indicated by E, M and T, respectively. Adapted from Andersen et al. [172].

in bridging tetrahedral sites and in the interlayer as discussed in the preceding section, and with charge balancing by alkali cations (Na^+ and K^+) in the gel interlayer, with additional alkalis able to sorb to the gel surfaces [74,154,185,195–197]. The structural characteristics of this complex gel have been elucidated largely by the application of SS NMR; representative spectra of alkali-activated GGBFS are shown in Fig. 17, while a schematic representation of the C-(N,K)-A-S-H gel structure is shown in Fig. 18. As with C-S-H, the C-(N,K)-A-S-H gel exhibits a disordered structure similar to that of crosslinked and/or non-crosslinked, structurally imperfect tobermorite [17,74,195]. As noted previously, there is a strong thermodynamic preference for Al substitution into bridging tetrahedra in the C-(N,K)-A-S-H gel [198].

^{29}Si MAS NMR has provided extensive evidence of the presence of cross-linked (Q^3 and/or Q^3(1Al)) sites within 2000-year-old Roman seawater harbour concrete [189], alkali-activated slag cements [20,188,199] and synthetic analogues [14,15,200–203]. The structure of these C-(N,K)-A-S-H gels was described by Myers et al. [195] as a mixture of cross-linked and non-cross—linked silicate chains within a defect-tobermorite structure, with crosslinking occurring through partially Al-substituted bridging sites [21,188,193,196]. Using this model and ^{29}Si MAS NMR spectral deconvolutions, it is possible to calculate the MCL and Al^{IV}/Si ratio of the cross-linked C-(N)-A-S-H gel structures using the following equations (3) and (4) [195].

$$\mathrm{MCL}_{\mathrm{crosslinked}} = \frac{4\left[Q^1 + Q^2 + Q^2(1\mathrm{Al}) + Q^3 + 2Q^3(1\mathrm{Al})\right]}{Q^1} \tag{3}$$

$$\frac{\mathrm{Al}^{IV}}{Si} = \frac{Q^3(1\mathrm{Al})}{\left[Q^1 + Q^2 + Q^2(1\mathrm{Al}) + Q^3 + 2Q^3(1\mathrm{Al})\right]} \tag{4}$$

Crosslinking occurs predominantly in low-Ca C-(N,K)-A-S-H gels, and ^{29}Si and ^{27}Al MAS NMR results indicate that the extent of crosslinking is promoted by increased overall Al content up to a ratio of approximately 1 Al per 6 chain sites [21,204]. However, the extent of crosslinking has been observed to decrease over time as the reaction proceeds, attributed to the lower Al-binding capacity of crosslinked gel components [21]. Study of laboratory synthesised gels has shown that the amount of Al which is able to substitute into the C-(N,K)-A-S-H gel appears to be limited to approximately $Al/Si \leq 0.2$, with C-(N,K)-A-S-H gel compositions typically within the range $0.5 < Ca/(Al + Si) \leq 1$ and $0 < Al/Si \leq 0.2$ [15,192,193,205]. The MCL of the aluminosilicate chains is often 7–10 tetrahedra for C-(N,K)-A-S-H gels produced by sodium silicate or potassium silicate activation of slag [18,206]; however, this depends on the Ca/(Al + Si) ratio.

There are conflicting reports regarding the mechanism of alkali uptake and relationship with Al content of the C-(N,K)-A-S-H gel. ^{23}Na MAS NMR analysis has indicated that alkali cations exist in two distinct environments within C-(N,K)-A-S-H gels [164,207,208]; the spectra show a sharp resonance at $\delta_{obs} = -7.6$ ppm (7.05 T, $\nu_R = 10$ kHz) [164] attributed to either a

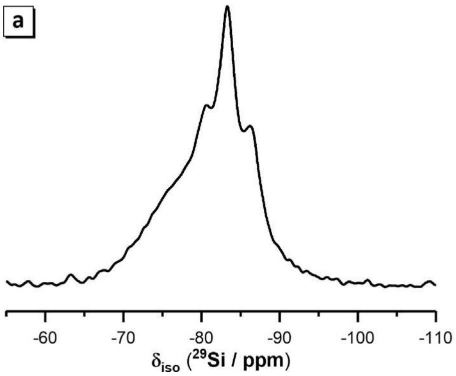

Fig. 17. (a) ^{29}Si MAS NMR spectra (14.1 T, $\nu_R = 10$ kHz) and (b) ^{27}Al MAS NMR spectra (14.1 T, $\nu_R = 10$ kHz) of an alkali-activated slag cured for 7 days. Adapted from Bernal et al., 2013 [20].

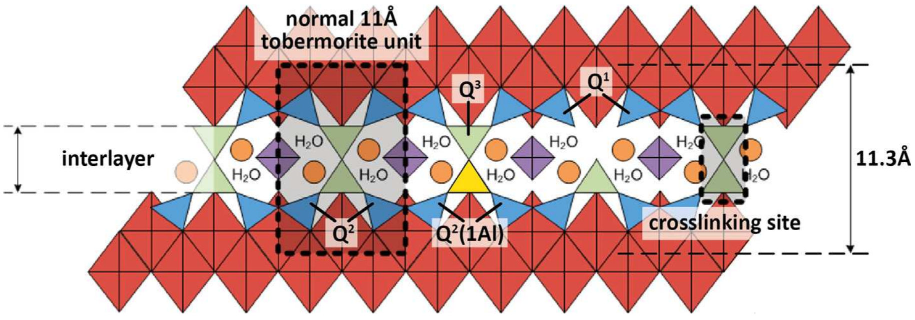

Fig. 18. Schematic representation of the structural features of C-(N)-A-S-H gels, adapted from Myers et al. [195]. Paired and bridging Si tetrahedra are represented by blue and green triangles, respectively, and intralayer calcium, charge-balancing alkali cations and interlayer protons and/or calcium cations by the red diamonds, orange circles and purple squares, respectively. The yellow triangle indicates Al substituting for Si in a bridging tetrahedral site.

highly symmetric bound alkali site or mobile alkali ions. An additional broad resonance at approximately $\delta_{obs} = -3$ ppm (14.1 T, $\nu_R = 10$ kHz) [14] to $\delta_{obs} = -10$ ppm (7.05 T, $\nu_R = 10$ kHz) [164] attributed to low-mobility Na within a disordered phase, possibly sorbed to the surface of the nanostructured gel.

Some observations suggest a direct correlation between Al content and alkali uptake [16,209], supported by an intuitive rationale of increased Al content driving an increase in alkali uptake to charge balance the AlO_4^- tetrahedra. However, other observations suggest an inverse proportionality between Al content and alkali uptake [210] or that Al content does not affect alkali uptake in the C-(N,K)-A-S-H gel [204,211,212]. Alkali uptake in C-A-S-H gels has been observed to be promoted by lower Ca/Si ratios and higher alkali concentration [213], presumably because lower levels of charge balancing Ca^{2+} increase the requirement for charge balancing by alkali cations. It has been suggested that charge balancing alkali cations in the C-(N,K)-A-S-H gel interlayer induce additional structural disorder by reducing the periodicity of the interlayer and reducing the regularity of the stacking of the layers due to differences in ionic size, indicating that incorporation of alkalis into C-(N,K)-A-S-H has a significant effect on gel nanostructure [13,214]. However, when ^{29}Si MAS NMR was used to investigate composition—solubility—structure relationships in synthetic C-(N,K)-A-S-H gels [204], it appeared that the C-(N,K)-A-S-H gel structure was actually becoming more (rather than less) crystalline in the presence of alkalis, with both Na and K incorporated into its interlayer space [213]. The additional structural disorder was observed in C-(N,K)-A-S-H gel systems with lower pH (~13 [214]) than those in which greater ordering was observed (pH > 13.5 [204,213]); it is, therefore, likely to be the higher pH of the more alkali-rich systems which drives rearrangement to more crystalline structures, rather than the alkali cations themselves. Elevated temperature also drives increased polymerisation, ordering and phase purity of synthetic C-(A)-S-H gel structures [215].

4.2.1.3. Other guest ions in C-S-H gels (C-S-(X)-H). In addition to Al^{3+} and Na^+, other ionic species may be incorporated into the C-S-H gel structure. Owing to the 100% natural abundance and high magnetogyric ratio of ^{19}F and ^{31}P, SS NMR experiments probing these nuclei have been very useful in elucidating the structural sites in which these atoms can exist within the C-S-H gel. ^{19}F MAS NMR has shown that interlayer hydroxyl species may be substituted by F^- [36,216]. Further analysis of F^- speciation in C-S-H by ^{19}F-^{29}Si-^{19}F forth and back (FB) CP MAS NMR (a modified double CP MAS NMR experiment which transfers polarisation forth and back between high- and low-γ spin nuclei [217]) confirmed the aforementioned observation of F^- for OH^- substitution in the interlayer, as well as revealing a second F site attributed to F^- ions associated with CaO_6 layers of a jennite-like part of the C-S-H gel [216,217].

PO_4^{3-} ions can also be incorporated in the interlayer of C-S-H gels. ^{31}P MAS NMR analysis of interlayer PO_4^{3-} ions exhibits a broad resonance which has the same chemical shift as the PO_4^{3-} ions in alite, so must be selectively detected using ^{1}H-^{31}P CP MAS NMR to enable it to be distinguished from the signal of remnant clinker in an incompletely hydrated paste [32,34].

4.2.1.4. C-S-H − X interactions. SS NMR has also found applications investigating sorption of ions onto cement binding gels [173,218,219]. Static ^{35}Cl NMR experiments and measurement of ^{35}Cl spin—lattice relaxation time constants (T_1) and spin—spin relaxation time constants (T_2) were used to study chloride sorption onto jennite (used as a model C-S-H phase) suspended in lime-saturated NaCl solution [218]. This was intended to simulate hydrated PC in service in marine environments and showed that chloride undergoes rapid exchange between surface and bulk solution sites and exists predominantly in a hydrated, solution-like chemical environment.

High-resolution ^{29}Si, ^{23}Na and ^{133}Cs MAS NMR was used to study the interaction of sodium and caesium chloride salts with synthetic C-S-H [173]; this work is of particular relevance to the nuclear industry as some caesium isotopes are important fission product radionuclides. This work showed that both Na^+ and Cs^+ cluster in hydrated C-S-H, while in dry C-S-H Na^+, formed outer-sphere complexes (adsorbed with their hydration sphere) and Cs^+ formed inner sphere complexes (bound directly to the surface with no intervening water molecules).

^{1}H, ^{13}C, ^{27}Al and ^{29}Si MAS NMR has been used to investigate the structure of the $CaCO_3$ polymorphs calcite, aragonite and vaterite [65,220], as well as K_2CO_3 [220], and their formation in hydrated PC (i.e. through carbonation) and interaction with PC hydrate phases [221]. This work showed that carbonation of hydrated PC occurs in two stages: gradual decalcification of C-S-H by removal of calcium from the interlayer and defect sites until Ca/Si = 0.67 is reached (corresponding to infinite silicate chains in a tobermorite-like structure), followed by further decalcification by removal of calcium from the gel layers and formation of a layered or three-dimensional silicate gel. The amount of carbonates formed is directly proportional to the Ca/Si ratio of the gel. The application of ^{13}C MAS and ^{1}H-^{13}CP MAS NMR also enabled carbonate anions in hydrous and anhydrous phases to be distinguished [65,220].

SS MAS NMR has been used to examine the interaction between a variety of organic additives and PC during hydration. Natural abundance ^{43}Ca and ^{13}C MAS NMR was used to examine the interaction between a poly(ethylene-vinyl acetate) (PEVAc) admixture, added to cement mortars to improve fracture toughness and impermeability, and hydrated white PC over the first 3 months of hydration. PEVAc hydrolysis occurs immediately as PC hydration commences, and induces minor structural changes to the hydrated PC, primarily formation of a small amount of amorphous, low-coordinated calcium sites [222]. This demonstrates that PEVAc admixtures do not induce significant structural changes to hydrated white PC and are therefore unlikely to be detrimental to the performance of these cements. Conversely, ^{1}H-^{13}C CP MAS NMR showed that when mixed with 15 wt % poly (vinyl alcohol) and 10 wt % mineral antiblocking agents, PEVAc does not hydrolyse in the alkaline solution of hydrating PC and was adsorbed to the surface of the cement binder [223,224]. This is particularly important in the context of both chemical and physical durability as PEVAc and other similar latex dispersions are commonly used as waterproofing agents and sealants in cements.

4.2.2. Alkali aluminosilicate ((N,K)-A-S-H) gels

SS MAS NMR studies of hydrous alkali aluminosilicate in the context of cements are relatively recent compared to those examining C-S-H and related phases in hydrated PC, with the first application probing ^{29}Si speciation in alkali hydroxide/silicate activated metakaolin cements in 1988 [115,225,226]. Since these first experiments, SS MAS NMR analysis probing ^{29}Si and ^{27}Al has played a pivotal role in determining the structure of alkali-activated aluminosilicate cements, including those known as 'geopolymers' [68,227]. The main reaction product of alkali activation of aluminosilicate precursors has been revealed to be a three-dimensional hydrous alkali aluminosilicate gel, consisting of highly crosslinked (predominantly q^4/Q^4) AlO_4^- and SiO_4 tetrahedra linked via bridging oxygen atoms, with a small number of terminal hydroxyl groups forming Q^3 sites. This structure is consistent across alkali aluminosilicate gels produced from reagent chemicals [228—231], calcined clays such as metakaolin [104,232—235], and aluminosilicate-rich waste materials such as coal FA

Table 6
Coordination, expected δ_{obs}, δ_{iso} and C_Q for different nuclei in (N,K)-A-S-H.

Nucleus	Site	Coordination	δ_{obs} (ppm)	δ_{iso} (ppm)	C_Q (MHz)	Magnetic field (T)	Reference
^{17}O	Si-$\underline{O}$-Si	2	–	39.0	1.26	14.10	[252,255,371]
	Si-$\underline{O}$-Al	2	–	33.0	1.00	14.10	[252,255,371]
	$H_2\underline{O}$	2	–	−9.8	0.55	14.10	[252,255,371]
^{23}Na	Charge balancing Na^+	6	−3 to −5	−1.26 to −2.60	0.70–1.41	11.7, 14.10	[112,255]
^{27}Al	q^4	4	58–60	61.0–66.3	1.4–1.9	14.10	[112,255,256]
^{29}Si	Q^4	4	−110 ± 6 ppm	−110 ± 6 ppm	–	7.5, 9.4, 14.1	[112,236,237,250,251]
	Q^4(1Al)	4	−102 ± 5 ppm	−102 ± 5 ppm	–	7.5, 9.4, 14.1	[112,236,237,250,251]
	Q^4(2Al)	4	−95 ± 4 ppm	−95 ± 4 ppm	–	7.5, 9.4, 14.1	[112,236,237,250,251]
	Q^4(3Al)	4	−90 ± 4 ppm	−90 ± 4 ppm	–	7.5, 9.4, 14.1	[112,236,237,250,251]
	Q^4(4Al)	4	−86 ± 4 ppm	−86 ± 4 ppm	–	7.5, 9.4, 14.1	[112,236,237,250,251]

[104,105,236–238]. This three-dimensional alkali aluminosilicate gel framework is often described as a highly crosslinked, disordered pseudo-zeolitic structure [13,239–243], and nanocrystalline zeolite phases have been observed as localised regions of ordering within the broadly less-ordered gel framework [239]. The short-range ordering has been observed by ^{29}Si and ^{27}Al MAS NMR spectroscopy [20,112,244,245] together with X-ray and neutron pair distribution function analysis [246–249] to extend to approximately 2–3 nearest neighbour shells. The expected δ_{obs}, δ_{iso} and C_Q for different nuclei in (N,K)-A-S-H gels are shown in Table 6 and discussed in the following text.

^{27}Al and ^{29}Si MAS NMR have shown that Al and Si are present in tetrahedral coordination, with Si existing in Q^4(mAl) environments where m is between 1 and 4 depending on the Al/Si ratio of the gel, and Al predominantly in q^4(4Si) environments due to the energetic penalty associated with Al-$\underline{O}$-Al bonding (Fig. 19) [236,237,250,251]. Reports of the observation of Al^{IV}-$\underline{O}$-Al^{IV} bonds within alkali-activated metakaolin have also been made for materials with Si/Al close to 1.0 using ^{17}O triple quantum (3Q) MAS NMR [252], despite these bonds being significantly less thermodynamically favourable than Al^{IV}-$\underline{O}$-Si^{IV} bonds, as entropic effects cause some violation of strict Si-Al ordering [250]. The negative charge associated with Al substitution for Si is balanced by hydrated alkali cations (Fig. 20) and is thought to be delocalised across all oxygen atoms, with the oxygen atom closest to the charge balancing alkali cation carrying the majority of this delocalised negative charge [114,252]. The (N,K)-A-S-H gel nanostructure is significantly influenced by kinetic limitations on silica and alumina release from solid precursors if these are used [253,254] and consequently evolves over time as the reaction process proceeds [237]. Schematic representations of the disordered N-A-S-H gel based on recent structural descriptions are shown in Fig. 20.

^{23}Na MAS NMR analysis of metakaolin-derived (N,K)-A-S-H gels (Fig. 21a) [111,257] identified a single disordered Na environment within the gel attributed to Na^+ in a charge-balancing role, whose chemical shift ($\delta_{obs} = -3.5$ to -6 ppm, $B_0 = 11.7$ T) was independent of the Si/Al ratio. Aqueous Na^+ ($\delta_{obs} = 0$ ppm, $B_0 = 11.7$ T) was also observed within the pore solution, charge-balancing $Al(OH)^-_{4(aq)}$ species, in samples with Si/Al $\leq$ 1.40. Charge balancing Na^+ sites resonating at a similar frequency ($\delta_{obs} = -4$ ppm, $B_0 = 14.1$ T) have also been observed in alkali aluminosilicate gels produced from synthetic precursors [228]. These sites resonate at similar frequencies to those of hydrated Na^+ ions in hydrothermally altered glass [258], providing opportunities to draw structural parallels to better understand the nature of the cementitious gels. K^+ ions in alkali aluminosilicate gels balance the charge deficit from $Al^{3+} \Leftrightarrow Si^{4+}$ substitution within the aluminosilicate framework and behave similarly to charge-balancing Na^+ ions [259,260] (Fig. 21b), and the incorporation of K^+ ions into the (N,K)-A-S-H gel is preferential compared to Na^+ ions when both are present.

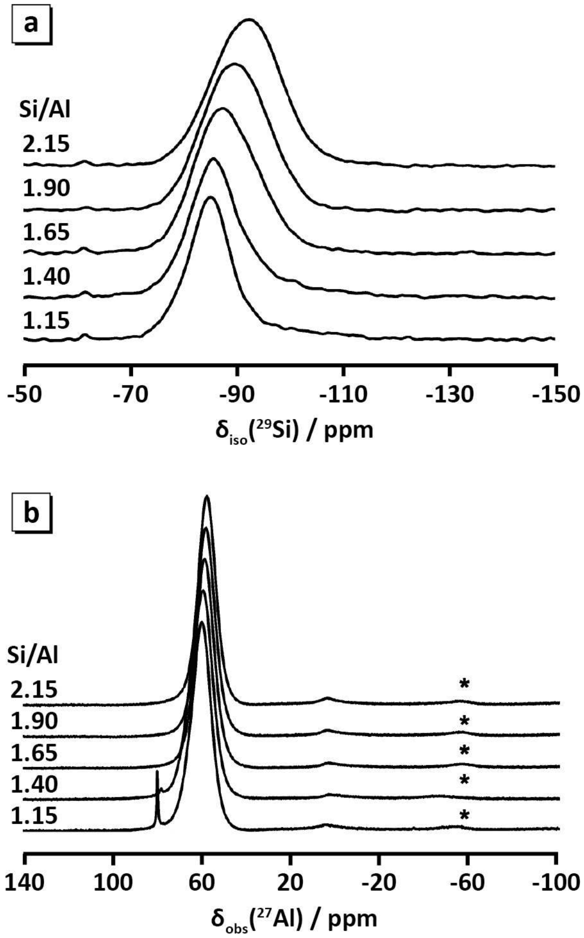

Fig. 19. (a) ^{29}Si MAS NMR spectra (7.05 T, $\nu_R = 5$ kHz) and (b) ^{27}Al MAS NMR spectra (11.7 T, $\nu_R = 15$ kHz) of N-A-S-H gels produced by reacting metakaolin with a sodium silicate solution (with Si/Al ratios as marked) and curing for 14 days. Adapted from Duxson et al. [111,112].

Related to this selectivity for larger alkali cations, SS NMR has also been applied to study the interaction of caesium with alkali aluminosilicate gels, to investigate their applicability in nuclear waste immobilisation applications. ^{133}Cs MAS NMR spectra of Cs-doped alkali aluminosilicate gels produced from metakaolin and sodium silicate exhibit a single broad asymmetric resonance at approximately $\delta_{obs} = 0$ ppm ($B_0 = 9.4$ T) [261] consistent with that of Cs^+ bound tightly to an aluminosilicate surface (such as that in kaolinite and illite [208,262]), strengthening the appeal of alkali aluminosilicate gels in nuclear waste immobilisation applications.

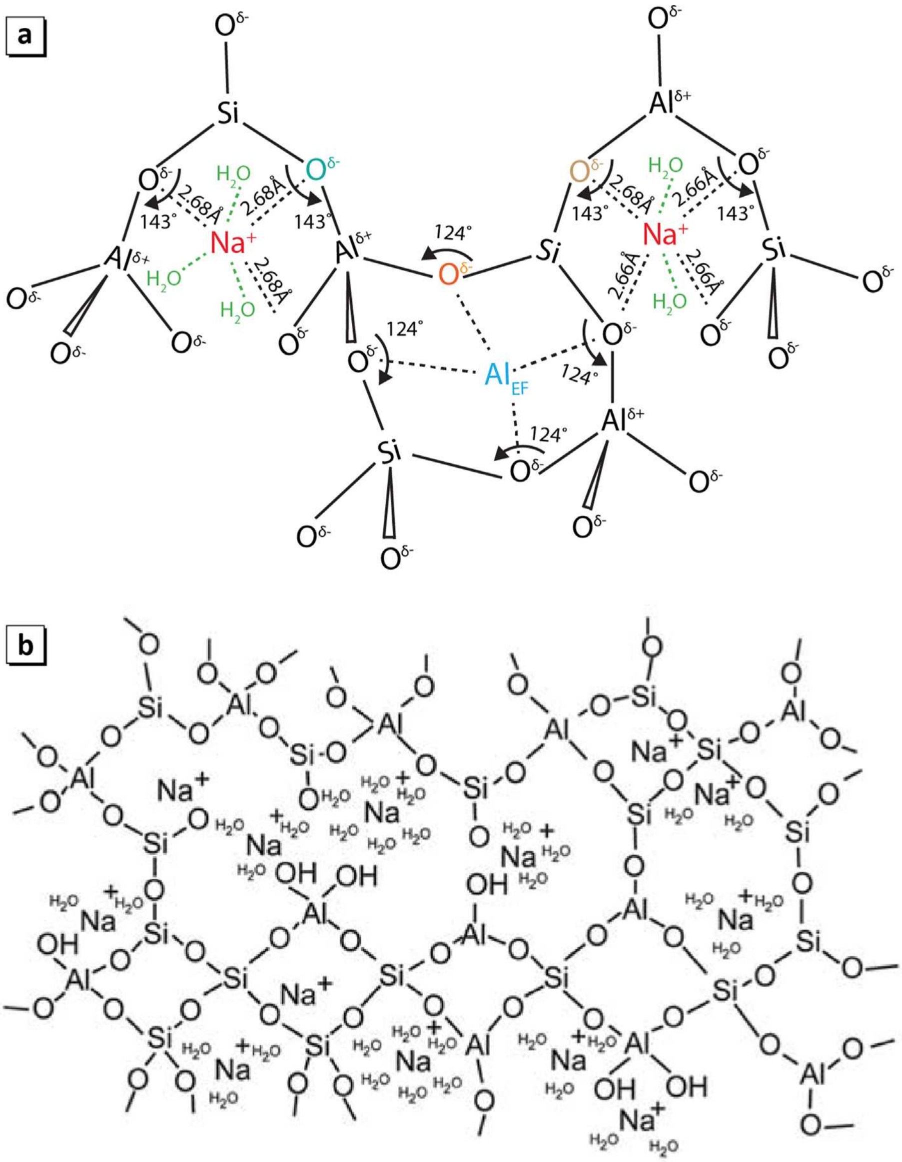

Fig. 20. (a) Schematic representation of a section of N-A-S-H gel adapted from Walkley et al. [255] showing charge-balancing sodium, charge-balancing extra-framework Al (Al_{EF}), bridging oxygen charge balanced by Na^+ and associated with three H_2O molecules, bridging oxygen charge balanced by Al_{EF} and bridging oxygen charge balanced by Na+ and associated with two H_2O molecules and (b) schematic representation of a section of N-A-S-H gel adapted from Rowles et al. [256].

4.2.3. Multiphase C-(N,K)-A-S-H/(N,K)-A-S-H gels

Coexistence of C-(N,K)-A-S-H and (N,K)-A-S-H gel frameworks occurs in many cement systems, including AAMs based on blends of high-calcium and low-calcium reactive precursors [20,263–265] (Fig. 22), and the gels appear to be stable in coexistence [14,20,231,266–268], as long as there is sufficient alkali content [117,266,269–271]. SS NMR has proven particularly useful in determining the structure and composition of these coexisting gel frameworks which are otherwise very difficult to discriminate. Owing to the structural similarity between these two gels, many resonances in their SS NMR spectra overlap; however, these can be distinguished and attributed appropriately with sound chemical reasoning and spectral deconvolution (discussed in section 4.3).

Using ^{27}Al and ^{29}Si MAS NMR, the growth of an N-A-S-H gel within alkali silicate-PC-dehydroxylated halloysite blends was shown to preferentially consume available Si within the system through rapid reactions involving the initially dissolved silica [270]. ^{27}Al and ^{29}Si MAS NMR of AAMs based on GGBFS-metakaolin blends [266], combined with high-resolution X-ray diffractometry [272,273], has also shown significant phase coexistence in these binders, although the dissolution of Ca^{2+} from the GGBFS, and subsequent reaction mechanisms, depends on both alkalinity and precursor chemistry.

Structural analysis via ^{29}Si, ^{1}H-^{29}Si CP MAS, ^{27}Al, ^{23}Na and ^{1}H MAS NMR of multiphase C-(N)-A-S-H and N-A-S-H gel frameworks within synthetic AAMs has also revealed strong dependence of reaction kinetics, gel composition and structure on precursor composition [14]. This work demonstrated that increased Ca content of the solid precursor (or blend of precursors) promotes the formation of low-Al, high-Ca C-(N)-A-S-H with lower MCL, whereas increased Al content promotes Al inclusion and reduced cross-linking within C-(N)-A-S-H, formation of an additional N-A-S-H gel and increased presence of secondary alumina-rich hydrate phases.

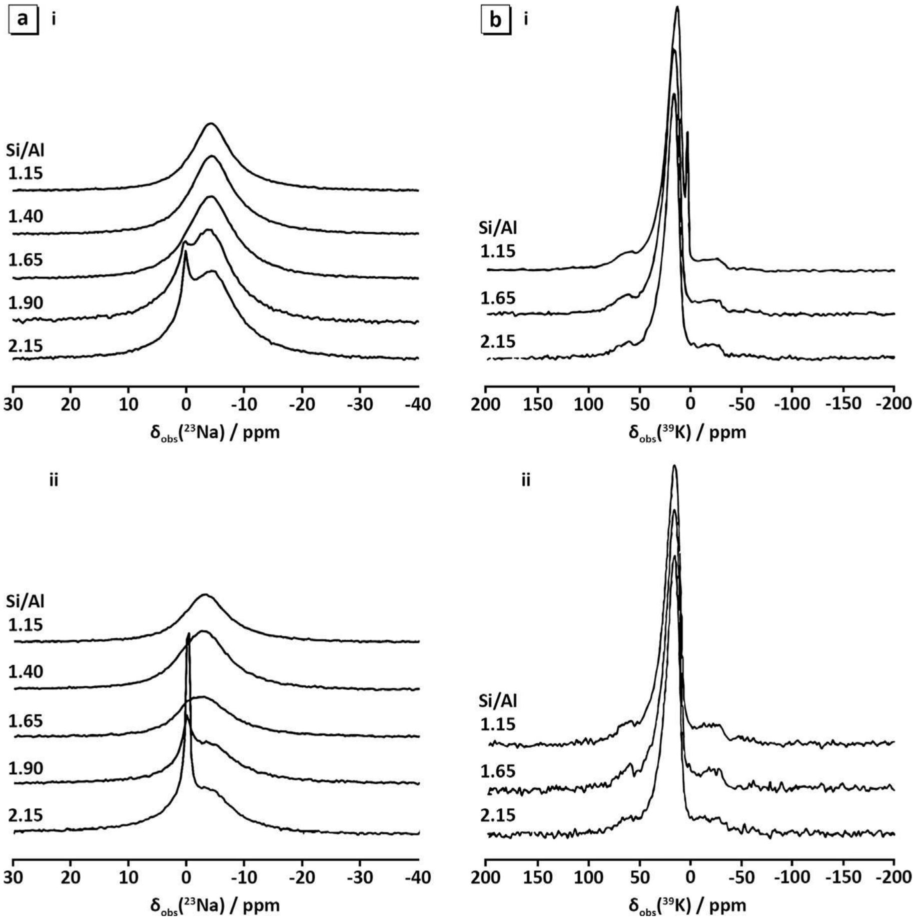

Fig. 21. (a) ^{23}Na MAS NMR spectra of (i) N-A-S-H and (ii) N-K-A-S-H gels with Si/Al ratios as marked and (b) ^{39}K MAS NMR spectra of (i) K-A-S-H and (ii) N-K-A-S-H gels with Si/Al ratios as marked. All mixed-alkali gels have Na:K = 1:1 on a molar basis, and all gels were produced by alkali activation of metakaolin. Adapted from Duxson et al. [111] and Duxson et al. [259].

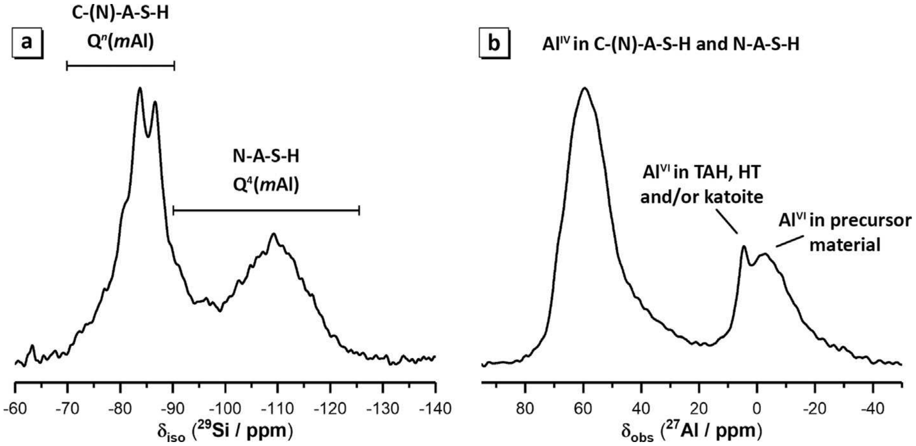

Fig. 22. (a) ^{29}Si MAS NMR spectra (14.1 T, $\nu_R = 10$ kHz) and (b) ^{27}Al MAS NMR spectra (14.1 T, $\nu_R = 10$ kHz) of an alkali-activated 50% wt. slag/50% wt. fly ash blend cured for 14 days, with coexistence of C-(N)-A-S-H and (N,K)-A-S-H gels. The ^{29}Si MAS NMR spectrum shown in (a) exhibits resonances due to $Q^n(m\text{Al})$ ($1 \le n \le 3$ and $m \le n$) species in C-(N)-A-S-H and $Q^4(m\text{Al})$ ($m \le n$) in N-A-S-H, while the ^{27}Al MAS NMR spectrum shown in (b) exhibits resonances due to Al^{IV} species in both C-(N)-A-S-H and N-A-S-H, as well as Al^{VI} species in unreacted precursor material and the additional reaction products hydrotalcite (HT), the third aluminate hydrate (TAH) and katoite. Adapted from Bernal et al. [20].

4.2.4. Hydrated CACs

CACs comprising primarily CA (with smaller quantities of CA_2 and/or $C_{12}A_7$) hydrate to form mixtures of the microcrystalline metastable phases CAH_{10} and C_2AH_8, followed by conversion to the stable phases C_3AH_6 and amorphous AH_3 [122,274]. The expected δ_{obs}, δ_{iso} and C_Q for ^{27}Al in hydrated CACs are shown in Table 7 and discussed in the following text; information for other nuclei within these phases is not available in the open literature.

Skibsted et al. [52] used ^{27}Al MAS NMR to identify overlapping resonances attributed to octahedral Al environments in the stable

Table 7
Coordination, expected δ_{obs}, δ_{iso} and C_Q for different nuclei in hydrated calcium aluminate cements.

Nucleus	Site	Coordination	δ_{iso} (ppm)	C_Q (MHz)	Magnetic field (T)	Reference
^{27}Al	Al in CAH_{10}	6	10.2	2.4	7.1, 9.4 and 11.7	[52]
	Al in C_2AH_8	6	10.3	1.2	7.1, 9.4 and 11.7	[50,276]
	Al in C_3AH_6	6	12.36	0.71	7.1, 9.4 and 11.7	[52]
	$Al^{IV}{}_1$ in AH_3	6	10.4	1.97	7.1, 9.4 and 11.7	[52]
	$Al^{IV}{}_2$ in AH_3	6	11.5	4.45	7.1, 9.4 and 11.7	[52]

C_3AH_6 (δ_{iso} = 12.3 ppm, C_Q = 0.705 MHz) and amorphous AH_3 ($\delta_{obs} = 8$ ppm at $B_0 = 9.4$ T) phases in CAC hydrated for 28 days; the isotropic chemical shift for C_3AH_6 was determined via simulation of the spinning sidebands associated with this phase. Analysis of synthetic CAH_{10} at multiple fields exhibited a broad resonance in the octahedral Al region of the ^{27}Al MAS NMR spectrum and allowed determination of δ_{iso} = 10.2 ppm and 1.9 MHz $\leq C_Q \leq$ 2.6 MHz for this site. These results are consistent with previous data acquired at lower field [275]. Subsequent work examined CAC hydrate phases using ^{27}Al MAS [50,276] and MQMAS [276] NMR, enabling determination of δ_{iso} = 10.3 ppm and C_Q = 1.2 MHz for the octahedral Al site in the metastable C_2AH_8 phase and δ_{iso} = 11.9 ppm and C_Q = 4.3 MHz for the amorphous AH_3 phase.

Because of the clear distinction between Al environments in hydrated (Al^{VI}) and anhydrous (Al^{VI}) CAC, the degree of hydration of this cement may be readily determined from ^{27}Al MAS NMR (Fig. 23) [44,50,51]. This, however, relies on the assumption that all Al resonances within the ^{27}Al MAS NMR spectra are observable and quantified correctly; this is not always the case due to the presence of 'NMR invisible' Al species (see section 4.3).

^{27}Al, ^{31}P and ^{1}H-^{31}P CP MAS NMR has also been used to show that modification of CAC by addition of phosphate prevents the loss of material performance which is caused by the conversion from the metastable calcium aluminate hydrates to stable C_3AH_6 in hydrated CAC. Instead, phosphate modification yields an apparently stable amorphous calcium aluminophosphate gel comprising both Al^{IV} and Al^{VI} sites [277]. In these materials, phosphorus is present in hydrous environments with varying, but mostly low, degrees of crosslinking.

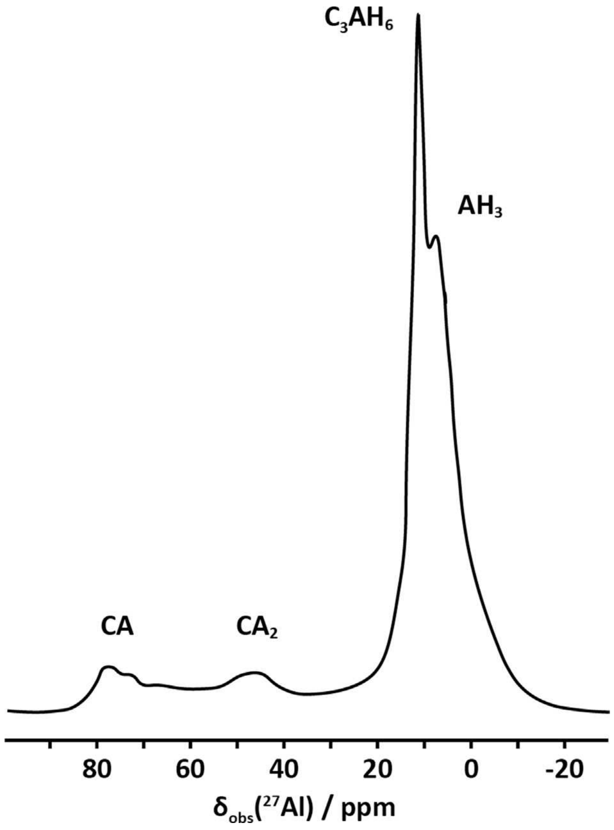

Fig. 23. ^{27}Al MAS NMR spectrum (9.4 T, ν_R = 13.1 kHz) of a calcium aluminate cement hydrated for 28 days. The degree of hydration, estimated by integration of the Al^{IV} and Al^{VI} spectral regions, is 86 ± 1%. Adapted from Skibsted et al. [52].

4.2.5. Hydrated CSA cements

Ye'elimite ($C_4A_3\$$) hydrates in the presence of calcium sulphate ($C\$$, added as gypsum or in dehydrated forms) to form ettringite ('AFt', $Ca_6Al_2(SO_4)_3(OH)_{12}\cdot 26H_2O$, see section 4.2.8.2), calcium monosulfoaluminate hydrate ('monosulphate AFm', $3CaO\cdot(Al,Fe)_2O_3\cdot CaSO_4\cdot nH_2O$, see section 4.2.8.3) and microcrystalline aluminium hydroxide ($Al(OH)_3$), with the proportion of each phase dependent on the $C_4A_3\$/C\$$ ratio [278]. The presence of belite along with these phases in a CSA cement, which is common because of the prohibitive cost of Si-free Al sources for cement manufacture, results in the formation of strätlingite ($2CaO\cdot SiO_2\cdot Al_2O_3\cdot 8H_2O$; a silica-substituted AFm phase, see section 4.2.8.3) and/or C-S-H as additional reaction products. As mentioned in section 4.1.2.2.2, CSA clinkers can also contain $C_5S_2\$$ (ternesite), which hydrates along with alumina-bearing clinker constituents to form strätlingite [279,280]. Most commercial CSA cements also contain C_4AF (section 4.1.1.4) as the economically viable alumina sources used in cement manufacture also contain significant quantities of Fe; this will typically hydrate (in both CSA and PC cements) more slowly than the hydraulic aluminate phases and yields Fe-substituted forms of many of the same AFm and AFt hydrate phases [281–283].

SS NMR studies of hydrated CSA (synthetic and commercial) and CSA/PC blends have shown narrow ^{27}Al MAS NMR resonances for octahedral Al in ettringite and monosulphate at approximately δ_{obs} = 13 ppm and 10.2 ppm (B_0 = 14.1 T), respectively, as well as a broad low-intensity resonance at δ_{obs} = 9 ppm at the same field which is attributed to $Al(OH)_3$ [133–135,284,285], consistent with the resonances of pure phases in synthetic samples, section 4.2.4 [52,286,287]. As with CAC, the clear distinction between Al environments in hydrated (Al^{VI}) and anhydrous (Al^{VI}) CSA allows the degree of hydration of aluminium-containing phases to be readily determined from ^{27}Al MAS NMR. This has shown that aluminium-containing phases generally react to form hydrates within 24 h [133–135,284]. Monitoring the degree of hydration in CSA/PC blends is significantly more difficult due to the presence of Al^{IV} sites in C_3A and C-(A)-S-H phases [133], as well as the presence of Fe which can severely dampen and shift the NMR signal of these nuclei [10]; however, it is made possible by spectral deconvolution using appropriate models and constraints (see section 4.3).

4.2.6. *Magnesium silicate hydrate (M-S-H) gels*

Magnesium silicate hydrate (M-S-H) cements are commonly produced from MgO and silica fume via hydrothermal or ambient-temperature processes [288–292], and generally comprise a talc-like or serpentine-like phase [141,293], although there remains some debate around the most appropriate structural model for M-S-H. ^{29}Si MAS NMR spectra of M-S-H cements exhibit as many as five distinct ^{29}Si MAS NMR resonances, attributed to Q^1, Q^2, two Q^3 and Q^4 sites [142,146,292,294–298]. The major component of the ^{29}Si MAS NMR spectra is a Q^3 resonance at approximately $\delta_{iso} = -93$ ppm and the Q^1 and Q^2 resonances are typically broad [142,292], indicating the disordered nature of the gel. These environments have been attributed to Si sites within a disordered phase structurally similar to talc ($Mg_3Si_4O_{10}(OH)_2$) [296] and/or serpentine-group minerals (polymorphs of $Mg_3(Si_2O_5)(OH)_4$, such as chrysotile, lizardite and antigorite) [142], with Mg/Si ratios ranging from 0.57 to 1.3 [291,293,298].

Alkaline earth aluminosilicate hydrate gel (magnesium aluminosilicate hydrate, M-A-S-H) has also been reported [299]. MAS NMR of these materials synthesised from sepiolite ($Mg_4Si_6O_{15}(OH)_2 \cdot 6H_2O$) and chrysotile ($Mg_3(Si_2O_5)(OH)_4$) resolved similar Q^3 ^{29}Si MAS NMR resonances at −90 ppm, and tetrahedral Mg sites from ^{25}Mg MAS NMR.

4.2.7. *Magnesium potassium phosphate cements (MKPC)*

Magnesium potassium phosphate cement (MKPC) is a clinker-free acid–base cement which reacts to form struvite-K ($MgKPO_4 \cdot 6H_2O$) as a crystalline main strength-giving phase; this phase is structurally analogous to the natural mineral struvite, $NH_4MgPO_4 \cdot 6H_2O$, but without requiring the presence of ammonium cations for its synthesis [141,300–302]. Application of SS NMR to investigate structural and phase evolution in MKPC is relatively recent, with the most extensive analysis probing ^{25}Mg, ^{27}Al, ^{29}Si, ^{31}P and ^{39}K nuclei in MKPC blended with FA and with GGBFS [303]. Struvite-K exhibits a ^{31}P resonance at $\delta_{obs} = 6.2$ ppm [303], which correlates well with the chemical shift of struvite, $\delta_{obs} = 6.1$ ppm [304]. A shoulder on this resonance at $\delta_{obs} = 4$ ppm was observed in MKPC/FA blends (but not MKPC/GGBFS blends) and was suggested to result from the presence of a disordered and/or partially substituted struvite-K phase. The predominant crystalline struvite-K phase exhibits ^{25}Mg and ^{39}K resonances at $\delta_{iso} = -1.0$ ppm ($C_Q = 3.8$ MHz) and $\delta_{iso} = -73.1$ ppm ($C_Q = 2.2$ MHz), consistent with previous observations for synthetic versions of this phase [305,306]. An amorphous orthophosphate environment was also identified, which has no intimate interaction with hydrogen and no measurable Al interactions [303].

4.2.8. *Additional reaction products*

Many additional reaction products are also formed along with the main silicate gels during hydration of the cements discussed previously and will be discussed in turn in this section. These additional reaction products are often intimately mixed with the dominant silicate gel frameworks [7,231] and can significantly influence the phase evolution and nanostructural development of these hydrate phases. The expected δ_{obs}, δ_{iso} and C_Q for different nuclei in the additional reaction products observed in hydrated PC, CAC, CSA and magnesia-based cements, as well as cements based on alkali metal or alkali earth aluminosilicate chemistry, are shown in Table 8.

4.2.8.1. *Portlandite.*

Portlandite ($CaOH_2$), also called slaked lime, is a common reaction product in hydrated PC and is also present as a reaction product or remnant precursor in pozzolanic or slag-based binders activated with lime. In general, portlandite forms when the Ca/Si ratio is significantly higher than can be accommodated by C-

Table 8
Coordination, expected δ_{obs}, δ_{iso} and C_Q values for different nuclei in various additional reaction products in hydrated PC, CAC, CSA and magnesia-based cements, as well as cements based on alkali metal or alkali earth aluminosilicate chemistry.

Phase	Nucleus	Site	Coordination	δ_{obs} (ppm)	δ_{iso} (ppm)	C_Q (MHz)	Magnetic field (T)	Reference
Portlandite	^{1}H	Ca-$\underline{O}$-H	1	0.7	0.7	–	7.04, 9.4, 11.7	[180,182,310]
	^{43}Ca	Ca-$\underline{O}$	6	50–60	–	–	7.04, 11.7 and 21.1 T	[309]
Aluminate ferrite trisulphate (AFt) (ettringite)	^{27}Al	$Al^{VI}{}_1$	6	–	13.08	0.391	7.1, 9.4, 11.7, 14.1 and 22.3	[52,137]
		$Al^{VI}{}_2$	6	–	13.51	0.337	7.1, 9.4, 11.7, 14.1 and 22.3	[52,137]
	^{33}S	SO_4^{2-}	4	–	330	0.7	14.1, 19.6	[59,316]
	^{43}Ca	Ca^{2+}		8	–	–	8.45, 11.75	[40]
Thaumasite	^{29}Si	Si^{VI}	6	−179.6	−179.6	–	4.7, 9.4	[318–320]
	^{33}S	SO_4^{2-}	4	–	330.9	0.95	14.1	[316]
Aluminate ferrite monosulphate (AFm) family	^{27}Al	Al^{VI}	6	–	11.8	1.7	7.1, 9.4 and 11.7	[52]
OH-AFm (C_4AH_{13})	^{27}Al	Al^{VI}	6	–	10.2	1.8	7.1, 9.4 and 11.7	[52]
(Al,Si)-AFm (strätlingite)	^{27}Al	Al^{IV}	4	61	–	–	14.1	[137,333]
	^{27}Al	Al^{VI}	6	11.3	–	–	14.1	[137,333]
Third aluminate hydrate	^{27}Al	Al^{VI}	6	5	–	–	14.1	[172,194,337]
Hydrotalcite-group phases (MgAl-layered double hydroxides)	^{1}H	Mg_3OH	1	1.3	1.3	–	11.7	[354]
	^{1}H	Mg_2AlOH	1	5.0	5.0	–	11.7	[354]
	^{13}C	CO_3^{2-}	4	170.9	170.9	–	7.05, 9.4, 14.1	[220]
	^{17}O	Mg_3OH	2	–	53.0	6.6	9.4, 16.4	[355]
		Mg_2AlOH	2	–	64.8	6.2	9.4, 16.4	[355]
	^{25}Mg	$Mg(OAl)_3(OMg)_3$	6	–	13.7	4.5	19.6	[354]
	^{27}Al	$Al(OMg)_6$	6	–	11.8	1.55	8.45	[354]
Hydrogarnet family (katoite)	^{27}Al	AlO_6 in C_3AH_6	6	–	12.36	0.71	7.1, 9.4 and 11.7	[52,362]
	^{29}Si	$[Si(OAl)_{4-x}]^{VI}(OCa)_x$	4	−79.9	−79.9	–	9.4	[50]

S-H or related phases [307]. It consists of layers of octahedrally coordinated Ca bound to oxygen atoms in tetrahedral coordination [23] with hydrogen occupying a single crystallographic site. It is a key participant in longer term phase evolution of C-(A)-S-H gels in blended PC cements via the pozzolanic reaction [308]. High-field natural abundance ^{43}Ca MAS NMR of portlandite [179] and ^{43}Ca MAS NMR of isotopically enriched portlandite at multiple fields [309] have shown a single quadrupolar resonance centred at approximately δ_{obs} = 50–60 ppm (7.04, 11.7 and 21.1 T) corresponding to a single Ca environment where Ca is octahedrally coordinated by six hydroxyl groups. Correspondingly, ^{1}H MAS NMR spectra of portlandite exhibit a single resonance at δ_{iso} = 0.7 ppm from the single Ca-$\underline{\mathrm{O}}$-H site [180,182,310]. Chloride sorption onto portlandite in portlandite suspensions has been studied using static ^{35}Cl NMR experiments and measurement of ^{35}Cl spin–lattice relaxation time constants (T_1) and spin–spin relaxation time constants (T_2) [218]. Chloride on portlandite exists predominantly in a hydrated, solution-like chemical environment and is rapidly exchanged between the surface and bulk solution. Portlandite quantification in hydrated cements by NMR is not usually attempted, as neither ^{43}Ca nor ^{17}O nuclei are particularly straightforward to use in such studies, and other techniques such as thermogravimetry and X-ray diffraction (XRD) can give reliable quantitative results for this phase much faster and less expensively.

4.2.8.2. 'Aluminate ferrite trisulphate'–type phases. Ettringite is the archetypal 'aluminate ferrite trisulphate' (AFt) phase, with a columnar hydrous CSA structure and a very high water content (up to 32 water molecules per formula unit) [311]. Ettringite forms rapidly in the earliest stages of hydration of PC, as C_3A reacts with gypsum, or equivalently through hydration of ye'elimite with excess gypsum in CSA cements. Early ^{27}Al MAS NMR experiments (9.4 T) examining ettringite displayed a resonance at δ_{iso} = 13 ppm that appeared characteristic of a single octahedrally coordinated AlO_6 site [52], which contrasted with the then-proposed crystal structure of ettringite which contained two distinct octahedral AlO_6 sites [312]. Recent work using ultra–high-field (22.3 T) ^{27}Al MAS and MQMAS NMR (Fig. 24) has in fact been able to resolve two distinct octahedrally coordinated AlO_6 sites in synthetic ettringite [137], consistent with the now well-accepted crystal structure solved by Moore and Taylor [312]. The two AlO_6 sites resonate at δ_{iso} = 13.08 and 13.51 ppm and are highly symmetric, displaying very small quadrupolar coupling parameters of C_Q = 0.391 MHz and 0.337 MHz, respectively. The high symmetry and very similar isotropic chemical shifts of these resonances are due to very small variations in Al-O bond lengths between sites, consistent with high-resolution powder XRD [313], single-crystal XRD and DFT calculations [311]. As a consequence of the small distinction in isotropic chemical shift values, these resonances remained unresolved for more than two decades in ^{27}Al MAS NMR spectra acquired at lower fields [22,52,57,117,135,186,187,314,315]. This demonstrates the importance of acquiring high-field spectra for quadrupolar nuclei in complex phases, even where crystallinity is high (as in the case of ettringite) and for relatively 'accessible' nuclei such as ^{27}Al.

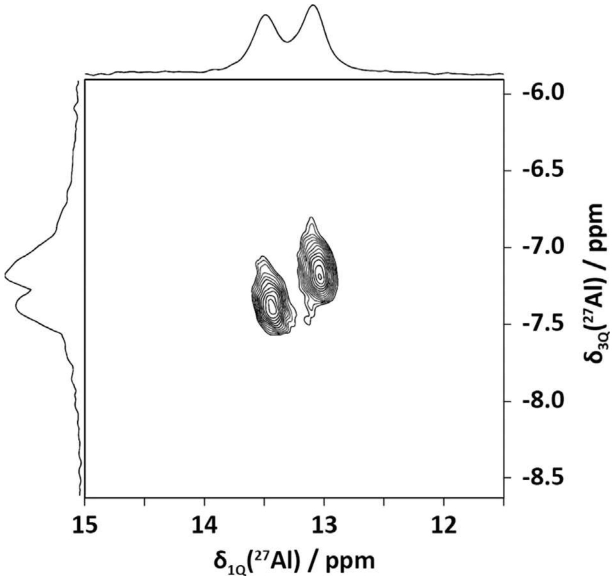

Fig. 24. ^{27}Al MQMAS NMR spectrum (23.3 T, ν_R = 15 kHz, −5 °C sample temperature) of ettringite showing two distinct Al^{IV} sites. Adapted from Skibsted et al. [137].

Natural abundance ^{43}Ca MAS NMR analysis of ettringite also resolved only a single ^{43}Ca resonance (δ_{obs} = 8 ppm) [40] despite the existence of two Ca sites in the crystal structure; this can be attributed to the structural similarity between the two Ca sites in ettringite and the poor signal-to-noise ratio of the spectrum resulting in poorly defined overlapping quadrupolar lineshapes for each site. High-field natural abundance ^{33}S MAS NMR [59] and single-enhanced wideband uniform rate smooth truncation (WURST) and hyperbolic secant (HS) MAS NMR spectroscopy probing ^{33}S [316] identified a single narrow resonance (δ_{iso} = 330 ppm, C_Q = 0.7 MHz) attributed to the single sulphur site in ettringite, which has a high degree of symmetry as it is within a discrete sulphate anion.

Thaumasite ($Ca_3Si(OH)_6(CO_3)(SO_4)\cdot 12H_2O$) is a silicate- and carbonate-substituted AFt phase which can form by reaction of sulphate and carbonate ions with cement minerals (i.e. during sulphate attack of PC systems) [317]. This similarity has caused difficulty distinguishing thaumasite from ettringite using XRD, infrared spectroscopy or thermogravimetric techniques. However, thaumasite exhibits a ^{29}Si MAS NMR resonance at δ_{iso} = −179.6 ppm [318–320], corresponding to Si in a very unusual sixfold coordination, meaning that it is readily identifiable by this technique. ^{1}H-^{29}Si CP MAS NMR has been used to identify and quantify thaumasite in PC systems containing carbonate and sulphate additives and revealed that significant quantities of thaumasite can form in cements with negligible Al content [320]. WURST and HS MAS NMR spectroscopy probing ^{33}S [316] in thaumasite identified a single narrow resonance (δ_{iso} = 330.9 ppm, C_Q = 0.95 MHz), consistent with its crystal structure in which sulphur exists in a single SO_4^{2-} crystallographic site [321], as in ettringite.

4.2.8.3. 'Aluminate-ferrite-monosulphate'–type phases. Calcium monosulfoaluminate and similar hydrocalumite-like AFm phases are observed in many types of cements, including PC [117,322,323], CSA cements [133–135,284,285] and many alkali-activated slag cements [154,324–326]. AFm phases are layered double hydroxide (LDH)–type structures, with positively charged portlandite-like layers containing one-third of Al^{3+} or Fe^{3+} cations as substituents for Ca^{2+}, balanced by anionic species (commonly SO_4^{2-}, CO_3^{2-} and OH^-), and with significant interlayer H_2O [327–330] (Fig. 25). They can be represented by the general formula $[Ca_2(Al,Fe)(OH)_6]\cdot X\cdot xH_2O$, where X represents an exchangeable singly charged (e.g. OH^-) anion or half of a doubly charged anion (e.g. SO_4^{2-}, CO_3^{2-}) [322]. With the exception of OH^-/SO_4^{2-} substitution (up to 50 mol %) [322], these phases generally do not form extensive solid solutions but rather can coexist as separate phases with closely related structures but differing interlayer anions. Consequently, many hydrated cement systems contain mixtures of distinct AFm phases. AFm phases in hydrated PC typically contain the anions SO_4^{2-} (termed monosulphate), CO_3^{2-} (monocarbonate) and/or OH^- (hydrocalumite, C_4AH_{13}) in the interlayer [52,117,322,323,331], while those in alkali-activated slags and metakaolin-rich PC blends commonly contain interlayer divalent aluminosilicate anions, $[AlSi(OH)_8]_2^{2-}$, forming an AFm structure, which is also given the mineral name strätlingite [154,324]. Substitution by multiple anions in ordered positions is also possible, for example, 1:1 hydroxide and carbonate to form hemicarbonate or 1:1 sulphate and chloride to form Kuzel's salt [322]. Friedel's salt ($3CaO \cdot Al_2O_3 \cdot CaCl_2 \cdot 10H_2O$) is also observed in hydrated PC, which has been exposed to a source of chloride, e.g. when serving in marine environments or cold climates with road salting.

These phases each exhibit a single ^{27}Al MAS NMR resonance at approximately $\delta_{obs} = 10-12$ ppm, depending on field strength [52,117,133], in accordance with their crystal structures containing Al^{VI} [327,332]. Owing to similarities in structure, each of these AFm phases exhibits very similar ^{27}Al MAS NMR resonances at standard field strengths, and so they are more often distinguished from each other via complementary techniques, e.g. XRD, where their different basal spacings can be observed. The monosulphate and monocarbonate ^{27}Al MAS NMR resonances are severely overlapping ($\delta_{obs} = 12$ ppm), but evidence for more than one peak in this region has been observed by ultra−high-field ^{27}Al MAS NMR (23.3 T) [137], suggesting that it may be possible to resolve these resonances, and those of C_4AH_{13}, at ultrahigh field. The sorption of chloride onto the monocarbonate AFm phase C_4ACH_{11} was investigated by static ^{35}Cl NMR experiments and measurement of ^{35}Cl spin−lattice relaxation time constants (T_1) and spin−spin relaxation time constants (T_2) [218], showing that chloride is in rapid exchange between adsorbed surface sites and bulk solution sites in each phase and exists predominantly in a hydrated, solution-like chemical environment on the monocarbonate surface. This behaviour is similar to chloride sorption onto portlandite and onto jennite, as discussed previously.

Strätlingite ($Ca_4Al_2(OH)_{12}[AlSi(OH)_8]_2 \cdot 2H_2O$) is an AFm phase which forms as a hydration product of aluminium-rich cements including PC-metakaolin blends and some non-Portland binders. ^{27}Al MAS NMR analysis of hydrated white PC-metakaolin blends [117] and hydrated CSA [137], as well as synthetic strätlingite [333], revealed two resonances at $\delta_{obs} = 61$ ppm and 11.3 ppm (14.1 T) attributed to Al^{IV} and Al^{VI} sites, respectively. These resonances are characteristic of the crystal structure of strätlingite [334], which contains Al^{IV} in a double-tetrahedral environment as part of the aluminosilicate interlayer anion ($[(T,\square)_4(OH,O)_8 \cdot 0.25H_2O]^-$, T = Si or Al, $\square$ = vacancy), as well as the Al^{VI} in the brucite-type layer ($[Ca_2Al(OH)_6 \cdot 2H_2O]^+$) that defines the AFm structure. The Al^{VI} site in strätlingite resonates at a similar frequency to Al^{VI} sites in monosulphate, and consequently strätlingite is more conclusively identified from its Al^{IV} resonance, unless working at extremely high fields. The ^{27}Al MAS NMR spectrum of hydrated CSA collected at $B_0 = 22.3$ T appears to contain contributions from several individual overlapping Al^{VI} resonances [137], suggesting that monosulphate, monocarbonate and strätlingite may be able to be resolved in ^{27}Al MAS or MQMAS NMR spectra acquired at ultra-high magnetic field.

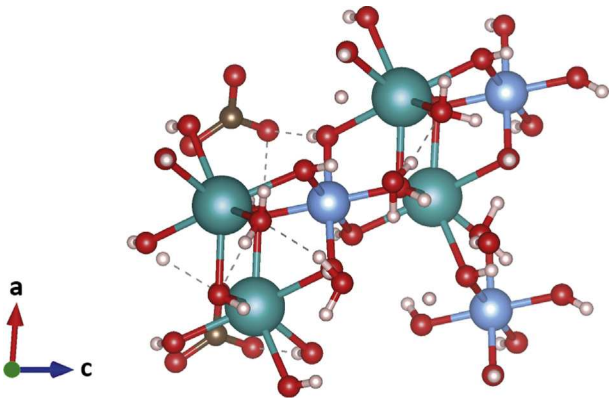

Fig. 25. Illustration of the local environments in the crystal structure of the monocarbonate AFm phase $[Ca_4Al_2(OH)_{12}]CO_3 \cdot 5H_2O$ obtained from single-crystal diffraction data [329]. Ca atoms are represented by cyan spheres, Al atoms are represented by blue spheres, O atoms are represented by red spheres and H atoms are represented by light pink spheres. Prepared using the VESTA software package [128].

The ^{29}Si MAS NMR spectrum of synthetic strätlingite exhibits a broad resonance at approximately $\delta_{obs} = 86.5$ ppm, containing contributions from resonances resulting from $Q^3(3Al)$, $Q^2(2Al)$, $Q^2(1Al)$ and Q^2 sites [333,335], consistent with the crystal structure [334] of strätlingite which contains double tetrahedral silicate ring structures. The presence of these resonances is often used to monitor hydration in PC-CSA blends [133].

As mentioned previously, Friedel's salt is an AFm phase with Cl^- as its interlayer ion. Variable temperature static ^{35}Cl NMR has shown that interlayer Cl^- in Friedel's salt exhibits a resonance at $\delta_{iso} = 30$ ppm with a quadrupolar coupling constant $C_Q = 2.22-2.87$ MHz, indicating uniaxial symmetry above 0 °C resulting from dynamically averaged interlayer species [336]. Below 0 °C, the Cl^- in this site exhibits reduced (triaxial) symmetry resulting from a rigid crystal structure, as indicated by a resonance at $\delta_{iso} = 26$ ppm with a quadrupolar coupling constant $C_Q = 3.0$ MHz.

4.2.8.4. *Third aluminate hydrate.* The ‘third aluminate hydrate’ (TAH) phase is an amorphous nanoscale aluminate hydrate phase which precipitates at the surface of the C-S-H−type gels formed during PC hydration [172,194,337] and which has also been noted in sodium silicate−activated GGBFS [18,20,155,324]. TAH is to date only identifiable by NMR, and consequently, the technique is key to the discovery of its existence. TAH is described as a poorly ordered $Al(OH)_3$ phase [194,337] which is intimately mixed with other hydrate phases. Stoichiometric arguments and thermodynamic modelling suggest that the presence of TAH is likely to be linked to high concentrations of available Ca and Al [154,338,339], as the opposing charges on C−S−H and AFm phases may produce strong mutual attractions and physically destroy the AFm crystals [22,340], which would then result in low-crystallinity aluminate (AFm-like) layers being dispersed throughout the C−S−H gel while being undetectable by XRD [22]. This hypothesis is supported by transmission electron microscopy observations [337]. TAH phases exhibit a ^{27}Al MAS NMR resonance at $\delta_{obs} = 5$ ppm (14.1 T) in the spectra of C-S-H−type gels [172,194,337] and of sodium silicate−activated GGBFS [18,20,155,324]. Broadening of the ^{29}Si MAS NMR resonance attributed to Q^1 Si species in sodium silicate−activated slags [155] is attributed to the presence of Al^{VI}-$\underline{O}$-Si linkages between TAH and C-S-H.

4.2.8.5. *Hydrotalcite-group phases.* Hydrotalcite ($Mg_6Al_2CO_3(OH)_{16}[CO_3] \cdot 4H_2O$), Fig. 26) is an Mg-Al LDH mineral with a primary layer of positively charged brucite-like sheets (see section 4.1.2.2.3), comprising octahedrally coordinated Mg bound to oxygen atoms in tetrahedral coordination, with partial replacement of Mg^{2+} by trivalent octahedrally coordinated cations, which are Al in the case of true hydrotalcite [341]. The Al atoms are randomly distributed within these layers at low concentrations [342] but take on a significantly more ordered configuration at the higher concentrations which are more characteristic of hydrotalcite-group phases observed in cements [23]. A secondary layer contains H_2O molecules and anions, most commonly carbonate, CO_3^{2-}, and hydroxyl, OH^-, which are

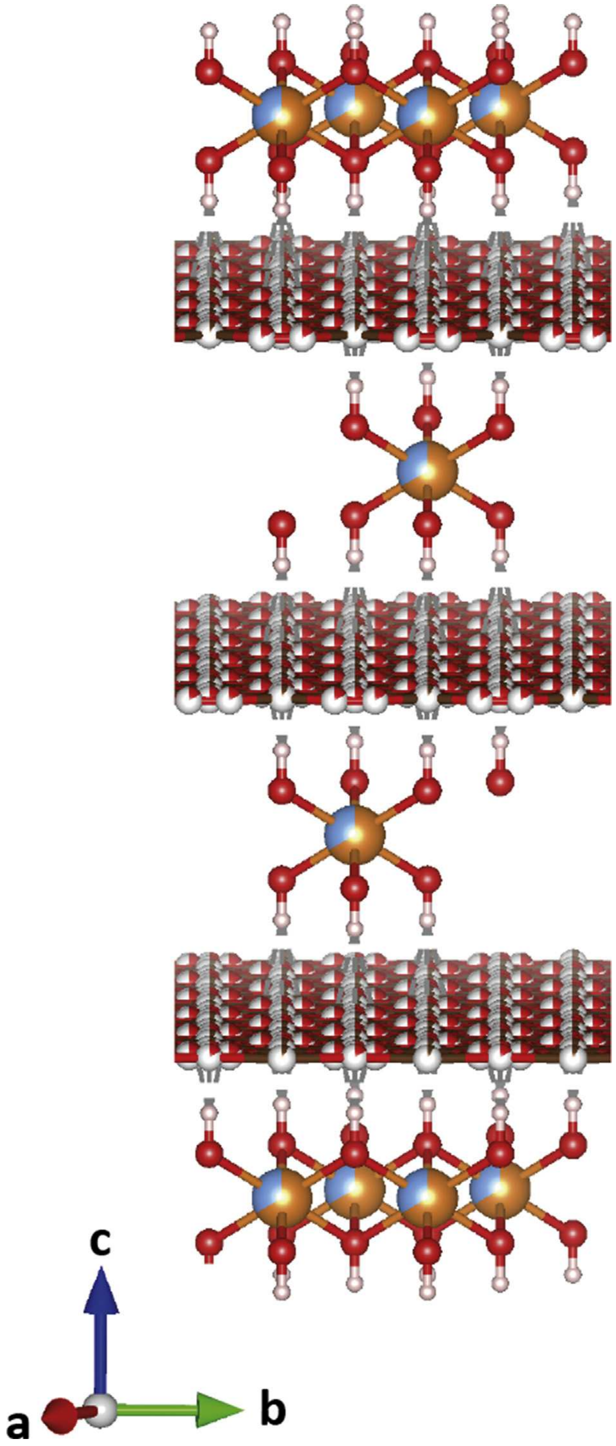

Fig. 26. Illustration of the local environments in the crystal structure of hydrotalcite ($Mg_6Al_2CO_3(OH)_{16}[CO_3]\cdot 4H_2O$) obtained from single-crystal diffraction data [352]. Mg, Al, C, O and H atoms are represented by orange, blue, red and light pink spheres, respectively. Partial colouring of spheres indicates the average proportion of each respective atom occupying a specific site in the hydrotalcite crystal structure. Prepared using the VESTA software package [128].

intercalated and charge balance the net positive charges induced in the sheets by incorporation of trivalent cations to replace Mg^{2+} [341,343]. More than 40 identified mineral species conform to this general description (but with different cation and anion substituents and degrees of substitution) and are collectively denoted hydrotalcite-supergroup phases.

Quintinite-group phases, which are a subset of the hydrotalcite-supergroup with Mg/Al = 2, have been observed on a sub-micrometre scale in hydrated PC-GGBFS blends [99,220,344] and in cements produced from metallurgical slags activated with sodium silicate or sodium hydroxide [71,72,154,190,324,325,345–348], typically occurring when slags with Mg content ≥ 5% are used, consistent with predictions from thermodynamic modelling [349]. These phases generally contain higher Al content (Mg/Al = 2) than true hydrotalcite (Mg/Al = 3) [341]. Previous work identified a phase that was denoted 'M_4AH_{13}' and proposed that it may be an analogue of the AFm-structured C_4AH_{13}, however, this phase has since been shown to be OH-quintinite ($Mg_4Al_2(OH)_{13}\cdot 4H_2O$)) [350,351].

^{27}Al MAS NMR spectra of sodium silicate–activated slag cements exhibit a resonance at $\delta_{obs} = 9$ ppm (9.4 T) attributed to a hydrotalcite-like phase containing Al^{VI} sites [325,353], consistent with ^{27}Al MAS NMR analysis of synthetic hydrotalcites [342,353]. Simulation of ^{27}Al MAS NMR spectra of synthetic hydrotalcite-group phases has determined the isotropic chemical shift of this site to be $\delta_{iso} = 11.8$ ppm, attributed to a single Al environment surrounded by Mg atoms in octahedral coordination [354], with broadening of this resonance indicating increased disorder as Al content is decreased. A broad shoulder on this resonance at $\delta_{obs} = 3$ ppm (8.45 T) is observed when the intercalated anion is CO_3^{2-} [354]. High-field (19.6 T) ^{25}Mg MQMAS NMR of these hydrotalcite-group phases resolved a single ^{25}Mg resonance at $\delta_{iso} = 13.7$ ppm assigned to Mg symmetrically surrounded by 3 Mg and 3 Al ions, $Mg(OAl)_3(OMg)_3$ [354]. ^{1}H MAS NMR data acquired with high spinning speeds have also been used to resolve two distinct hydroxyl resonances in these phases at $\delta_{iso} = 1.3$ and 5.0 ppm, respectively, attributed to Mg_3OH and Mg_2AlOH which are observed at Mg/Al = 4 and 3, respectively [354]. Recently, ^{17}O MAS and MQMAS NMR resonances attributed to oxygen sites in these two hydroxyl groups were also observed in isotopically enriched synthetic hydrotalcite-group phases [355]. ^{1}H-^{13}C CP MAS NMR of synthetic hydrotalcite revealed a single ^{13}C resonance at $\delta_{iso} = 170.9$ ppm attributed to a single CO_3 site [220]. This work also utilised ^{13}C MAS and ^{1}H-^{13}C CP MAS NMR to resolve carbonate anions in anhydrous (e.g $CaCO_3$) and hydrous or hydroxylated (e.g. hydrotalcite or monocarbonate) phases in hydrated PC–limestone blends. The observation of a ^{1}H-^{13}C CP MAS NMR resonance in a hydrated PC–limestone blend exhibiting a chemical shift consistent with that of pure hydrotalcite ($\delta_{iso} = 170.9$ ppm) measured on the same instrument showed explicitly that hydrotalcite formed in this hydrated cement contained carbonate anions [220].

4.2.8.6. Hydrogarnets. The hydrogarnet series ($Ca_3(Al_xFe_{(1-x)})_2(SiO_4)_y(OH)_{4(3-y)}$; $0 \leq x \leq 1$ and $0 \leq y \leq 3$) describes a group of garnet minerals where the $(SiO_4)^{4-}$ tetrahedra are partially or completely replaced by hydroxyl ions. In PC hydrated at ambient temperatures, the formation of siliceous hydrogarnet is minimal [331,356]; however, formation of these phases has been observed in PC hydrated at higher temperatures [357–360] or in the presence of excess Fe species [357,361], and water-rich members of the grossular - katoite hydrogrossular series ($Ca_3Al_2(SiO_4)_y(OH)_{4(3-y)}$; $0 \leq y \leq 3$) are major hydration products in CACs [52].

Katoite ($Ca_3Al_2(SiO_4)_y(OH)_{4(3-y)}$; $0 \leq y \leq 1.5$, often denoted C_3AH_6) exhibits a ^{27}Al MAS NMR resonance with an isotropic chemical shift of $\delta_{iso} = 12.4$ ppm and a quadrupolar coupling constant $C_Q = 0.6$ MHz [52,362] due to octahedral Al surrounded by six hydroxyl groups in the hydrogarnet structure [51]. Increased substitution of silica into this structure results in a ^{27}Al MAS NMR resonance at approximately $\delta_{iso} = 4$–6 ppm, with this resonance shifting towards lower frequencies and exhibiting increased quadrupolar broadening with increasing silica content [50,362]. ^{27}Al MAS NMR resonances attributed to katoite have been observed in CACs [50,52] and alkali-activated slags [20,155,197]. ^{29}Si MAS NMR analysis of hydrated CAC attributed a broad resonance at approximately $\delta_{iso} = -79.9$ ppm to Si sites in $[Si(OAl^{VI})_{4-x}]\ (OCa)_x$ species (classified as Q^0 in the nomenclature of Fig. 1 as there are no bonds to tetrahedral species; all of the Al substituents are octahedral) and used spectral deconvolution to quantify this phase in the hydrated CAC [50].

4.3. Spectral deconvolution

4.3.1. Deconvolution strategies and pitfalls related to spectra of cementitious materials

Mathematical deconvolution of MAS NMR spectra allows resolution of individual resonances which contribute to the overall spectra and can enable quantification of the resonating species [60]. The simplest case in which deconvolution can be performed is for non-quadrupolar (spin $S = ½$) nuclei, the spectra of which can be deconvoluted using a series of Gaussian, Lorentzian or mixed (Voigt or pseudo-Voigt) peaks to simulate individual resonances using a least squares fitting method [363]. This is performed routinely in the study of anhydrous and hydrated cements and related phases.

The most appropriate lineshape to simulate the individual resonances for spin $S = ½$ nuclei depends on the ordering and dynamics of the material under investigation [364,365]; for ordered and rigid SS systems, a Gaussian (statistical) distribution best represents the resonance lineshape as interatomic distances are generally constant. For highly dynamic systems (e.g. solutions or gases), a Lorentzian distribution (based on collision theory) best represents the resonance lineshape as mobility is high [365]. Consequently, resonance lineshapes for spin $S = ½$ nuclei in dynamic SS systems may be best represented by Voigt or pseudo-Voigt distributions weighted heavily towards a Gaussian profile. In reality, dynamics of solids in cementitious systems are extremely slow relative to those in solution, and a Gaussian distribution provides a suitable approximation for the resonance lineshapes.

Deconvolution of the spectra of quadrupolar nuclei ($S > ½$) is also possible; however, quadrupolar interactions must be taken into account when simulating the spectra (Fig. 27). Quadrupolar parameters can be estimated [21]; however, owing to the large variation in NMR parameters across samples and instruments, this approach is prone to error must be appropriately justified. It is often more appropriate to determine the quadrupolar parameters directly.

Quadrupolar interactions can be determined by acquiring single-pulse MAS NMR spectra at multiple fields and simulating the NMR resonances observed for the central transition at each field with a consistent set of NMR parameters (δ_{iso}, C_Q and the asymmetry parameter η) [30,172]; this is often the most readily implementable approach if instruments at multiple fields are available as it does not require complex experiments or fitting approaches. Quadrupolar parameters can also be determined (along with δ_{iso} and η) at a single field by simulation of manifolds of spinning sidebands observed for satellite transitions in MAS NMR spectra [367–369], typically across spectral widths on the order of 2 MHz. This method can be computationally expensive relative to simulation of single-pulse MAS NMR spectra.

Two-dimensional experiments such as MQMAS NMR techniques [242,255,370] are also used to determine δ_{iso}, C_Q and η, and thus aid in deconvolution of NMR spectra for quadrupolar nuclei. MQMAS achieves high resolution by conversion of symmetric MQ coherence (pQ) to the single quantum (1Q) detectable central transition and plotting pQ and 1Q correlations in two dimensions [371]. Consequently, chemical shift anisotropy is removed from the MQ dimension, and δ_{iso} can readily be determined from the two dimensional MQMAS spectrum. C_Q and η can then be determined by simulating the two-dimensional MQMAS spectrum or the pQ dimension of this spectrum using readily available software (e.g. DMFit [60] or Quadfit [372]), information which can in turn be used to simulate the single-pulse MAS NMR spectrum. A suitable model which incorporates these interactions should be used, e.g. the Czjzek model [373].

When performing any spectral deconvolution, the minimum possible number of constituent subpeaks should be used to enable an accurate and meaningful interpretation of the spectra [363]. Subpeak widths should be set in a rational manner, considering the expected disorder within each site type, and their positions must be consistent with literature data for specific site types in pure

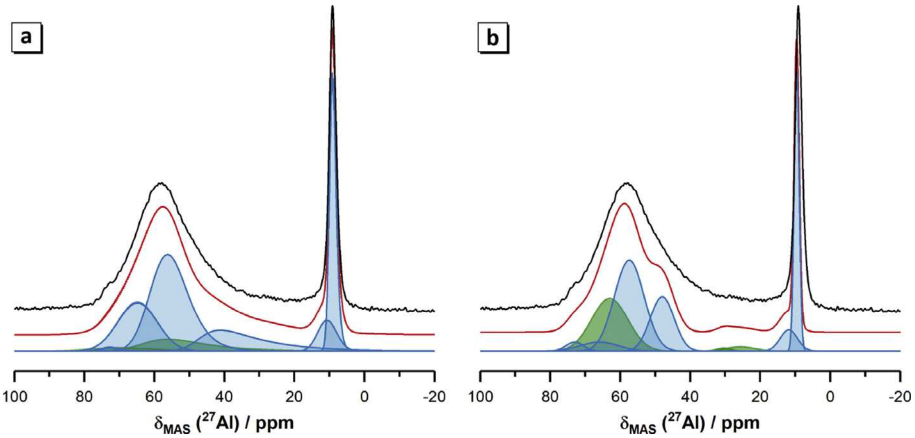

Fig. 27. ^{27}Al ($S = 5/2$) MAS NMR data of a synthetic (calcium, alkali) aluminosilicate gel deconvoluted using (a) the Czjzek isotropic model with quadrupolar parameters determined from ^{27}Al MQMAS NMR data [366] and (b) Gaussian distributions. Deconvoluted resonances (bottom curves) attributed to sites within the precursor are shaded in green, deconvoluted resonances attributed to newly formed sites in the reaction product are marked in blue, the simulated spectrum is marked in red (middle curve) and the ^{27}Al MAS NMR spectrum is marked in black (top curve). The distributions of chemical shifts (as defined by δ_{iso} and FWHM) are the same in the deconvolutions in both (a) and (b); however, the simulated spectrum in (a) correctly accounts for quadrupolar broadening by using the Czjzek isotropic model, while the simulated spectrum in (b) is deconvoluted incorrectly using Gaussian distributions and does not account for quadrupolar broadening. As a result, the intensities of the resonances attributed to each newly formed site differ between (a) and (b), and additional resonances must be added to the deconvolution in (b) to provide a satisfactory fit. Consequently, any quantification obtained from (b) is incorrect. Adapted from Walkley et al., [366].

materials. The relative deconvoluted subpeak intensities should be consistent with a mass balance for all elements, the structural constraints dictated by data from additional analytical techniques (e.g. quantitative XRD) and those described by relevant structural models, e.g. the ‘substituted general model’ for C-S-H gels [159], the ‘crosslinked substituted tobermorite model’ for C-(N)-A-S-H gels [195] and the thermodynamics of a statistical distribution of Si and Al sites within a Q^4 aluminosilicate network for N-A-S-H products [250].

To provide an accurate representation of binder chemistry, and considering that the conversion of solid cementitious phases to hydrate products is almost never fully complete in a practical cementing binder (even after decades or more), the contribution of the remnant unreacted precursor to the spectra must be taken into account [13]. This can be achieved either through selective isotopic labelling of the binder [371], by subtraction of a scaled component spectrum for the remnant unreacted precursor during deconvolution if congruent dissolution is assumed [18,20,345] (Fig. 28) or by using the spectrum of a leached residue (obtained via selective dissolution) to represent a residual precursor component if congruency is uncertain [315,345]. For quantitative analysis, the congruency and kinetics of dissolution and reaction processes involving cementitious precursor materials must be carefully considered and modelled appropriately [14,20] as the underlying assumptions can dramatically affect the final deconvolution. This can be achieved by a variety of methods, including those used to measure the degree of reaction of SCMs in PC—SCM blends [374]. Methods include selective dissolution [375], scanning electron microscopy [323,376], thermogravimetry [374] and XRD with iterative Rietveld refinement (e.g. the ‘partial or no known crystal structure’, PONKCS, method [377]) approaches. In a practical sense, GGBFS is a highly depolymerised glass that is likely to dissolve close to congruently [325], whereas FA is a much more complex mineral assemblage that dissolves incongruently [101,102].

Quantification of individual resonances can often be complex, even with seemingly simple spectra of non-quadrupolar nuclei such as ^{29}Si (see the following section). Quantification of ^{27}Al resonances can be particularly difficult due to the presence of Al species which exhibit resonances so broad that they are often undetectable. ‘NMR invisible’ Al species have been described, largely in older literature, in zeolites, minerals and gels; up to 30% of all Al species in some zeolites could not be observed at 9.4 T [378]. However, these resonances were detectable at high field (18.8 T) [378], highlighting the importance of acquiring SS NMR spectra at the highest field possible if quantification is desired.

4.3.2. *Complexities in quantification of tricalcium and dicalcium silicate in PC*

The ^{29}Si spin—lattice relaxation time constants (T'_1) for belite are approximately 30 times those of alite at the same magnetic field [29], and consequently, it is crucial to ensure that sufficient recycle delays are used during NMR data acquisition to allow for complete relaxation of both alite and belite. This can be achieved via inversion-recovery ^{29}Si spin—lattice relaxation MAS NMR [27,29] (e.g. Fig. 29) or T'_1-relaxation-time-filtered ^{29}Si MAS NMR [57]. Deconvolution of such data allows independent quantification, and hence validation, of the relative proportions of alite and belite within PC [27,29]. This work has shown that the determination of alite and belite content in PC using traditional Bogue calculations [379] strongly overestimates the belite content at the expense of alite, consistent with results from XRD and other techniques; the modified Taylor-Bogue calculation [380] provides a much better match to the alite/belite ratio determined by ^{29}Si MAS NMR spectral deconvolution [27].

4.4. *DFT computation of NMR spectra and parameters*

Isotropic chemical shifts, coupling constants and electric field gradients of molecules can also be predicted *ab initio* from calculations using DFT [381,382] and used to simulate NMR spectra. Computation of NMR parameters from DFT is widely used to determine the crystal structure and ordering in ceramics, zeolites and other crystalline materials; however, there has been little application of this approach to the phases in cementitious materials. Rejmak et al. [165,166] performed simulations of various C-S-H gel structures based on 14 Å tobermorite and jennite models and calculated the resultant isotropic ^{29}Si chemical shifts. Calculated chemical shifts for Q^2 sites were found to be largely independent of the structural model used, and Q^1 and Q^2 sites each showed a large dispersion of calculated chemical shifts. The calculated ^{29}Si MAS NMR chemical shifts were found to be in good agreement with those of 14 Å tobermorite. This work also showed that terminal silicate sites (Q^1), and paired silicate tetrahedra with an AlO_4 unit within the first coordination sphere (Q^2(1Al)), which exhibit similar isotropic chemical shifts, may be distinguished easily by large differences between their chemical shift anisotropies [166].

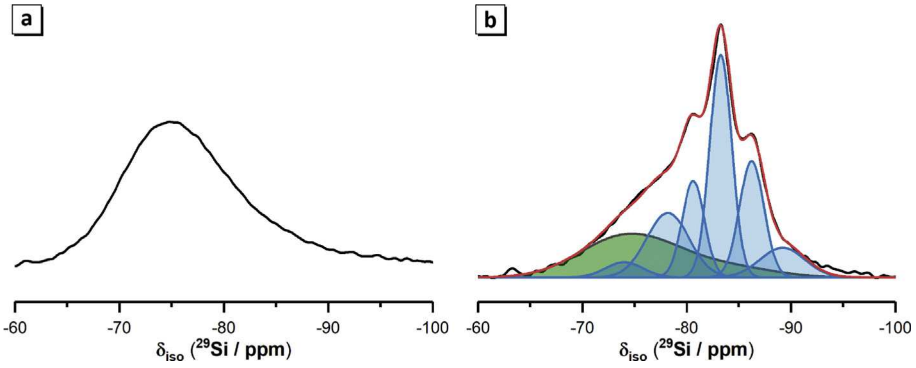

Fig. 28. ^{29}Si MAS NMR spectra (14.1 T, $\nu_R = 10$ kHz) of (a) an anhydrous slag and (b) a sodium silicate—activated slag cement (shown in black) with associated deconvolutions (individual resonances are shown in blue and the simulated spectrum is shown in red). The shaded green resonance is a representation of the unreacted anhydrous slag component and is based on the ^{29}Si MAS NMR spectrum of the anhydrous slag, with the intensity of this resonance rescaled by a single factor on the assumption of congruent dissolution of slag. Adapted from Bernal et al. [20].

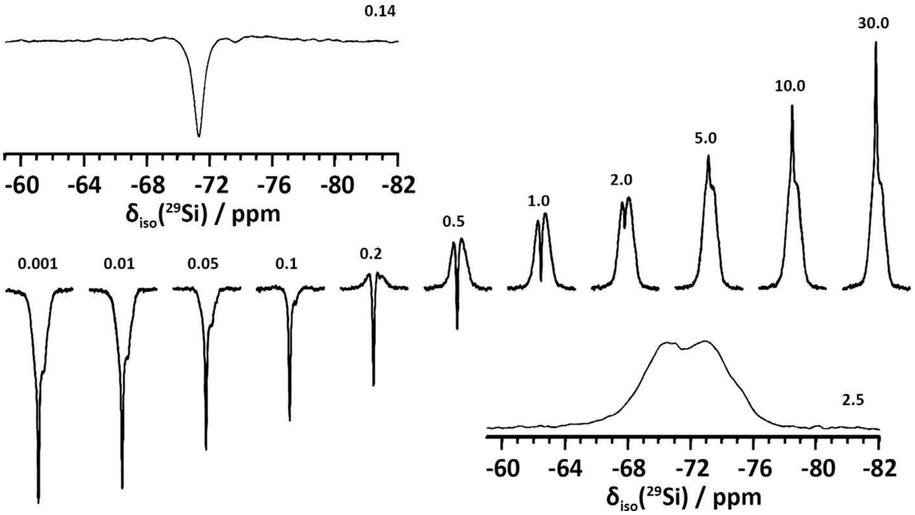

Fig. 29. Inversion-recovery ^{29}Si MAS NMR spectra (9.4 T, $\nu_R = 12.0$ kHz) of white PC, illustrating the differences in spin–lattice relaxation for alite and belite. The left and right expansions show subspectra of belite and alite obtained at the zero-crossings for ^{29}Si in alite and belite, respectively. The recovery times in seconds are indicated for the individual spectra. Adapted from Poulsen et al. [29].

Ab initio prediction of NMR parameters from calculations using DFT is yet to be applied extensively to cementitious materials and represents an important opportunity for further advancement. In particular, combining DFT predictions with experimental data acquired at high field of synthetic model systems will reveal important new structural insights which may then be used to untangle many remaining questions in more complex, heterogeneous systems.

4.5. Application of advanced NMR experiments to cementitious materials

4.5.1. Spin-echo MAS NMR

MAS NMR spectra containing broad resonances, such as those of disordered cementitious systems, can experience artefacts and distortion introduced in the first few microseconds of instrumental dead time at the beginning of the free induction decay [10]. Spin-echo pulse sequences [383] can be used to overcome this by refocussing the spin system. The spin system is given an initial non-selective (90°) pulse, after which the spins are allowed to precess and dephase (due to the varying precession rates of individual nuclear moments within the system). Applying a 180° pulse after a time τ flips the spin system and restores phase coherence to the precession at a time 2τ after the first 90° pulse, refocussing the spin system [10,383]. A small number of authors have used spin-echo pulse sequences analysing cementitious materials to accurately quantify the sites present in these systems [8,260,299,384].

4.5.2. Cross polarisation MAS NMR

CP MAS NMR involves transfer of magnetisation from a nucleus with more abundant spins to a nucleus with less abundant spins, allowing acquisition of the NMR spectrum of the less abundant nucleus with a much higher signal-to-noise ratio than would be obtained by MAS NMR [10]. This is achieved by irradiation of the two nuclei at their correct Larmor frequencies in fulfilment of the Hartmann–Hahn condition [385]. The signal from the less abundant nucleus in closest proximity to the more abundant nucleus is preferentially enhanced, and so additional structural information can be gained by comparison of CP MAS and MAS spectra of the same sample. ^{1}H is the most common high-abundance nucleus in cementitious materials, and consequently, this technique can be particularly advantageous for probing local environments in cementitious materials where the structural role of water is of interest.

4.5.2.1. ^{1}H-X CP MAS. ^{1}H-^{29}Si CP MAS was used to examine hydration of β-C_2S and show that the initial hydration products contain monomeric silicate hydrates, the amount of which determines the initial hydration rate [386], while ^{31}P MAS and ^{31}P-^{1}H CP MAS NMR were used to demonstrate that the very small quantity of PO_4^{3-} ions involved in the hydration of white PC are accommodated within the interlayer of C-S-H [32,34]. Interlayer PO_4^{3-} ions exhibit a broad ^{31}P resonance with the same chemical shift as that of PO_4^{3-} guest ions in alite, so must be selectively detected using ^{31}P-^{1}H CP MAS techniques. ^{1}H-^{29}Si CP MAS NMR (Fig. 30) has also been used to identify Si species closely associated with water (i.e. Si-OH linkages) that are likely to exist as part of the C-S-H gel [43,167,185,386–392], C-(N)-A-S-H gel or AFm phases in alkali-activated slag [154,196], metakaolin [242] and synthetic C-(N)-A-S-H gels [14], while ^{1}H-^{27}Al CP MAS NMR has also been used to identify Al-OH linkages in synthetic analogues of PC hydration products [393].

^{13}C MAS and ^{1}H-^{13}C CP MAS NMR have also been combined to study carbonation of synthetic C-S-H and C-A-S-H gels [221] and to determine the NMR parameters of inorganic carbonates relevant to cement chemistry [220]. During early studies of TAH, ^{1}H-^{27}Al CP MAS NMR revealed $Al(OH)_6^{3-}$ units closely associated with C-S-H, leading to the identification of the TAH as an amorphous aluminate hydroxide or calcium aluminate hydrate produced either as a separate phase or a nanostructured precipitate on the surface of the C-S-H gel [194]. ^{1}H-^{29}Si and ^{1}H-^{27}Al CP MAS NMR experiments are also particularly useful for constraining ^{29}Si and ^{27}Al MAS NMR spectral deconvolutions of the C-S-H model system tobermorite and C-A-S-H gels [14,393].

4.5.2.2. X-Y CP MAS. Studies using X-Y CP MAS NMR experiments (that is, those CP experiments which do not probe protons) to study cementitious materials are fewer; however, they have still revealed new insight into the interactions in these materials. ^{17}O-^{27}Al CP MAS NMR has been used to support a claim that Al atoms within GGBFS are connected only to bridging oxygen atoms and not non-bridging oxygen atoms [75]. ^{19}F-^{29}Si CP MAS and ^{19}F-^{29}Si CP REDOR

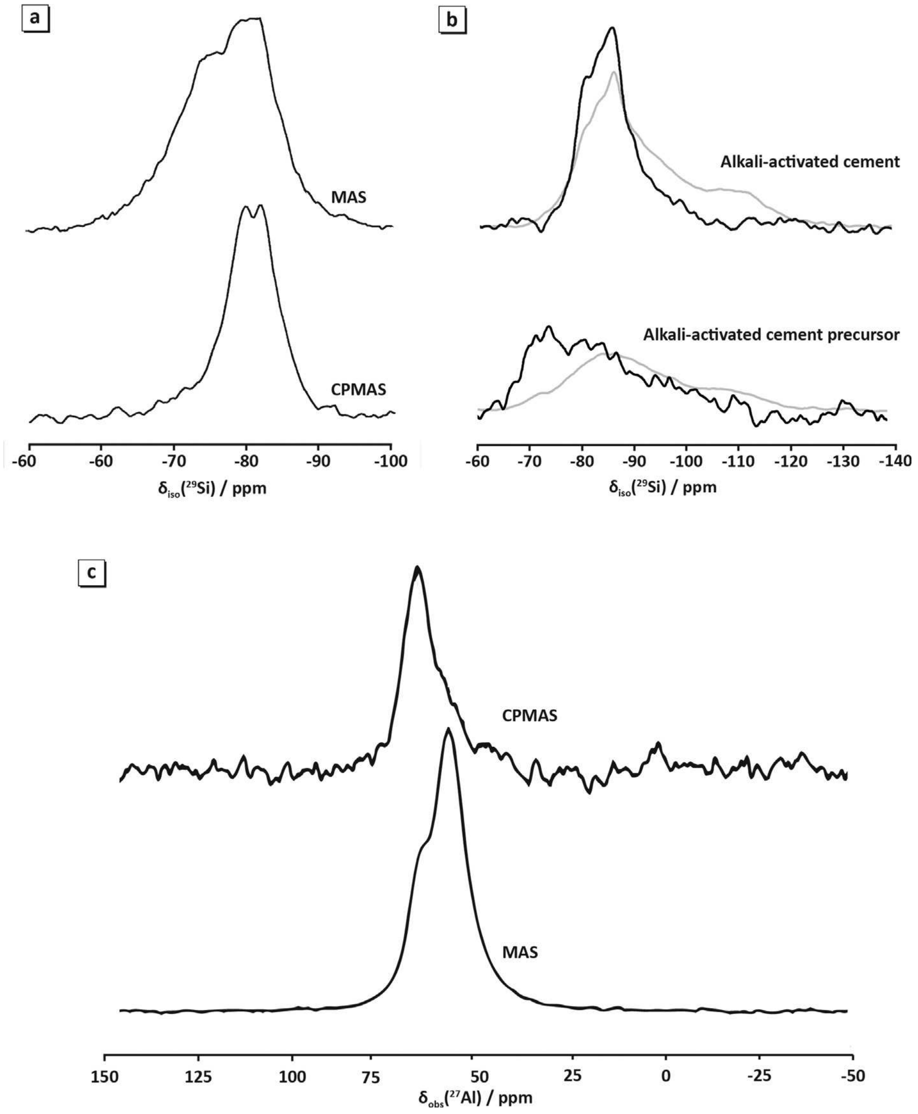

Fig. 30. (a) ^{1}H-^{29}Si CP MAS and MAS NMR spectra of blast furnace slag activated with 4 M NaOH and cured for 1 day. Adapted from Wang et al. [154]. (b) Single-pulse ^{29}Si (grey) and ^{1}H-^{29}Si CP (black) MAS NMR spectra of a synthetic calcium aluminosilicate precursor and of a synthetic alkali-activated cement produced from it (containing C-(N)-A-S-H), cured for 3 days. All spectra are normalised to constant total intensity. Adapted from Walkley et al. [14]. (c) ^{1}H-^{27}Al CP-MAS NMR of tobermorite. Adapted from Houston et al. [393].

MAS NMR techniques have been used to show that F^- substitutes for O^{2-} ions in only the alite phase in white PC, as discussed previously in section 4.1.1.1, aligning with the proposed $Si^{4+} + O^{2-} \rightarrow Al^{3+} + F^-$ coupled substitution mechanism [35], with ^{19}F-^{29}Si CP REDOR MAS NMR indicating a strong preference for F^- substitution into interstitial oxygen sites not involved in covalent Si-O bonds.

4.5.3. Multiple quantum MAS NMR

Recently, MQMAS spectroscopy [394,395], probing half integer quadrupolar nuclei including ^{17}O, ^{23}Na, and ^{27}Al, has been used to obtain high-resolution NMR spectra of synthetic C-S-H [188], CAC [276], AAM [113,242,252,256,276,370,371,396], related reaction products [137,276,354,355,397] and precursors [34,36,75,138]. MQMAS achieves high resolution by conversion of symmetric MQ coherence (*pQ*) to the single quantum (1Q) detectable central transition, and plotting *pQ* and 1Q correlations in two dimensions [371]. Consequently, chemical species with similar local structures and coordination environments, which would otherwise result in overlapping resonances in one-dimensional MAS NMR spectra, may be resolved.

^{27}Al 3Q MAS NMR has been used to examine symmetry of Al sites within synthetic calcium aluminate hydrates and to obtain the isotropic chemical shift, quadrupolar coupling constant and asymmetry parameter of these sites [276]. ^{27}Al 3QMAS NMR spectra of these materials resolved additional Al sites to those that could not be obtained by ^{27}Al MAS NMR alone, including two Al sites within C_4AH_{13} [276]. ^{27}Al 3Q MAS NMR has also been used to probe Al substitution in C-S-H gels [276,393], identifying two distinct tetrahedral Al sites that were attributed to Al substitution for Si into both bridging and non-bridging positions [276], although other studies (as discussed in section 4.2.1.1) have shown that bridging positions are a strongly preferred environment. ^{27}Al 3QMAS NMR has provided additional insight into coordination and symmetry of Al environments within N-A-S-H—type gels (Fig. 31a and b), including determination of the isotropic chemical shift (δ_{iso}), quadrupolar coupling constant (C_Q) and asymmetry (η) parameter of the electric field gradient tensor

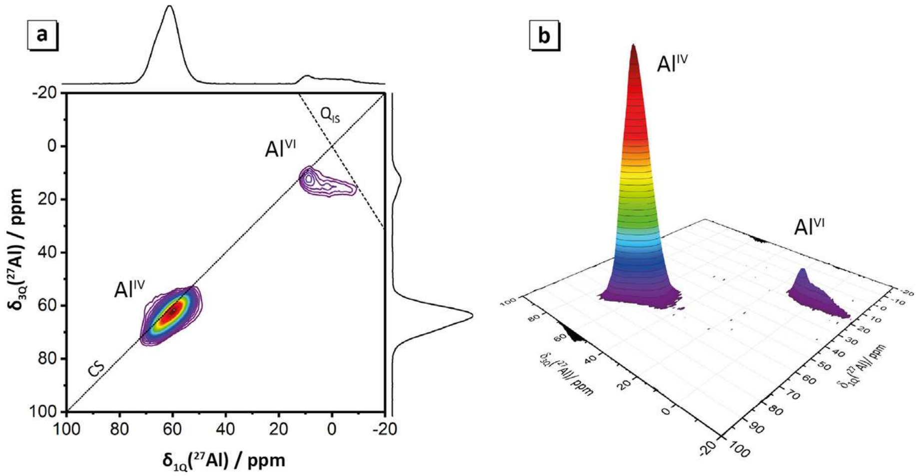

Fig. 31. (a) ^{27}Al MQMAS NMR spectrum (14.1 T, $\nu_R = 20$ kHz, room temperature) of a synthetic alkali-activated cement containing a N-A-S-H gel (adapted from Walkley et al. [255]) and (b) a three-dimensional representation of the spectrum shown in (a).

[113,242,255,256,370,371,396] and also Al environments in C-A-S-H/N-A-S-H gel blends [396]. Both ^{27}Al 3QMAS NMR [276] and ^{25}Mg 3QMAS NMR [354] have also been used to resolve individual Al and Mg sites within Mg-containing LDHs, while recent work used ^{27}Al MQMAS NMR to resolve for the first time 8 distinct Al sites in ye'elimite [34,138] and high-field ^{27}Al MQMAS NMR to resolve for the first time two distinct octahedrally coordinated AlO_6 sites in synthetic ettringite [137] (see section 4.2.8.2 'Aluminate ferrite trisulphate'—type phases). MQMAS NMR, therefore, appears to offer significant scope for future advances in the understanding the atomic structure of cements.

Processing of MQMAS spectra using standard single-axial isotropic shearing (iso-shearing) in the indirect dimension removes the second-order quadrupolar term and leaves the projection of the spectra onto the indirect dimension axis as a pure function of isotropic variables such as the isotropic chemical shift (δ_{iso}) and the quadrupolar-induced shift (δ_{QIS}), allowing chemically distinct sites to be resolved in the indirect (*pQ*) dimension [242,371,398,399]. The more recently introduced method of biaxial Q-shearing [371] in both the indirect and direct dimensions allows orthogonal separation of δ_{iso} from the quadrupolar parameters δ_{QIS} and the quadrupolar coupling constant (C_Q) and is particularly useful for disordered materials which typically give MQMAS spectra displaying a distribution of chemical shift and quadrupolar parameters, that can be difficult to interpret for identification of chemically distinct sites [113,371].

4.5.4. Multiple resonance experiments

4.5.4.1. REDOR, TEDOR, TRAPDOR and REAPDOR. REDOR [400–402] and transferred-echo double-resonance (TEDOR) [403–405] are multiple resonance MAS NMR experiments which exploit heteronuclear dipolar coupling in spin-½ nuclei and provide both qualitative and quantitative information about the proximity of the two spins. Transfer of population in double-resonance (TRAPDOR) [406,407] and rotational-echo adiabatic passage double-resonance (REAPDOR) [400,408] experiments extend the principles of REDOR and TEDOR to quadrupolar nuclei. It should be noted that the X{^{1}H} REDOR and ^{1}H-X CP MAS NMR techniques (where X = ^{27}Al or ^{29}Si) provide complementary data; X{^{1}H} REDOR MAS NMR experiments selectively suppress resonances of protonated species, while ^{1}H-X CP MAS NMR experiments enhance the signals of species experiencing dipolar coupling with rigid proton species (i.e. terminal hydroxyl groups, strongly bound H_2O etc.) [242].

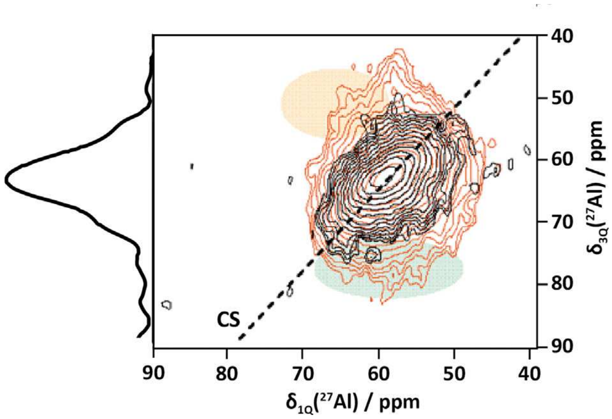

Fig. 32. Isosheared ^{27}Al{^{1}H} REDOR 3Q/MAS NMR spectrum (black contours) overlaid on an isosheared ^{27}Al MQMAS NMR spectrum (red contours) of a sodium silicate-activated metakaolin cement. Adapted from Brus et al. [242]. The main resonance results predominantly from AlO_4^- tetrahedra charge balanced by Na^+ ions, and the shaded orange and green areas indicate regions where AlO_4^- tetrahedra connected to SiO_4 tetrahedra via bridging hydroxyl groups ($Al^{IV} - OH^+ - Si^{IV}$) and AlO_4^- tetrahedra charge balanced by extra-framework Al species are expected to resonate, respectively.

Brus et al. [242] applied ^{27}Al{^{1}H} REDOR 3Q MAS NMR (Fig. 32) to identify bridging hydroxyl groups connecting Al^{IV} and Si^{IV} tetrahedra in a series of alkali-activated metakaolin cements, supporting the identification (see section 4.2.2) of charge balancing extra-framework Al species in these systems. ^{29}Si{^{1}H} REDOR 3Q MAS NMR has also been applied to a series of aluminosilicate geopolymers [370] to show that these materials contain a heterogeneous distribution of charge-balancing Na ions and associated water molecules, with the Na ions and water molecules preferentially clustered around fully polymerised Q^4(4Al) Si species.

Recently, Greiser et al. [409] used ^{29}Si{^{27}Al} TRAPDOR NMR, ^{27}Al{^{29}Si} and ^{27}Al{^{1}H} REDOR NMR experiments to reveal new information regarding the phase assemblage and nanostructure of cementitious sodium aluminosilicate gels produced via the one-part alkali-activation route using variety of silica sources. This work showed the extent of formation of an amorphous sodium

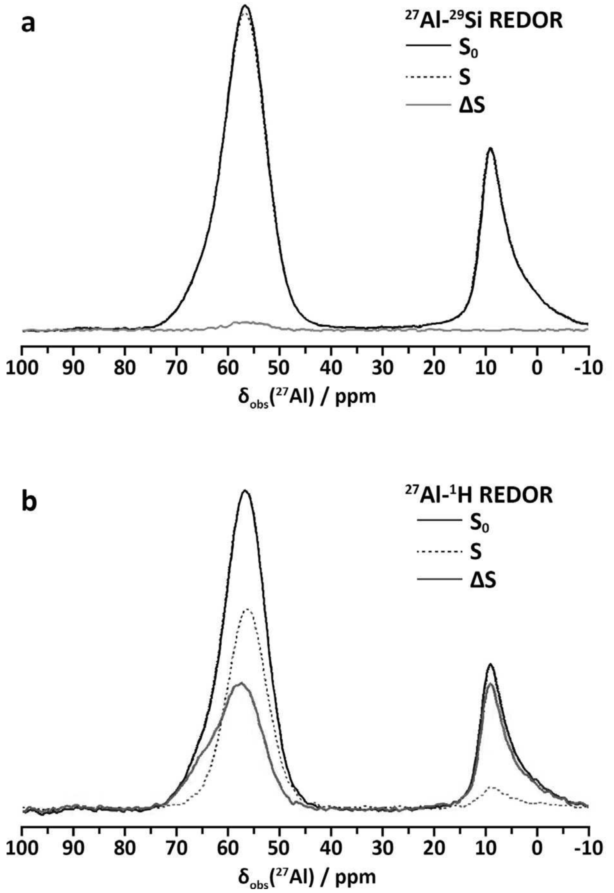

Fig. 33. (a) ^{27}Al{^{29}Si} and (b) ^{27}Al{^{1}H} REDOR NMR spectra (S, dashed line) overlaid with ^{27}Al MAS NMR spectra (S_0, black line) and difference spectra ($\Delta S = S_0 - S$, grey or blue lines) of a cementitious sodium aluminosilicate gel produced via one-part alkali-activation of rice husk ash. Adapted from Greiser et al. [409]. The AlO_6 resonance ($\delta_{obs} = 8$ ppm) does not show a discernible ^{27}Al–(^{29}Si) REDOR NMR effect and shows a strong ^{27}Al–(^{1}H) REDOR interaction, demonstrating that this resonance is due to AlO_6 within a hydrous alumina gel ($Al(OH)_3$) with little or no Si in proximity.

aluminosilicate gel, coprecipitation of an amorphous hydrous alumina gel ($Al(OH)_3$) and formation of zeolitic phases are dependent on the silica source, despite very similar Si/Al of the starting reaction mixtures. The identification of amorphous $Al(OH)_3$ has not been previously reported and demonstrates the importance of using double-resonance NMR techniques to resolve multiple overlapping ^{27}Al resonances that are often present in single-pulse ^{27}Al MAS NMR spectra (Fig. 33).

Tran et al. [396] used a ^{29}Si{^{27}Al} REAPDOR NMR technique to distinguish between Si-$\underline{O}$-Al connectivity environments in alkali-activated metakaolin and to identify the number of Al atoms substituted in the second coordination sphere of each probed Si site. The same authors also used ^{29}Si and ^{27}Al MAS, ^{19}F-^{29}Si CP MAS and ^{29}Si{^{19}F} CP REDOR MAS NMR techniques to show that F^- substitutes for O^{2-} ions in only the alite phase in white PC, with ^{29}Si{^{19}F} CP REDOR MAS NMR indicating a strong preference for F^- substitution into interstitial oxygen sites not involved in covalent Si-O bonds, demonstrating a limitation on the achievable degree of fluoride substitution into alite. ^{31}P-^{27}Al REAPDOR NMR has also been used to demonstrate the existence of aluminium–phosphorus interactions within phosphate-modified CACs [277], where no other analytical technique was able to provide direct evidence about the existence (or otherwise) of these bonds within the disordered gel systems of interest. The universal REAPDOR curve [410] which is commonly used to fit REAPDOR NMR data and determine internuclear distances is, however, specifically designed for an isolated spin pair (i.e. monodentate structures) which limits its applicability (in a quantitative sense) to the polydentate structures which comprise most cements.

4.5.4.2. 2D homonuclear correlation MAS NMR spectroscopy. 2D homonuclear correlation MAS NMR spectroscopy (COSY) is a multiple resonance MAS NMR experiment involving transfer of magnetisation between two nuclei of the same isotope and is useful for determining connectivity between different sites when many resonances are present. Double quantum ^{29}Si-^{29}Si COSY experiments on synthetic C-S-H isotopically enriched with ^{29}Si has resolved both dimeric (Q^1-Q^1) and chain end group (Q^1-Q^2) Si sites as well as (Q^3-Q^3) and (Q^3-Q^2) bridging linkages [176], confirming the presence of these sites in C-S-H as discussed in section 4.2.1.

4.5.4.3. 2D heteronuclear correlation MAS NMR. 2D HETCOR MAS NMR is a multiple resonance MAS NMR experiment which involves transfer of magnetisation between two heteronuclei and is useful for determining connectivity between different nuclei when many resonances are present. This experiment is similar to the X-Y CP MAS NMR experiment; however, in the X-Y 2D HETCOR experiment, the magnetisation of nucleus Y is allowed to evolve for a (variable) time t_1 prior to being transferred to nucleus X, whose response is measured directly during the detection period t_2 [10]. Significant sensitivity enhancement can be gained by combining MQMAS with the HETCOR experiment (HMQC) [411]. Rawal et al. [57] used ^{1}H-^{29}Si and ^{1}H-^{27}Al HETCOR MAS NMR with different ^{1}H spin-diffusion times to probe correlations between different molecular moieties in hydrated white PC: both short (10 μs, probing strongly coupled species with internuclear distance < 1 nm) and long (30 ms for ^{29}Si and 20 ms for ^{27}Al, probing more weakly coupled species over several nm), Fig. 33. ^{1}H-^{29}Si HETCOR MAS NMR experiments were able to resolve chemically bonded -OH groups, adsorbed water and strongly hydrogen bonded -OH groups associated with Q^1, Q^2 and Q^2(1Al) Si sites, with chemically bonded -OH groups and adsorbed water primarily associated with Q^1 and Q^2(1Al) sites, as well as water strongly adsorbed to six-coordinate Si sites within a thaumasite-like phase that was claimed to be present in the hydrated PC [57], although the identification of this mineral in cements that have not been subjected to chemical damage is extremely uncommon.

Resonances from protons in H_2O, Ca-OH and Si-OH groups have also been identified by ^{1}H-^{29}Si HETCOR MAS NMR analysis of synthetic C-S-H [176], with both types of hydroxyl sites correlating with all Si sites in C-S-H and water molecules correlating with Q^1 and both bridging and pairing Q^2 sites. ^{1}H-^{27}Al HETCOR MAS NMR experiments resolved hydroxyl groups chemically bound to Al^{VI} sites within ettringite and TAH and an absence of correlation between ^{1}H species and four-coordinate $^{27}Al^{IV}$ moieties. Enhanced resolution provided by the ^{1}H-^{29}Si and ^{1}H-^{27}Al HETCOR MAS NMR experiments allowed resolution of ^{29}Si-OH and ^{27}Al-OH bonds which were not resolved in single-pulse MAS NMR experiments.

4.5.4.4. Satellite transition spectroscopy. Accurate determination of δ_{iso}, C_Q and η is crucial for an accurate and unambiguous interpretation of SS MAS NMR spectra. Determination of these parameters from single-pulse MAS NMR spectroscopy observing the central transition ($m_S = \pm$ ½) between nuclear spin states, however, is hindered due to the second-order quadrupolar shift. Satellite transition spectroscopy involves observing the satellite transitions in MAS NMR spectra of quadrupolar nuclei, where residual second-order quadrupolar effects under MAS (quadrupolar broadening and the second-order quadrupolar shift) are reduced relative to the central transition [367]. The dependence of the second-order quadrupolar shift for a particular spin S on the nuclear spin state transition (m) results in a different net isotropic chemical shift for each m; consequently, by simulating all observed transitions, it is possible to determine the isotropic chemical shift from a single spectrum [367–369]. Jakobsen et al. [412] and Skibsted et al. [368] demonstrated simulation of all transitions in MAS NMR spectra of crystalline powders to accurately determine C_Q and η for ^{17}O, ^{23}Na and ^{27}Al in systems with large C_Q values (C_Q > 2 MHz), as well as applying this method to accurately determine the ^{27}Al C_Q value of 1.9 MHz for Al^{VI} in hydrated white PC [44]. Skibsted et al. [52] also applied this method to a series of calcium aluminate phases in CAC and in PC (Fig. 34), determining ^{27}Al δ_{iso}, C_Q and η values and distributions. These were then used to describe linear relationships between C_Q and the mean deviation of bond angle from ideal tetrahedral symmetry, as well as between C_Q and a calculated estimate of the geometrical dependency of the EFG tensor. This method has also been used to identify the two crystallographically distinct octahedrally coordinated Al sites in kaolinite [413], as specified by its crystal structure [414].

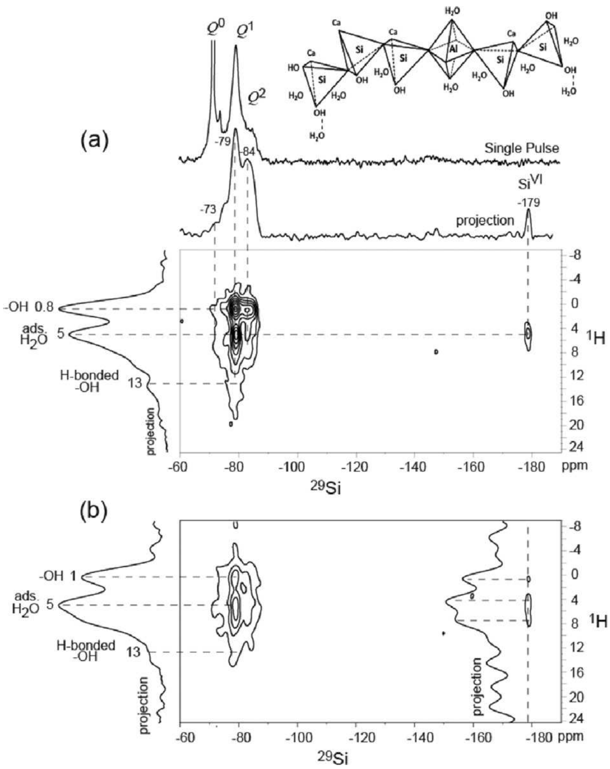

Fig. 34. ^{1}H-^{29}Si HETCOR MAS NMR (11.7 T, $\nu_R = 6.5$ kHz) of white PC with ^{1}H spin-diffusion times of (a) 10 μs and (b) 30 ms. Adapted from Rawal et al. [57].

4.5.5. ^{1}H relaxation NMR

^{1}H is the most sensitive nucleus in cementitious materials which may be probed using NMR; however, ^{1}H-^{1}H dipolar couplings cause severe line broadening which limits the resolution of ^{1}H MAS NMR spectra, which is further compounded by the small chemical shift range (approximately 20 ppm) over which ^{1}H nuclei in solid phases resonate. These limitations have impeded the widespread application of single-pulse MAS NMR experiments probing ^{1}H in cementitious materials. However, ^{1}H relaxation rates (spin–lattice, $1/T_1$, and spin–spin, $1/T_2$) are sensitive to proton mobility in hydration products and water in the vicinity of solid–liquid interfaces and can therefore provide extensive information regarding porosity, pore size distributions and tortuosity in these cementitious materials.

Early work used proton NMR relaxometry to monitor hydration of C_3S and PC by measurement of T_1 and T_2 relaxation times [415–421], identifying an induction period (~3 h) [417] as well as water in various hydrate phases [416], mobile water in micropores and water with restricted mobility in a solid gel component [420,421].

Spin–spin relaxation rates are modulated by the motion of the species on which the spins reside and vary by several orders of magnitude for protons in rigid (e.g. solid hydrates) or mobile (e.g. molecular water) species. Rapid measurements of spin–spin relaxation rates are, therefore, particularly attractive to monitor reaction in-situ [22]. This approach has been used to monitor hydration of white PC, and synthetic C_3S and C_3A [422–424], and led to identification of five components with distinct T_2 values corresponding to capillary pore water, solid-like crystalline water and OH^- groups (i.e. in portlandite, gypsum, and ettringite), mobile water molecules incorporated in C–S–H, water molecules with restricted mobility in the C–S–H interlayer and secondary hydration water released by the decomposition of ettringite (Fig. 35).

Spin–spin relaxation times have also been used to observe the retardation of PC hydration in the presence of various organic additives [425]. ^{1}H relaxation rates can also be exploited to link the structure and kinetics at the atomic level of cementitious materials to microscale and macroscale engineering properties such as porosity, pore size distributions and tortuosity in hydrated cement pastes, mortars and concretes. Measurement of spin–lattice relaxation rates has been used to develop relaxation models for the dependency of T_1 on the pore surface to the volume ratio and the presence of nearby paramagnetic ions [426–429], while T_1-T_2 [427,428] and T_2-T_2 [430,431] correlation NMR experiments have been used to identify discrete pores (e.g. large capillary pores or smaller gel pores, Fig. 36) in hydrated white PC and synthetic C-S-H and measure exchange of water between these locations, by exploitation of the fact that increased pore size results in increased relaxation times. Variable temperature proton NMR relaxometry experiments have also been used to monitor freeze–thaw phenomena in hydrated PC and C-S-H [432,433].

More recently, ^{1}H NMR relaxometry has been used to quantify all the water present, as well as the size and volume of discrete population of pores containing this water, in hydrated white PC both with [8] and without [434,435] silica fume additions. This work showed that addition of silica fume alters the chemical composition of the C-S-H formed, but does not alter the density, and identified four discrete populations of liquid water: water in the C-S-H interlayer in pores approximately 1 nm in diameter, water in the C-S-H gel in pores approximately 3 nm in diameter and water in small (~10 nm in diameter) and large (≫ 10 nm in diameter) capillary pores. Correlation of ^{1}H NMR relaxometry with results from mercury intrusion porosimetry (MIP) has shown that MIP can accurately determine the porosity of cement pastes [436].

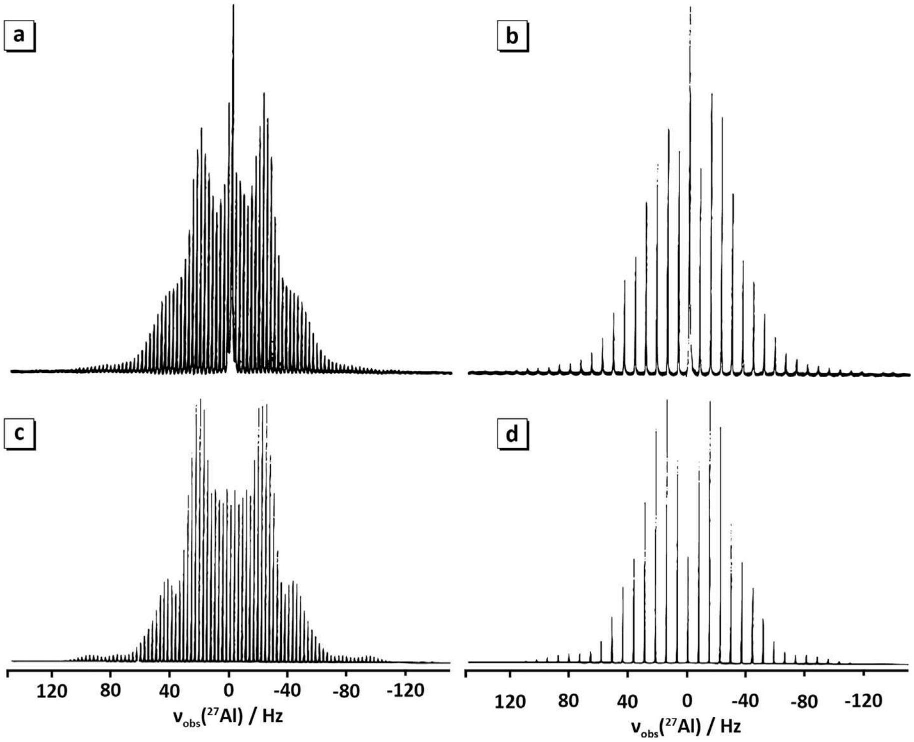

Fig. 35. ^{27}Al MAS NMR spectra of ettringite ($C_6A\$_3H_{32}$) recorded at (a) 9.4 T, $\nu_R = 6.5$ kHz, and (b) 9.4 T, ν_R 7.5 kHz. Simulations of the satellite transitions in parts (a) and (b) are shown in (c) and (d). Adapted from Skibsted et al. [52].

5. Conclusions and perspectives

SS NMR spectroscopy has played a pivotal role understanding the complex composition–structure–property relationships in cements and related materials. In particular, SS NMR spectroscopy has afforded a level of insight into their atomic structure, reaction mechanisms, kinetics of formation and structural evolution which has been previously unattainable and has provided the basis for the current state of the art in understanding, modelling and predicting composition–structure–property relationships, reaction mechanism and kinetics in PC, CAC, CSA, magnesia-based, AAM and geopolymer-based cements.

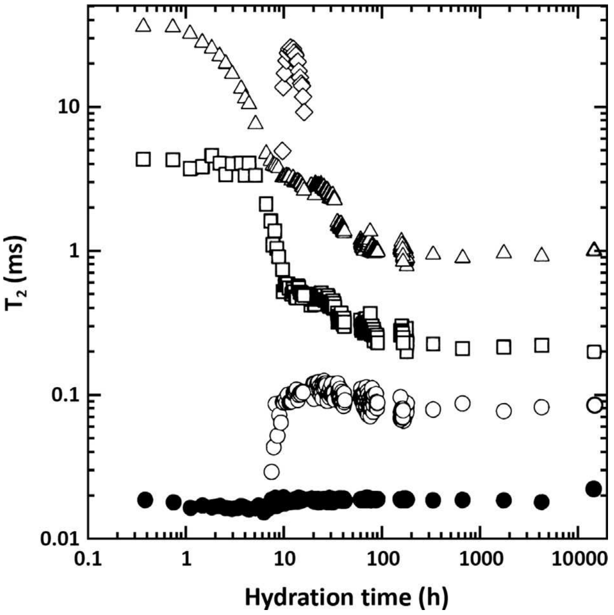

Fig. 36. Proton spin–spin relaxation times (T_2) vs. hydration time of white PC hydrated at 20 °C. Proton signals come from water molecules in the pore solution (triangles), crystalline water and OH^- groups (filled circles) in C-S-H and portlandite, more mobile water molecules in the interlayer of C-S-H (squares) and secondary hydration water released by the decomposition of ettringite (diamonds). Adapted from Holly et al. [422].

Application of advanced MAS NMR experiments probing ^1H, ^{13}C, ^{17}O, ^{19}F, ^{23}Na, ^{25}Mg, ^{27}Al, ^{29}Si, ^{31}P, ^{33}S, ^{35}Cl, ^{39}K and ^{43}Ca nuclei have been used to study the atomic structure, phase evolution, nanostructural development, reaction mechanisms and kinetics occurring in these cementitious systems, including multidimensional, multiresonance and in-situ experiments. Single-pulse MAS NMR experiments probing ^{27}Al and ^{29}Si nuclei are by far the most routinely applied NMR experiments used to study cements and have been instrumental in building our current understanding. However, owing to the extensive structural information these experiments have provided to date, their role in continued advancement of the understanding of composition–structure–property relationships in cementitious materials is limited.

Performing NMR experiments at high field ($B_0 \geq 20.0$ T), probing less commonly investigated nuclei such as ^{17}O and ^{43}Ca in isotopically enriched samples and application of less commonly used techniques including CP MAS, MQMAS and multiresonance experiments (e.g. SEDOR, REDOR, TEDOR, REAPDOR and TRAPDOR) presents the best opportunity for elucidation of information regarding the mechanisms which control the structure and physical properties of cementitious materials, that has been previously unattainable. The difficulty in conducting these experiments and interpretation of the spectra obtained, however, is likely to be the largest obstacle to their routine application. This presents a key challenge which must be overcome and will require a concerted, collaborative effort from both the SS NMR spectroscopy and cement materials chemistry communities.

Conflict of interest

The authors declare no conflict of interest.

Acknowledgements

The authors thank and acknowledge Dr John Hanna, Dr Greg Rees, Dr Frédéric Blanc, Dr Marc-Antoine Sani, Dr Peter Duxson, Dr John Gehman, Dr Susan Bernal and Dr Rupert Myers for very helpful and insightful discussions over many years regarding the application of SS NMR to cementitious materials. The research leading to these results has received funding from the Engineering and Physical Sciences Research Council (EP/P013171/1) and from the European Research Council under the European Union's Seventh Framework Programme (FP/2007-2013)/ERC Grant Agreement StG 335928 (GeopolyConc).

Appendix A. Supplementary data

Supplementary data to this article can be found online at https://doi.org/10.1016/j.mtadv.2019.100007.

References

[1] P.-C. Aïtcin, Cements of yesterday and today: concrete of tomorrow, Cement Concr. Res. 30 (2000) 1349–1359.
[2] World Business Council for Sustainable Development, Cement Industry Energy and CO_2 Performance: 'Getting the Numbers Right', 2009.
[3] P. Hewlett, Lea's Chemistry of Cement and Concrete, Elsevier Science, 1998.
[4] J.L. Provis, S.A. Bernal, Geopolymers and related alkali-activated materials, Annu. Rev. Mater. Res. 44 (2014) 299–327.
[5] L. Bernstein, J. Roy, K.C. Delhotal, J. Harnisch, R. Matsuhashi, L. Price, et al., Industry, in: B. Metz, O.R. Davidson, P.R. Bosch, R. Dave, L.A. Meyer (Eds.), Climate Change 2007: Mitigation. Contribution of Working Group III to the Fourth Assessment Report of the Intergovernmental Panel on Climate Change, Cambridge University Press, Cambridge, United Kingdom, 2007.
[6] J.G.J. Olivier, G. Janssens-Maenhout, J.A.H.W. Peters, Trends in Global CO_2 Emissions; 2012 Report, PBL Netherlands Environmental Assessment Agency, The Hague, Netherlands, 2012.
[7] B. Lothenbach, K. Scrivener, R.D. Hooton, Supplementary cementitious materials, Cement Concr. Res. 41 (2011) 1244–1256.
[8] A.C.A. Muller, K.L. Scrivener, J. Skibsted, A.M. Gajewicz, P.J. McDonald, Influence of silica fume on the microstructure of cement pastes: new insights from ^{1}H NMR relaxometry, Cement Concr. Res. 74 (2015) 116–125.
[9] A.M. Gajewicz, E. Gartner, K. Kang, P.J. McDonald, V. Yermakou, A ^{1}H NMR relaxometry investigation of gel-pore drying shrinkage in cement pastes, Cement Concr. Res. 86 (2016) 12–19.
[10] K.J.D. Mackenzie, M.E. Smith, Multinuclear Solid-State Nuclear Magnetic Resonance of Inorganic Materials, Pergamon, Elsevier, Oxford, 2002.
[11] G. Engelhardt, D. Michel, High-resolution Solid State NMR of Silicates and Zeolites, Wiley, Chichester, 1987.
[12] S.E. Ashbrook, Recent advances in solid-state NMR spectroscopy of quadrupolar nuclei, Phys. Chem. Chem. Phys. 11 (2009) 6892–6905.
[13] J.L. Provis, A. Palomo, C.J. Shi, Advances in understanding alkali-activated materials, Cement Concr. Res. 78 (2015) 110–125.
[14] B. Walkley, R. San Nicolas, M.-A. Sani, G.J. Rees, J.V. Hanna, J.S.J. van Deventer, et al., Phase evolution of C-(N)-A-S-H/N-A-S-H gel blends investigated via alkali-activation of synthetic calcium aluminosilicate precursors, Cement Concr. Res. 89 (2016) 120–135.
[15] É.M. L'Hôpital, B. Lothenbach, G. Le Saoût, D. Kulik, K. Scrivener, Incorporation of aluminium in calcium-silicate-hydrates, Cement Concr. Res. 75 (2015) 91–103.
[16] J. Skibsted, M.D. Andersen, H. Jennings, The effect of alkali ions on the incorporation of aluminum in the calcium silicate hydrate (C-S-H) phase resulting from portland cement hydration studied by ^{29}Si MAS NMR, J. Am. Ceram. Soc. 96 (2013) 651–656.
[17] I.G. Richardson, The calcium silicate hydrates, Cement Concr. Res. 38 (2008) 137–158.
[18] G. Le Saoût, M. Ben Haha, F. Winnefeld, B. Lothenbach, C. Jantzen, Hydration degree of alkali-activated slags: a ^{29}Si NMR study, J. Am. Ceram. Soc. 94 (2011) 4541–4547.
[19] W. Loewenstein, The distribution of aluminum in the tetrahedra of silicates and aluminates, Am. Mineral. 39 (1954) 92–96.
[20] S.A. Bernal, J.L. Provis, B. Walkley, R. San Nicolas, J.D. Gehman, D.G. Brice, et al., Gel nanostructure in alkali-activated binders based on slag and fly ash, and effects of accelerated carbonation, Cement Concr. Res. 53 (2013) 127–144.
[21] R.J. Myers, S.A. Bernal, J.D. Gehman, J.S.J. van Deventer, J.L. Provis, The role of Al in cross-linking of alkali-activated slag cements, J. Am. Ceram. Soc. 98 (2015) 996–1004.
[22] J. Skibsted, C. Hall, Characterization of cement minerals, cements and their reaction products at the atomic and nano scale, Cement Concr. Res. 38 (2008) 205–225.
[23] H.F.W. Taylor, Cement Chemistry, Thomas Telford, London, 1997.
[24] J.W. Jeffery, The tricalcium silicate phase, in: Proceedings of the Third International Symposium on the Chemistry of Cement, Cement and Concrete Association, London, 1952.
[25] T. Staněk, P. Sulovský, The influence of the alite polymorphism on the strength of the Portland cement, Cement Concr. Res. 32 (2002) 1169–1175.
[26] M. Magi, E. Lippmaa, A. Samoson, G. Engelhardt, A.R. Grimmer, Solid-state high-resolution silicon-29 chemical shifts in silicates, J. Phys. Chem. 88 (1984) 1518–1522.
[27] J. Skibsted, H.J. Jakobsen, C. Hall, Quantification of calcium silicate phases in Portland cements by ^{29}Si MAS NMR spectroscopy, J. Chem. Soc. Faraday Trans. 91 (1995) 4423–4430.
[28] F. Nishi, Y. Takéuchi, I. Maki, Tricalcium silicate $Ca_3O[SiO_4]$: the monoclinic superstructure, Z. für Kristallogr. Cryst. Mater. 172 (1985) 297–314.
[29] S.L. Poulsen, V. Kocaba, G. Le Saoût, H.J. Jakobsen, K.L. Scrivener, J. Skibsted, Improved quantification of alite and belite in anhydrous Portland cements by ^{29}Si MAS NMR: effects of paramagnetic ions, Solid State Nucl. Magn. Reson. 36 (2009) 32–44.
[30] J. Skibsted, H.J. Jakobsen, C. Hall, Direct observation of aluminium guest ions in the silicate phases of cement minerals by ^{27}Al MAS NMR spectroscopy, J. Chem. Soc. Faraday Trans. 90 (1994) 2095–2098.
[31] T.T. Tran, D. Herfort, H.J. Jakobsen, J. Skibsted, Site preferences of fluoride guest ions in the calcium silicate phases of Portland cement from $^{29}Si\{^{19}F\}$ CP-REDOR NMR spectroscopy, J. Am. Chem. Soc. 131 (2009) 14170–14171.
[32] S.L. Poulsen, H.J. Jakobsen, J. Skibsted, Incorporation of phosphorus guest ions in the calcium silicate phases of Portland cement from ^{31}P MAS NMR spectroscopy, Inorg. Chem. 49 (2010) 5522–5529.
[33] J. Jeffery, The crystal structure of tricalcium silicate, Acta Crystallogr. 5 (1952) 26–35.
[34] J. Skibsted, T.F. Sevelsted, S.L. Poulsen, T.T. Tran, Studies on guest-ion incorporation in Portland cement - part 2, ZKG Int. (2013) 46–52.
[35] G.K. Moir, H.F.W. Taylor, F. Massazza, J.E. Bailey, S. Chanda, P. Pichat, et al., Improvements in the early strength properties of Portland cement [and discussion], Philos. Trans. Roy. Soc. Lond. A Math. Phys. Sci. 310 (1983) 127–138.
[36] J. Skibsted, T.F. Sevelsted, S.L. Poulsen, T.T. Tran, Studies on guest-ion incorporation in Portland cement—Part 1, ZKG Int. (2013) 66–72.
[37] I. Hung, Z. Gan, P.L. Gor'kov, D.C. Kaseman, S. Sen, M. LaComb, et al., Detection of "free" oxide ions in low-silica Ca/Mg silicate glasses: results from $^{17}O \rightarrow ^{29}Si$ HETCOR NMR, J. Non Cryst. Solids 445–446 (2016) 1–6.
[38] I.L. Moudrakovski, R. Alizadeh, J.J. Beaudoin, Natural abundance high field ^{43}Ca solid state NMR in cement science, Phys. Chem. Chem. Phys. 12 (2010) 6961–6969.
[39] N.I. Golovastikov, R.G. Matveeva, N.V. Belov, Crystal structure of tricalcium silicate, Kristallografiya 20 (1975) 721–729.
[40] R. Dupree, A.P. Howes, S.C. Kohn, Natural abundance solid state ^{43}Ca NMR, Chem. Phys. Lett. 276 (1997) 399–404.
[41] D.L. Bryce, Calcium binding environments probed by ^{43}Ca NMR spectroscopy, Dalton Trans. 39 (2010) 8593–8602.
[42] K.H. Jost, B. Ziemer, R. Seydel, Redetermination of the structure of β-dicalcium silicate, Acta Crystallogr. B 33 (1977) 1696–1700.
[43] X. Cong, R.J. Kirkpatrick, ^{17}O and ^{29}Si MAS NMR study of $\beta-C_2S$ hydration and the structure of calcium-silicate hydrates, Cement Concr. Res. 23 (1993) 1065–1077.
[44] J. Hjorth, J. Skibsted, H.J. Jakobsen, ^{29}Si MAS NMR studies of Portland cement components and effects of microsilica on the hydration reaction, Cement Concr. Res. 18 (1988) 789–798.
[45] K.T. Greene, Dicalcium silicate solid solutions, J. Res. Natl. Bur. Stand. 32 (1944) 1–10.
[46] R.W. Nurse, The dicalcium silicate phase, in: Proceedings of the Third International Symposium on the Chemistry of Cement, Cement and Concrete Association, London, 1952.
[47] E.H. Oelkers, S.R. Gislason, The mechanism, rates and consequences of basaltic glass dissolution: I. An experimental study of the dissolution rates of basaltic glass as a function of aqueous Al, Si and oxalic acid concentration at $25^{\circ}C$ and $pH = 3$ and 11, Geochem. Cosmochim. Acta 65 (2001) 3671–3681.
[48] R.J. Mccarty, J.F. Stebbins, Constraints on aluminum and scandium substitution mechanisms in forsterite, periclase, and larnite: high-resolution NMR, Am. Mineral. 102 (2017) 1244–1253.
[49] J. Skibsted, H. Bildsøe, H.J. Jakobsen, High-speed spinning versus high magnetic field in MAS NMR of quadrupolar nuclei. ^{27}Al MAS NMR of $3CaO \cdot Al_2O_3$, J. Magn. Reson. 92 (1991) 669–676.
[50] P. Pena, J.M. Rivas Mercury, A.H. de Aza, X. Turrillas, I. Sobrados, J. Sanz, Solid-state ^{27}Al and ^{29}Si NMR characterization of hydrates formed in

calcium aluminate–silica fume mixtures, J. Solid State Chem. 181 (2008) 1744–1752.

[51] D. Müller, W. Gessner, A. Samoson, E. Lippmaa, G. Scheler, Solid-state ^{27}Al NMR studies on polycrystalline aluminates of the system CaO-Al_2O_3, Polyhedron 5 (1986) 779–785.

[52] J. Skibsted, E. Henderson, H.J. Jakobsen, Characterization of calcium aluminate phases in cements by ^{27}Al MAS NMR spectroscopy, Inorg. Chem. 32 (1993) 1013–1027.

[53] S. Geller, P.M. Raccah, Phase transitions in perovskitelike compounds of the rare earths, Phys. Rev. B 2 (1970) 1167–1172.

[54] P. Colombet, H. Zanni, A.-R. Grimmer, P. Sozzani, Nuclear Magnetic Resonance Spectroscopy of Cement-Based Materials, Springer, Berlin, Heidelberg, 1998.

[55] J. Skibsted, H.J. Jakobsen, C. Hall, Quantitative aspects of ^{27}Al MAS NMR of calcium aluminoferrites, Adv. Cem. Based Mater. 7 (1998) 57–59.

[56] C.L. Edwards, L.B. Alemany, A.R. Barron, Solid-state ^{29}Si NMR analysis of cements: comparing different methods of relaxation analysis for determining spin–lattice relaxation times to enable determination of the C_3S/C_2S ratio, Ind. Eng. Chem. Res. 46 (2007) 5122–5130.

[57] A. Rawal, B.J. Smith, G.L. Athens, C.L. Edwards, L. Roberts, V. Gupta, et al., Molecular silicate and aluminate species in anhydrous and hydrated cements, J. Am. Chem. Soc. 132 (2010) 7321–7337.

[58] G.E. Pake, Nuclear resonance absorption in hydrated crystals: fine structure of the proton line, J. Chem. Phys. 16 (1948) 327–336.

[59] J.-B. d'Espinose de Lacaillerie, F. Barberon, B. Bresson, P. Fonollosa, H. Zanni, V.E. Fedorov, et al., Applicability of natural abundance ^{33}S solid-state NMR to cement chemistry, Cement Concr. Res. 36 (2006) 1781–1783.

[60] D. Massiot, F. Fayon, M. Capron, I. King, S. Le Calvé, B. Alonso, et al., Modelling one- and two-dimensional solid-state NMR spectra, Magn. Reson. Chem. 40 (2002) 70–76.

[61] K.L. Scrivener, V.M. John, E.M. Gartner, Eco-efficient Cements: Potential, Economically Viable Solutions for a low-CO_2, Cement-Based Materials Industry, United Nations Environment Programme, Paris, 2016.

[62] D.W.S. Ho, R.K. Lewis, Carbonation of concrete and its prediction, Cement Concr. Res. 17 (1987) 489–504.

[63] J. Feng, Y.J. Lee, R.J. Reeder, B.L. Phillips, Observation of bicarbonate in calcite by NMR spectroscopy, Am. Mineral. 91 (2006) 957–960.

[64] H.W. Papenguth, R.J. Kirkpatrick, B. Montez, P.A. Sandberg, ^{13}C MAS NMR spectroscopy of inorganic and biogenic carbonates, Am. Mineral. 74 (1989) 1152–1158.

[65] H. Nebel, M. Neumann, C. Mayer, M. Epple, On the structure of amorphous calcium carbonate – a detailed study by solid-state NMR spectroscopy, Inorg. Chem. 47 (2008) 7874–7879.

[66] European Committee for Standardization, EN 197-1:2011, Cement. Composition, Specifications and Conformity Criteria for Common Cements, 2011.

[67] P. Duxson, J.L. Provis, Designing precursors for geopolymer cements, J. Am. Ceram. Soc. 91 (2008) 3864–3869.

[68] J.L. Provis, J.S.J. van Deventer, Geopolymers – Structure, Processing, Properties and Industrial Applications, Woodhead Publishing, Abingdon, 2009.

[69] C.J. Shi, P.V. Krivenko, D.M. Roy, Alkali Activated Cements and Concretes, Taylor and Francis, New York, 2006.

[70] Y. Li, X. Liu, H. Sun, D. Cang, Mechanism of phase separation in BFS (blast furnace slag) glass phase, Sci. China Technol. Sci. 54 (2011) 105–109.

[71] M. Ben Haha, B. Lothenbach, G. Le Saoût, F. Winnefeld, Influence of slag chemistry on the hydration of alkali-activated blast-furnace slag — part I: effect of MgO, Cement Concr. Res. 41 (2011) 955–963.

[72] S.A. Bernal, R. San Nicolas, R.J. Myers, R. Mejía de Gutiérrez, F. Puertas, J.S.J. van Deventer, et al., MgO content of slag controls phase evolution and structural changes induced by accelerated carbonation in alkali-activated binders, Cement Concr. Res. 57 (2014) 33–43.

[73] M. Ben Haha, B. Lothenbach, G. Le Saoût, F. Winnefeld, Influence of slag chemistry on the hydration of alkali-activated blast-furnace slag — part II: effect of Al_2O_3, Cement Concr. Res. 42 (2012) 74–83.

[74] P.J. Schilling, L.G. Butler, A. Roy, H.C. Eaton, ^{29}Si and ^{27}Al MAS-NMR of NaOH-activated blast-furnace slag, J. Am. Ceram. Soc. 77 (1994) 2363–2368.

[75] K. Shimoda, Y. Tobu, K. Kanehashi, T. Nemoto, K. Saito, Total understanding of the local structures of an amorphous slag: perspective from multi-nuclear (^{29}Si, ^{27}Al, ^{17}O, ^{25}Mg, and ^{43}Ca) solid-state NMR, J. Non Cryst. Solids 354 (2008) 1036–1043.

[76] K. Shimoda, K. Kanehashi, M. Hatakeyama, Y. Tobu, T. Shimizu, K. Saito, Ultra-high magnetic field (21.8 T) solid-state nuclear magnetic resonance for inorganic materials, Chem. Lett. 36 (2007) 834–835.

[77] K. Shimoda, Y. Tobu, K. Kanehashi, T. Nemoto, K. Saito, Local environments of slags: the first application of ^{43}Ca 3QMAS NMR technique, Chem. Lett. 34 (2005) 1588–1589.

[78] K. Shimoda, Y. Tobu, K. Kanehashi, T. Nemoto, K. Saito, First evidence of multiple Ca sites in amorphous slag structure: multiple-quantum MAS NMR spectroscopy on calcium-43 at high magnetic field, Solid State Nucl. Magn. Reson. 30 (2006) 198–202.

[79] K. Shimoda, K. Saito, Detailed structure elucidation of the blast furnace slag by molecular dynamics simulation, ISIJ Int. 47 (2007) 1275–1279.

[80] S.K. Lee, J.F. Stebbins, Disorder and the extent of polymerization in calcium silicate and aluminosilicate glasses: O-17 NMR results and quantum chemical molecular orbital calculations, Geochem. Cosmochim. Acta 70 (2006) 4275–4286.

[81] S.K. Lee, J.F. Stebbins, C.A. Weiss, R.J. Kirkpatrick, ^{17}O and ^{27}Al MAS and 3QMAS NMR study of synthetic and natural layer silicates, Chem. Mater. 15 (2003) 2605–2613.

[82] J.R. Allwardt, S.K. Lee, J.F. Stebbins, Bonding preferences of non-bridging O atoms: evidence from ^{17}O MAS and 3QMAS NMR on calcium aluminate and low-silica Ca-aluminosilicate glasses, Am. Mineral. 88 (2003) 949–954.

[83] S.K. Lee, J.F. Stebbins, Extent of intermixing among framework units in silicate glasses and melts, Geochem. Cosmochim. Acta 66 (2002) 303–309.

[84] J.F. Stebbins, J.V. Oglesby, S. Kroeker, Oxygen triclusters in crystalline $CaAl_4O_7$ (grossite) and in calcium aluminosilicate glasses: ^{17}O NMR, Am. Mineral. 86 (2001) 1307–1311.

[85] S.K. Lee, J.F. Stebbins, The structure of aluminosilicate glasses: high-resolution ^{17}O and ^{27}Al MAS and 3QMAS NMR study, J. Phys. Chem. B 104 (2000) 4091–4100.

[86] S.K. Lee, J.F. Stebbins, Al–O–Al and Si–O–Si sites in framework aluminosilicate glasses with Si/Al=1: quantification of framework disorder, J. Non Cryst. Solids 270 (2000) 260–264.

[87] W. Bumrongjaroen, I. Muller, R.A. Livingston, J. Davis, A performance-based fly ash classification system using glassy particle chemical composition data, World of Coal Ash Conference, Denver, Colorado, USA, 2011.

[88] S. Gomes, M. François, Characterization of mullite in silicoaluminous fly ash by XRD, TEM, and ^{29}Si MAS NMR, Cement Concr. Res. 30 (2000) 175–181.

[89] S. Gomes, M. François, M. Abdelmoula, P. Refait, C. Pellissier, O. Evrard, Characterization of magnetite in silico-aluminous fly ash by SEM, TEM, XRD, magnetic susceptibility, and Mössbauer spectroscopy, Cement Concr. Res. 29 (1999) 1705–1711.

[90] N. Koukouzas, J. Hämäläinen, D. Papanikolaou, A. Tourunen, T. Jäntti, Mineralogical and elemental composition of fly ash from pilot scale fluidised bed combustion of lignite, bituminous coal, wood chips and their blends, Fuel 86 (2007) 2186–2193.

[91] K. Erdoğdu, P. Türker, Effects of fly ash particle size on strength of Portland cement fly ash mortars, Cement Concr. Res. 28 (1998) 1217–1222.

[92] S.V. Vassilev, R. Menendez, D. Alvarez, M. Diaz-Somoano, M.R. Martinez-Tarazona, Phase-mineral and chemical composition of coal fly ashes as a basis for their multicomponent utilization. 1. Characterization of feed coals and fly ashes, Fuel 82 (2003) 1793–1811.

[93] R.T. Hemmings, E.E. Berry, On the glass in coal fly ashes: recent advances, in: GJ McCarthy, FP Glasser, DM Roy, RT Hemmings (Eds.), Materials research society symposia proceedings, vol 113, Cambridge University Press, New York, USA, 1987, pp. 3–38.

[94] S. Diamond, Particle morphologies in fly ash, Cement Concr. Res. 16 (1986) 569–579.

[95] I. Diaz-Loya, M. Juenger, S. Seraj, R. Minkara, Extending supplementary cementitious material resources: reclaimed and remediated fly ash and natural pozzolans, Cement Concr. Compos. 101 (2019) 44–51.

[96] E.I. Diaz, E.N. Allouche, S. Eklund, Factors affecting the suitability of fly ash as source material for geopolymers, Fuel 89 (2010) 992–996.

[97] K.L. Aughenbaugh, R.T. Chancey, P. Stutzman, M.C. Juenger, D.W. Fowler, An examination of the reactivity of fly ash in cementitious pore solutions, Mater. Struct. 46 (2013) 869–880.

[98] K.L. Aughenbaugh, P. Stutzman, M.C. Juenger, Assessment of the glassy phase reactivity in fly ashes used for geopolymer cements, in: L. Struble, J. Hicks (Eds.), Geopolymer Binder Systems, ASTM STP 1566, ASTM International, West Conshohocken, PA, 2013, pp. 11–20.

[99] P.T. Durdziński, M. Ben Haha, M. Zajac, K.L. Scrivener, Phase assemblage of composite cements, Cement Concr. Res. 99 (2017) 172–182.

[100] P.T. Durdziński, C.F. Dunant, M. Ban Haha, K.L. Scrivener, A new quantification method based on SEM-EDS to assess fly ash composition and study the reaction of its individual components in hydrating cement paste, Cement Concr. Res. 73 (2015) 111–122.

[101] P.T. Durdziński, R. Snellings, C.F. Dunant, M.B. Haha, K.L. Scrivener, Fly ash as an assemblage of model Ca–Mg–Na-aluminosilicate glasses, Cement Concr. Res. 78 (2015) 263–272.

[102] R.T. Chancey, P. Stutzman, M.C.G. Juenger, D.W. Fowler, Comprehensive phase characterization of crystalline and amorphous phases of a Class F fly ash, Cement Concr. Res. 40 (2010) 146–156.

[103] A. Fernández-Jiménez, A. Palomo, Characterisation of fly ashes. Potential reactivity as alkaline cements, Fuel 82 (2003) 2259–2265.

[104] C. Ruiz-Santaquiteria, J. Skibsted, A. Fernández-Jiménez, A. Palomo, Alkaline solution/binder ratio as a determining factor in the alkaline activation of aluminosilicates, Cement Concr. Res. 42 (2012) 1242–1251.

[105] A. Palomo, S. Alonso, A. Fernández-Jiménez, I. Sobrados, J. Sanz, Alkaline activation of fly ashes: NMR study of the reaction products, J. Am. Ceram. Soc. 87 (2004) 1141–1145.

[106] J.F. Stebbins, Z. Xu, NMR evidence for excess non-bridging oxygen in an aluminosilicate glass, Nature 390 (1997) 60–62.

[107] K.J.D. MacKenzie, I.W.M. Brown, R.H. Meinhold, M.E. Bowden, Outstanding problems in the kaolinite-mullite reaction sequence investigated by ^{29}Si and ^{27}Al solid-state nuclear magnetic resonance: I, Metakaolinite, J. Am. Ceram. Soc. 68 (1985) 293–297.

[108] C.E. White, J.L. Provis, T. Proffen, D.P. Riley, van Deventer JSJ, Density functional modeling of the local structure of kaolinite subjected to thermal dehydroxylation, J. Phys. Chem. A 114 (2010) 4988–4996.

[109] F. Wang, K. Kovler, J.L. Provis, A. Buchwald, M. Cyr, C. Patapy, et al., Metakaolin, in: N. De Belie, M. Soutsos, E. Gruyaert (Eds.), Properties of Fresh and

Hardened Concrete Containing Supplementary Cementitious Materials: State-of-the-Art Report of the RILEM Technical Committee 238-SCM, Working Group 4, Springer International, Cham, 2018, pp. 153–179.

[110] D. Koloušek, J. Brus, M. Urbanova, J. Andertova, V. Hulinsky, J. Vorel, Preparation, structure and hydrothermal stability of alternative (sodium silicate-free) geopolymers, J. Mater. Sci. 42 (2007) 9267–9275.

[111] P. Duxson, G.C. Lukey, F. Separovic, J.S.J. van Deventer, Effect of alkali cations on aluminum incorporation in geopolymeric gels, Ind. Eng. Chem. Res. 44 (2005) 832–839.

[112] P. Duxson, J.L. Provis, G.C. Lukey, F. Separovic, J.S.J. van Deventer, ^{29}Si NMR study of structural ordering in aluminosilicate geopolymer gels, Langmuir 21 (2005) 3028–3036.

[113] L. Kobera, J. Brus, P. Klein, J. Dedecek, M. Urbanova, Biaxial Q-shearing of ^{27}Al 3QMAS NMR spectra: insight into the structural disorder of framework aluminosilicates, Solid State Nucl. Magn. Reson. 57–58 (2014) 29–38.

[114] P. Duxson, A. Fernández-Jiménez, J.L. Provis, G.C. Lukey, A. Palomo, J.S.J. van Deventer, Geopolymer technology: the current state of the art, J. Mater. Sci. 42 (2007) 2917–2933.

[115] J. Davidovits, Geopolymers – inorganic polymeric new materials, J. Therm. Anal. 37 (1991) 1633–1656.

[116] C.E. White, J.L. Provis, T. Proffen, D.P. Riley, J.S.J. van Deventer, Combining density functional theory (DFT) and pair distribution function (PDF) analysis to solve the structure of metastable materials: the case of metakaolin, Phys. Chem. Chem. Phys. 12 (2010) 3239–3245.

[117] Z. Dai, T.T. Tran, J. Skibsted, Aluminum incorporation in the C–S–H phase of white Portland cement–metakaolin blends studied by ^{27}Al and ^{29}Si MAS NMR spectroscopy, J. Am. Ceram. Soc. 97 (2014) 2662–2671.

[118] R.C. Lewis, Silica fume, in: N. De Belie, M. Soutsos, E. Gruyaert (Eds.), Properties of Fresh and Hardened Concrete Containing Supplementary Cementitious Materials: State-of-the-Art Report of the RILEM Technical Committee 238-SCM, Working Group 4, Springer International, Cham, 2018, pp. 99–121.

[119] H. Hilbig, F.H. Köhler, P. Schießl, Quantitative ^{29}Si MAS NMR spectroscopy of cement and silica fume containing paramagnetic impurities, Cement Concr. Res. 36 (2006) 326–329.

[120] X.J. Wang, X.Y. Wang, H.F. Zhu, C. Qian, ^{29}Si NMR characterization of silica tetrahedron in the silica fume simulate hydration, Key Eng. Mater. 539 (2013) 1–4.

[121] K.L. Scrivener, B. Lothenbach, N. De Belie, E. Gruyaert, J. Skibsted, R. Snellings, et al., TC 238-SCM: hydration and microstructure of concrete with SCMs, Mater. Struct. 48 (2015) 835–862.

[122] K. Scrivener, Calcium aluminate cements, in: B.S. Choo (Ed.), Advanced Concrete Technology, Butterworth-Heinemann, Oxford, 2003, pp. 1–31.

[123] A. Neville, History of high-alumina cement. Part 1: problems and the stone report, Proc. Instit. Civil Eng. Eng. Hist. Herit. 162 (2009) 81–91.

[124] W. Hörkner, H. Müller-Buschbaum, Zur kristallstruktur von $CaAl_2O_4$, J. Inorg. Nucl. Chem. 38 (1976) 983–984.

[125] J.F. Stebbins, S.K. Lee, J.V. Oglesby, Al-O-Al oxygen sites in crystalline aluminates and aluminosilicate glasses: high-resolution oxygen-17 NMR results, Am. Mineral. 84 (1999) 983.

[126] V.I. Ponomarev, D.M. Kheiker, N.V. Belov, Crystal structure of calcium dialuminate, Kristallografija 15 (1970) 1140.

[127] D.W. Goodwin, A.J. Lindop, The crystal structure of $CaO\cdot 2Al_2O_3$, Acta Crystallogr. B 26 (1970) 1230–1235.

[128] K. Momma, F. Izumi, VESTA 3 for three-dimensional visualization of crystal, volumetric and morphology data, J. Appl. Crystallogr. 44 (2011) 1272–1276.

[129] H. Bartl, T. Scheller, Zur struktur des $12CaO\cdot 7Al_2O_3$, Neues Jahrbuch Mineral. Monatsh. (1970) 547–552.

[130] M. Teusner, R.A. De Souza, H. Krause, S.G. Ebbinghaus, B. Belghoul, M. Martin, Oxygen diffusion in mayenite, J. Phys. Chem. C 119 (2015) 9721–9727.

[131] M. Lacerda, J.T.S. Irvine, F.P. Glasser, A.R. West, High oxide ion conductivity in $Ca_{12}Al_{14}O_{33}$, Nature 332 (1988) 525.

[132] F. Winnefeld, B. Lothenbach, Hydration of calcium sulfoaluminate cements — experimental findings and thermodynamic modelling, Cement Concr. Res. 40 (2010) 1239–1247.

[133] G. Le Saoût, B. Lothenbach, A. Hori, T. Higuchi, F. Winnefeld, Hydration of Portland cement with additions of calcium sulfoaluminates, Cement Concr. Res. 43 (2013) 81–94.

[134] J.T. Song, J.F. Young, Direct synthesis and hydration of calcium aluminosulfate ($Ca_4Al_6O_{16}S$), J. Am. Ceram. Soc. 85 (2002) 535–539.

[135] S. Allevi, M. Marchi, F. Scotti, S. Bertini, C. Cosentino, Hydration of calcium sulphoaluminate clinker with additions of different calcium sulphate sources, Mater. Struct. 49 (2016) 453–466.

[136] N.J. Calos, C.H.L. Kennard, A.K. Whittaker, R.L. Davis, Structure of calcium aluminate sulfate $Ca_4Al_6O_{16}S$, J. Solid State Chem. 119 (1995) 1–7.

[137] J. Skibsted, M.T. Pedersen, J. Holzinger, Resolution of the two aluminum sites in ettringite by ^{27}Al MAS and MQMAS NMR at very high magnetic field (22.3 T), J. Phys. Chem. C 121 (2017) 4011–4017.

[138] M.T. Pedersen, J. Skibsted, ^{27}Al MAS and MQMAS NMR study of ye'elimite at different magnetic fields, in: Proceedings of EUROMAR. Aarhus, Denmark, 2016.

[139] L. Bonafous, C. Bessada, D. Massiot, J.-P. Coutures, B.L. Holland, P. Colombet, ^{29}Si MAS NMR study of dicalcium silicate: the structural influence of sulfate and alumina stabilizers, J. Am. Ceram. Soc. 78 (1995) 2603–2608.

[140] P. Brotherton, J. Epstein, M. Pryce, A. White, Crystal structure of ‘calcium sulphosilicate’, $Ca_5(SiO_4)_2SO_4$, Aust. J. Chem. 27 (1974) 657–660.

[141] S.A. Walling, J.L. Provis, Magnesia-based cements: a journey of 150 years, and cements for the future? Chem. Rev. 116 (2016) 4170–4204.

[142] S.A. Walling, H. Kinoshita, S.A. Bernal, N.C. Collier, J.L. Provis, Structure and properties of binder gels formed in the system $Mg(OH)_2$–SiO_2–H_2O for immobilisation of Magnox sludge, Dalton Trans. 44 (2015) 8126–8137.

[143] D.C. Menashi, B. Arnon, Durability of Portland cement-silica fume pastes in magnesium and sodium sulfate solutions, ACI Mater. J. 85 (1988) 148–157.

[144] J. Szczerba, R. Prorok, E. Śnieżek, D. Madej, K. Maślona, Influence of time and temperature on ageing and phases synthesis in the MgO–SiO_2–H_2O system, Thermochim. Acta 567 (2013) 57–64.

[145] J. Wei, Y. Chen, Y. Li, The reaction mechanism between MgO and microsilica at room temperature, J. Wuhan Univ. Technol. Mater. Sci. Ed. 21 (2006) 88–91.

[146] J. Wei, Q. Yu, W. Zhang, H. Zhang, Reaction products of MgO and microsilica cementitious materials at different temperatures, J. Wuhan Univ. Technol. Mater. Sci. Ed. 26 (2011) 745–748.

[147] C. Ødegård, Z. Chen, B. Myhre, MgO–SiO_2–H_2O bonded MgO castables, in: Unified International Technical Conference on Refractories (UNITECR'01), American Ceramic Society, 2001, pp. 4–7.

[148] B. Myhre, C. Ødegård, H. Feldborg, Periclase castables based on the bond MgO–SiO_2–H_2O: properties and current status, in: INREFCON (5th India International Refractories Congress) in Bhubaneswar, India, 2002.

[149] R. Dupree, M. Smith, Solid-state magnesium-25 NMR spectroscopy, J. Chem. Soc. Chem. Commun. (1988) 1483–1485.

[150] P.S. Fiske, J.F. Stebbins, I. Farnan, Bonding and dynamical phenomena in MgO: a high temperature ^{17}O and ^{25}Mg NMR study, Phys. Chem. Miner. 20 (1994) 587–593.

[151] A.V. Chadwick, I.J.F. Poplett, D.T.S. Maitland, M.E. Smith, Oxygen speciation in nanophase MgO from solid-state ^{17}O NMR, Chem. Mater. 10 (1998) 864–870.

[152] S. Rossano, F. Mauri, C.J. Pickard, I. Farnan, First-principles calculation of ^{17}O and ^{25}Mg NMR shieldings in MgO at finite temperature: rovibrational effect in solids, J. Phys. Chem. B 109 (2005) 7245–7250.

[153] K.J.D. MacKenzie, R.H. Meinhold, Thermal decomposition of brucite, $Mg(OH)_2$: a ^{25}Mg MAS NMR study, Thermochim. Acta 230 (1993) 339–343.

[154] S.-D. Wang, K.L. Scrivener, ^{29}Si and ^{27}Al NMR study of alkali-activated slag, Cement Concr. Res. 33 (2003) 769–774.

[155] F. Bonk, J. Schneider, M.A. Cincotto, H. Panepucci, Characterization by multinuclear high-resolution NMR of hydration products in activated blast-furnace slag pastes, J. Am. Ceram. Soc. 86 (2003) 1712–1719.

[156] P. Colombet, A.R. Grimmer, Applications of NMR Spectroscopy to Cement Science, Taylor & Francis, 1995.

[157] J. Skibsted, C. Hall, H.J. Jakobsen, Nuclear magnetic resonance spectroscopy and magnetic resonance imaging of cements and cement-based materials, in: J. Bensted, P. Barnes (Eds.), Structure and Performance of Cements, second ed., Spon Press, London & New York, 2002, pp. 457–476.

[158] C. Labbez, I. Pochard, B. Jönsson, A. Nonat, C-S-H/solution interface: experimental and Monte Carlo studies, Cement Concr. Res. 41 (2011) 161–168.

[159] I.G. Richardson, G.W. Groves, The incorporation of minor and trace elements into calcium silicate hydrates (C-S-H) gel in hardened cement pastes, Cement Concr. Res. 23 (1993) 131–138.

[160] I.G. Richardson, Tobermorite/jennite- and tobermorite/calcium hydroxide-based models for the structure of C-S-H: applicability to hardened pastes of tricalcium silicate, β-dicalcium silicate, Portland cement, and blends of Portland cement with blast-furnace slag, metakaolin, or silica fume, Cement Concr. Res. 34 (2004) 1733–1777.

[161] D.A. Kulik, Improving the structural consistency of C-S-H solid solution thermodynamic models, Cement Concr. Res. 41 (2011) 477–495.

[162] H.F.W. Taylor, Proposed structure for calcium silicate hydrate gel, J. Am. Ceram. Soc. 69 (1986) 464–467.

[163] A. Nonat, The structure and stoichiometry of C-S-H, Cement Concr. Res. 34 (2004) 1521–1528.

[164] G. Renaudin, J. Russias, F. Leroux, C. Cau-dit-Coumes, F. Frizon, Structural characterization of C–S–H and C–A–S–H samples—part II: local environment investigated by spectroscopic analyses, J. Solid State Chem. 182 (2009) 3320–3329.

[165] P. Rejmak, J.S. Dolado, M.J. Stott, A. Ayuela, ^{29}Si NMR in cement: a theoretical study on calcium silicate hydrates, J. Phys. Chem. C 116 (2012) 9755–9761.

[166] P. Rejmak, J.S. Dolado, M.J. Stott, A. Ayuela, ^{29}Si chemical shift anisotropies in hydrated calcium silicates: a computational study, J. Phys. Chem. C 117 (2013) 8374–8380.

[167] X. Cong, R.J. Kirkpatrick, ^{29}Si MAS NMR study of the structure of C-S-H, Adv. Cem. Based Mater. 3 (1996) 114–156.

[168] X. Cong, R.J. Kirkpatrick, ^{17}O MAS NMR investigation of the structure of calcium silicate hydrate gel, J. Am. Ceram. Soc. 79 (1996) 1585–1592.

[169] C.S. Walker, S. Sutou, C. Oda, M. Mihara, A. Honda, Calcium silicate hydrate (C-S-H) gel solubility data and a discrete solid phase model at 25°C based on two binary non-ideal solid solutions, Cement Concr. Res. 79 (2016) 1–30.

[170] A. Kumar, B.J. Walder, A. Kunhi Mohamed, A. Hofstetter, B. Srinivasan, A.J. Rossini, et al., The atomic-level structure of cementitious calcium silicate hydrate, J. Phys. Chem. C 121 (2017) 17188–17196.

[171] I.G. Richardson, Model structures for C-(A)-S-H(I), Acta Crystallogr. B 70 (2014) 903–923.

[172] M.D. Andersen, H.J. Jakobsen, J. Skibsted, Incorporation of aluminum in the calcium silicate hydrate (C–S–H) of hydrated Portland cements: A high-field ^{27}Al and ^{29}Si MAS NMR investigation, Inorg. Chem. 42 (2003) 2280–2287.

[173] H. Viallis, P. Faucon, J.C. Petit, A. Nonat, Interaction between salts (NaCl, CsCl) and calcium silicate hydrates (C–S–H), J. Phys. Chem. B 103 (1999) 5212–5219.

[174] J.J. Chen, J.J. Thomas, H.F.W. Taylor, H.M. Jennings, Solubility and structure of calcium silicate hydrate, Cement Concr. Res. 34 (2004) 1499–1519.

[175] I.G. Richardson, J. Skibsted, L. Black, R.J. Kirkpatrick, Characterisation of cement hydrate phases by TEM, NMR and Raman spectroscopy, Adv. Cem. Res. 22 (2010) 233–248.

[176] F. Brunet, P. Bertani, T. Charpentier, A. Nonat, J. Virlet, Application of ^{29}Si homonuclear and ^{1}H–^{29}Si heteronuclear NMR correlation to structural studies of calcium silicate hydrates, J. Phys. Chem. B 108 (2004) 15494–15502.

[177] B. Lothenbach, A. Nonat, Calcium silicate hydrates: solid and liquid phase composition, Cement Concr. Res. 78 (2015) 57–70.

[178] K.J.D. MacKenzie, M.E. Smith, A. Wong, A multinuclear MAS NMR study of calcium-containing aluminosilicate inorganic polymers, J. Mater. Chem. 17 (2007) 5090–5096.

[179] G.M. Bowers, R.J. Kirkpatrick, Natural abundance ^{43}Ca NMR spectroscopy of tobermorite and jennite: model compounds for C–S–H, J. Am. Ceram. Soc. 92 (2009) 545–548.

[180] B. Bresson, S. Masse, H. Zanni, C. Noik, Tricalcium silicate hydration at high temperature. A ^{29}Si and ^{1}H NMR Investigation, in: P. Colombet, H. Zanni, A.-R. Grimmer, P. Sozzani (Eds.), Nuclear Magnetic Resonance Spectroscopy of Cement-Based Materials, Springer Berlin Heidelberg, 1998, pp. 209–215.

[181] D. Heidemann, W. Wieker, Characterization of protons in C-S-H phases by means of high-speed ^{1}H MAS NMR investigations, in: P. Colombet, A.-R. Grimmer, H. Zanni, P. Sozzani (Eds.), Nuclear Magnetic Resonance Spectroscopy of Cement-Based Materials, Springer-Verlag, Berlin, 1998, pp. 169–180.

[182] D. Heidemann, Proton high-resolution solid-state NMR spectroscopy using CRAMPS techniques for studies in silicate and cement science, in: P. Colombet, A.R. Grimmer (Eds.), Applications of NMR Spectroscopy to Cement Science, Gordon and Breach, Amsterdam, 1994, pp. 77–102.

[183] E. Pustovgar, R.P. Sangodkar, A.S. Andreev, M. Palacios, B.F. Chmelka, R.J. Flatt, et al., Understanding silicate hydration from quantitative analyses of hydrating tricalcium silicates, Nat. Commun. 7 (2016) 10952.

[184] I.G. Richardson, G.W. Groves, The structure of the calcium silicate hydrate phases present in hardened pastes of white Portland cement/blast-furnace slag blends, J. Mater. Sci. 32 (1997) 4793–4802.

[185] I.G. Richardson, A.R. Brough, G.W. Groves, C.M. Dobson, The characterization of hardened alkali-activated blast-furnace slag pastes and the nature of the calcium silicate hydrate (C–S–H) paste, Cement Concr. Res. 24 (1994) 813–829.

[186] M.D. Andersen, H.J. Jakobsen, J. Skibsted, Characterization of white Portland cement hydration and the C-S-H structure in the presence of sodium aluminate by ^{27}Al and ^{29}Si MAS NMR spectroscopy, Cement Concr. Res. 34 (2004) 857–868.

[187] C.A. Love, I.G. Richardson, A.R. Brough, Composition and structure of C–S–H in white Portland cement–20% metakaolin pastes hydrated at 25 °C, Cement Concr. Res. 37 (2007) 109–117.

[188] X. Pardal, F. Brunet, T. Charpentier, I. Pochard, A. Nonat, ^{27}Al and ^{29}Si solid-state NMR characterization of calcium-aluminosilicate-hydrate, Inorg. Chem. 51 (2012) 1827–1836.

[189] M.D. Jackson, J. Moon, E. Gotti, R. Taylor, S.R. Chae, M. Kunz, et al., Material and elastic properties of Al-tobermorite in ancient roman seawater concrete, J. Am. Ceram. Soc. 96 (2013) 2598–2606.

[190] I.G. Richardson, A.R. Brough, R. Brydson, G.W. Groves, C.M. Dobson, Location of aluminum in substituted calcium silicate hydrate (C-S-H) gels as determined by ^{29}Si and ^{27}Al NMR and EELS, J. Am. Ceram. Soc. 76 (1993) 2285–2288.

[191] L. Pegado, C. Labbez, S.V. Churakov, Mechanism of aluminium incorporation into C–S–H from ab initio calculations, J. Mater. Chem. A 2 (2014) 3477.

[192] P. Faucon, A. Delagrave, C. Richet, J.M. Marchand, H. Zanni, Aluminum incorporation in calcium silicate hydrates (C–S–H) depending on their Ca/Si ratio, J. Phys. Chem. B 103 (1999) 7796–7802.

[193] G.K. Sun, J.F. Young, R.J. Kirkpatrick, The role of Al in C–S–H: NMR, XRD, and compositional results for precipitated samples, Cement Concr. Res. 36 (2006) 18–29.

[194] M.D. Andersen, H.J. Jakobsen, J. Skibsted, A new aluminium-hydrate species in hydrated Portland cements characterized by ^{27}Al and ^{29}Si MAS NMR spectroscopy, Cement Concr. Res. 36 (2006) 3–17.

[195] R.J. Myers, S.A. Bernal, R. San Nicolas, J.L. Provis, Generalized structural description of calcium-sodium aluminosilicate hydrate gels: the cross-linked substituted tobermorite model, Langmuir 29 (2013) 5294–5306.

[196] A. Fernández-Jiménez, F. Puertas, Structure of calcium silicate hydrates formed in alkaline-activated slag: influence of the type of alkaline activator, J. Am. Ceram. Soc. 86 (2003) 1389–1394.

[197] J. Schneider, M.A. Cincotto, H. Panepucci, ^{29}Si and ^{27}Al high-resolution NMR characterization of calcium silicate hydrate phases in activated blast-furnace slag pastes, Cement Concr. Res. 31 (2001) 993.

[198] H. Manzano, J.S. Dolado, A. Ayuela, Aluminum incorporation to dreierketten silicate chains, J. Phys. Chem. B 113 (2009) 2832–2839.

[199] F. Puertas, M. Palacios, H. Manzano, J.S. Dolado, A. Rico, J. Rodriguez, A model for the C-A-S-H gel formed in alkali-activated slag cements, J. Eur. Ceram. Soc. 31 (2011) 2043–2056.

[200] S. Grangeon, F. Claret, C. Roosz, T. Sato, S. Gaboreau, Y. Linard, Structure of nanocrystalline calcium silicate hydrates: insights from X-ray diffraction, synchrotron X-ray absorption and nuclear magnetic resonance, J. Appl. Crystallogr. 49 (2016) 771–783.

[201] E.M. L'Hôpital, B. Lothenbach, D.A. Kulik, K. Scrivener, Influence of calcium to silica ratio on aluminium uptake in calcium silicate hydrate, Cement Concr. Res. 85 (2016) 111–121.

[202] É.M. L'Hôpital, Aluminium and Alkali Uptake in Calcium Silicate Hydrates (C-S-H), Ph.D. thesis, École Polytechnique Fédérale de Lausanne, Lausanne, Switzerland, 2014.

[203] B. Walkley, J.L. Provis, R. San Nicolas, M.A. Sani, J.S.J. van Deventer, Stoichiometrically controlled C–(A)–S–H/N–A–S–H gel blends via alkali-activation of synthetic precursors, Adv. Appl. Ceram. 114 (2015) 372–377.

[204] R.J. Myers, É.M. L'Hôpital, J.L. Provis, B. Lothenbach, Composition-solubility-structure relationships in calcium (alkali) aluminosilicate hydrate (C-(N,K-)A-S-H), Dalton Trans. 44 (2015) 13530–13544.

[205] X. Pardal, I. Pochard, A. Nonat, Experimental study of Si–Al substitution in calcium-silicate-hydrate (C-S-H) prepared under equilibrium conditions, Cement Concr. Res. 39 (2009) 637–643.

[206] I.G. Richardson, S. Li, Composition and structure of an 18-year-old 5 M KOH-activated ground granulated blast-furnace slag paste, Constr. Build. Mater. 168 (2018) 404–411.

[207] H. Viallis-Terrisse, A. Nonat, J.-C. Petit, Zeta-potential study of calcium silicate hydrates interacting with alkaline cations, J. Colloid Interface Sci. 244 (2001) 58–65.

[208] Y. Kim, R. James Kirkpatrick, ^{23}Na and ^{133}Cs NMR study of cation adsorption on mineral surfaces: local environments, dynamics, and effects of mixed cations, Geochem. Cosmochim. Acta 61 (1997) 5199–5208.

[209] S.-Y. Hong, F.P. Glasser, Alkali sorption by C-S-H and C-A-S-H gels: Part II. Role of alumina, Cement Concr. Res. 32 (2002) 1101–1111.

[210] H. Stade, On the reaction of C-S-H(di, poly) with alkali hydroxides, Cement Concr. Res. 19 (1989) 802–810.

[211] T.T.H. Bach, E. Chabas, I. Pochard, C. Cau Dit Coumes, J. Haas, F. Frizon, et al., Retention of alkali ions by hydrated low-pH cements: mechanism and Na^+/K^+ selectivity, Cement Concr. Res. 51 (2013) 14–21.

[212] T. Chappex, K. Scrivener, Alkali fixation of C–S–H in blended cement pastes and its relation to alkali silica reaction, Cement Concr. Res. 42 (2012) 1049–1054.

[213] É.M. L'Hôpital, B. Lothenbach, K. Scrivener, D.A. Kulik, Alkali uptake in calcium alumina silicate hydrate (C-A-S-H), Cement Concr. Res. 85 (2016) 122–136.

[214] C.E. White, L.L. Daemen, M. Hartl, K. Page, Intrinsic differences in atomic ordering of calcium (alumino)silicate hydrates in conventional and alkali-activated cements, Cement Concr. Res. 67 (2015) 66–73.

[215] R.J. Myers, É.M. L'Hôpital, J.L. Provis, B. Lothenbach, Effect of temperature and aluminium on calcium (alumino)silicate hydrate chemistry under equilibrium conditions, Cement Concr. Res. 68 (2015) 83–93.

[216] K. Enemark-Rasmussen, T.T. Tran, J. Skibsted, Fluoride ions as structural probe-ions in ^{19}F MAS NMR studies of cement materials and thermally activated SCMs, Adv. Cem. Res. 26 (2014) 233–246.

[217] T.T. Tran, H. Bildsøe, H.J. Jakobsen, J. Skibsted, Double cross-polarization MAS NMR in the assignment of abundant-spin resonances: ^{19}F–{^{29}Si}–^{19}F FBCP/MAS NMR of fluoride ions incorporated in calcium silicate hydrate (C–S–H) phases, J. Magn. Reson. 221 (2012) 19–23.

[218] P. Yu, R.J. Kirkpatrick, ^{35}Cl NMR relaxation study of cement hydrate suspensions, Cement Concr. Res. 31 (2001) 1479–1485.

[219] J.V. Hanna, L.P. Aldridge, E.R. Vance, Cs speciation in cements, MRS Proc. 663 (2011) 89–96.

[220] T.F. Sevelsted, D. Herfort, J. Skibsted, ^{13}C chemical shift anisotropies for carbonate ions in cement minerals and the use of ^{13}C, ^{27}Al and ^{29}Si MAS NMR in studies of Portland cement including limestone additions, Cement Concr. Res. 52 (2013) 100–111.

[221] T.F. Sevelsted, J. Skibsted, Carbonation of C–S–H and C–A–S–H samples studied by ^{13}C, ^{27}Al and ^{29}Si MAS NMR spectroscopy, Cement Concr. Res. 71 (2015) 56–65.

[222] J.L. MacDonald, U. Werner-Zwanziger, B. Chen, J.W. Zwanziger, D. Forgeron, A ^{43}Ca and ^{13}C NMR study of the chemical interaction between poly(ethylene–vinyl acetate) and white cement during hydration, Solid State Nucl. Magn. Reson. 40 (2011) 78–83.

[223] J. Rottstegge, M. Wilhelm, H.W. Spiess, Solid state NMR investigations on the role of organic admixtures on the hydration of cement pastes, Cement Concr. Compos. 28 (2006) 417–426.

[224] J. Rottstegge, M. Arnold, L. Herschke, G. Glasser, M. Wilhelm, H.W. Spiess, et al., Solid state NMR and LVSEM studies on the hardening of latex modified tile mortar systems, Cement Concr. Res. 35 (2005) 2233–2243.

[225] Z. Gabelica, J. Davidovits, H.J. Jakobsen, Geopolymerisation of polysialates, in: J. Davidovits, J. Orlinski (Eds.), Geopolymer'88: First European Conference on Soft Mineralurgy. Compiègne, The Geopolymer Institute; The University of Technology of Compiègne, France, 1988.

[226] J. Davidovits, Structural characterization of geopolymeric materials with X-ray diffractometry and MAS-NMR spectroscopy, in: J. Davidovits, J. Orlinski (Eds.), Geopolymer'88: First European Conference on Soft Mineralurgy. Compiègne, The Geopolymer Institute; The University of Technology of Compiègne, France, 1988.

[227] C.A. Rees, J.L. Provis, G.C. Lukey, J.S.J. van Deventer, Attenuated total reflectance Fourier transform infrared analysis of fly ash geopolymer gel aging, Langmuir 23 (2007) 8170–8179.

[228] B. Walkley, R. San Nicolas, M.A. Sani, J.D. Gehman, J.S. van Deventer, J.L. Provis, Phase evolution of Na_2O-Al_2O_3-SiO_2-H_2O gels in synthetic aluminosilicate binders, Dalton Trans. 45 (2016) 5521–5535.

[229] X-m Cui, L-p Liu, G-j Zheng, R-p Wang, J-p Lu, Characterization of chemosynthetic Al_2O_3–$2SiO_2$ geopolymers, J. Non Cryst. Solids 356 (2010) 72–76.

[230] G. Zheng, X. Cui, W. Zhang, Z. Tong, Preparation of geopolymer precursors by sol–gel method and their characterization, J. Mater. Sci. 44 (2009) 3991–3996.

[231] I. García-Lodeiro, A. Palomo, A. Fernández-Jiménez, D.E. Macphee, Compatibility studies between N-A-S-H and C-A-S-H gels. Study in the ternary diagram Na_2O–CaO–Al_2O_3–SiO_2–H_2O, Cement Concr. Res. 41 (2011) 923–931.

[232] J. Davidovits, Properties of geopolymer cements, in: First International Conference on Alkaline Cements and Concretes, Scientific Research Institute on Binders and Materials, Kiev, Ukraine, 1994, pp. 131–149.

[233] P. Duxson, S.W. Mallicoat, G.C. Lukey, W.M. Kriven, J.S.J. van Deventer, The effect of alkali and Si/Al ratio on the development of mechanical properties of metakaolin-based geopolymers, Colloid. Surf. A Physicochem. Eng. Asp. 292 (2007) 8–20.

[234] C. Li, H. Sun, L. Li, A review: the comparison between alkali-activated slag (Si+Ca) and metakaolin (Si+Al) cements, Cement Concr. Res. 40 (2010) 1341–1349.

[235] J. Melar, G. Renaudin, F. Leroux, A. Hardy-Dessources, J.M. Nedelec, C. Taviot-Gueho, et al., The porous network and its interface inside geopolymers as a function of alkali cation and aging, J. Phys. Chem. C 119 (2015) 17619–17632.

[236] M. Criado, A. Fernández-Jiménez, A. Palomo, I. Sobrados, J. Sanz, Effect of the SiO_2/Na_2O ratio on the alkali activation of fly ash. Part II: ^{29}Si MAS-NMR survey, Microporous Mesoporous Mater. 109 (2008) 525–534.

[237] A. Fernández-Jiménez, A. Palomo, I. Sobrados, J. Sanz, The role played by the reactive alumina content in the alkaline activation of fly ashes, Microporous Mesoporous Mater. 91 (2006) 111–119.

[238] K. Ikeda, Preparation of fly ash monoliths consolidated with a sodium silicate binder at ambient temperature, Cement Concr. Res. 27 (1997) 657–663.

[239] J.L. Provis, G.C. Lukey, J.S.J. van Deventer, Do geopolymers actually contain nanocrystalline zeolites? A reexamination of existing results, Chem. Mater. 17 (2005) 3075–3085.

[240] F. Škvára, T. Jílek, L. Kopecký, Geopolymer materials based on fly ash, Ceramics-Silikaty 49 (2005) 195–204.

[241] A. Fernández-Jiménez, M. Monzó, M. Vicent, A. Barba, A. Palomo, Alkaline activation of metakaolin–fly ash mixtures: obtain of zeoceramics and zeocements, Microporous Mesoporous Mater. 108 (2008) 41–49.

[242] J. Brus, L. Kobera, M. Urbanová, D. Koloušek, J. Kotek, Insights into the structural transformations of aluminosilicate inorganic polymers: a comprehensive solid-state NMR study, J. Phys. Chem. C 116 (2012) 14627–14637.

[243] J.E. Oh, Y. Jun, Y. Jeong, Characterization of geopolymers from compositionally and physically different Class F fly ashes, Cement Concr. Compos. 50 (2014) 16–26.

[244] I. García-Lodeiro, A. Fernández-Jimenez, A. Palomo, D.E. Macphee, Effect on fresh C-S-H gels of the simultaneous addition of alkali and aluminium, Cement Concr. Res. 40 (2010) 27–32.

[245] I. García-Lodeiro, A. Fernández-Jiménez, A. Palomo, D.E. Macphee, Effect of calcium additions on N–A–S–H cementitious gels, J. Am. Ceram. Soc. 93 (2010) 1934–1940.

[246] J.L. Provis, J.S.J. van Deventer, Direct measurement of the kinetics of geopolymerisation by in-situ energy dispersive X-ray diffractometry, J. Mater. Sci. 42 (2007) 2974–2981.

[247] C.E. White, J.L. Provis, A. Llobet, T. Proffen, J.S.J. van Deventer, Evolution of local structure in geopolymer gels: an in situ neutron pair distribution function analysis, J. Am. Ceram. Soc. 94 (2011) 3532–3539.

[248] C.E. White, J.L. Provis, T. Proffen, J.S.J. Van Deventer, The effects of temperature on the local structure of metakaolin-based geopolymer binder: a neutron pair distribution function investigation, J. Am. Ceram. Soc. 93 (2010) 3486–3492.

[249] C.E. White, B. Bloomer, J.L. Provis, N.J. Henson, K. Page, The synergy between total scattering and advanced simulation techniques in understanding geopolymer gel evolution: quantifying extent of reaction using in situ X-ray pair distribution function analysis, in: NICOM4: 4th International Symposium on Nanotechnology in Construction. Agios Nikolaos, Greece, 2012.

[250] J.L. Provis, P. Duxson, G.C. Lukey, van Deventer JSJ, Statistical thermodynamic model for Si/Al ordering in amorphous aluminosilicates, Chem. Mater. 17 (2005) 2976–2986.

[251] I. Lecomte, C. Henrist, M. Liégeois, F. Maseri, A. Rulmont, R. Cloots, (Micro)-structural comparison between geopolymers, alkali-activated slag cement and Portland cement, J. Eur. Ceram. Soc. 26 (2006) 3789–3797.

[252] P. Duxson, The Structure and Thermal Evolution of Metakaolin Geopolymers, PhD thesis, The University of Melbourne, Melbourne, Australia, 2006.

[253] A. Hajimohammadi, J.L. Provis, J.S.J. van Deventer, Effect of alumina release rate on the mechanism of geopolymer gel formation, Chem. Mater. 22 (2010) 5199–5208.

[254] A. Hajimohammadi, J.L. Provis, J.S.J. van Deventer, The effect of silica availability on the mechanism of geopolymerisation, Cement Concr. Res. 41 (2011) 210–216.

[255] B. Walkley, G.J. Rees, R. San Nicolas, J.S.J. van Deventer, J.V. Hanna, J.L. Provis, New structural model of hydrous sodium aluminosilicate gels and the role of charge-balancing extra-framework Al, J. Phys. Chem. C 122 (2018) 5673–5685.

[256] M.R. Rowles, J.V. Hanna, K.J. Pike, M.E. Smith, B.H. O'Connor, ^{29}Si, ^{27}Al, ^{1}H and ^{23}Na MAS NMR study of the bonding character in aluminosilicate inorganic polymers, Appl. Magn. Reson. 32 (2007) 663–689.

[257] V.F.F. Barbosa, K.J.D. MacKenzie, C. Thaumaturgo, Synthesis and characterisation of materials based on inorganic polymers of alumina and silica: sodium polysialate polymers, Int. J. Inorg. Mater. 2 (2000) 309–317.

[258] A.Y. Wang-hong, R. James Kirkpatrick, Hydrothermal reaction of albite and a sodium aluminosilicate glass: a solid-state NMR study, Geochem. Cosmochim. Acta 53 (1989) 805–819.

[259] P. Duxson, J.L. Provis, G.C. Lukey, J.S.J. van Deventer, ^{39}K NMR of free potassium in geopolymers, Ind. Eng. Chem. Res. 45 (2006) 9208–9210.

[260] V.F.F. Barbosa, K.J.D. MacKenzie, Synthesis and thermal behaviour of potassium sialate geopolymers, Mater. Lett. 57 (2003) 1477–1482.

[261] M.G. Blackford, J.V. Hanna, K.J. Pike, E.R. Vance, D.S. Perera, Transmission electron microscopy and nuclear magnetic resonance studies of geopolymers for radioactive waste immobilization, J. Am. Ceram. Soc. 90 (2007) 1193–1199.

[262] Y. Kim, R.J. Kirkpatrick, R.T. Cygan, ^{133}Cs NMR study of cesium on the surfaces of kaolinite and illite, Geochem. Cosmochim. Acta 60 (1996) 4059–4074.

[263] S.A. Bernal, E.D. Rodriguez, R. Mejia de Gutierrez, M. Gordillo, J.L. Provis, Mechanical and thermal characterisation of geopolymers based on silicate-activated metakaolin/slag blends, J. Mater. Sci. 46 (2011) 5477–5486.

[264] I. Ismail, S.A. Bernal, J.L. Provis, R. San Nicolas, S. Hamdan, J.S.J. van Deventer, Modification of phase evolution in alkali-activated blast furnace slag by the incorporation of fly ash, Cement Concr. Compos. 45 (2014) 125–135.

[265] C.K. Yip, G.C. Lukey, J.S.J. van Deventer, The coexistence of geopolymeric gel and calcium silicate hydrate at the early stage of alkaline activation, Cement Concr. Res. 35 (2005) 1688–1697.

[266] A. Buchwald, H. Hilbig, C. Kaps, Alkali-activated metakaolin-slag blends—performance and structure in dependence of their composition, J. Mater. Sci. 42 (2007) 3024–3032.

[267] F. Puertas, S. Martinez-Ramirez, S. Alonso, T. Vazquez, Alkali-activated fly ash/slag cement – strength behaviour and hydration products, Cement Concr. Res. 30 (2000) 1625–1632.

[268] F. Puertas, A. Fernández-Jiménez, Mineralogical and microstructural characterisation of alkali-activated fly ash/slag pastes, Cement Concr. Compos. 25 (2003) 287–292.

[269] A.V. Girão, I.G. Richardson, R. Taylor, R.M.D. Brydson, Composition, morphology and nanostructure of C–S–H in 70% white Portland cement–30% fly ash blends hydrated at 55°C, Cement Concr. Res. 40 (2010) 1350–1359.

[270] J. Tailby, K.J.D. MacKenzie, Structure and mechanical properties of aluminosilicate geopolymer composites with Portland cement and its constituent minerals, Cement Concr. Res. 40 (2010) 787–794.

[271] K. Dombrowski, A. Buchwald, M. Weil, The influence of calcium content on the structure and thermal performance of fly ash based geopolymers, J. Mater. Sci. 42 (2007) 3033–3043.

[272] S.A. Bernal, J.L. Provis, V. Rose, R. Mejia de Gutierrez, Evolution of binder structure in sodium silicate-activated slag-metakaolin blends, Cement Concr. Compos. 33 (2011) 46–54.

[273] S.A. Bernal, R. Mejia de Gutierrez, J.L. Provis, V. Rose, Effect of silicate modulus and metakaolin incorporation on the carbonation of alkali silicate-activated slags, Cement Concr. Res. 40 (2010) 898–907.

[274] L. Black, P. Purnell, J. Hill, Current themes in cement research, Adv. Appl. Ceram. 109 (2010) 253–259.

[275] W. Gessner, D. Müller, H.J. Behrens, G. Scheler, Zur Koordination des Aluminiums in den Calciumaluminathydraten $2CaO\cdot Al_2O_3\cdot 8H_2O$ und $CaO\cdot Al_2O_3\cdot 10H_2O$, Z. Anorg. Allg. Chem. 486 (1982) 193–199.

[276] P. Faucon, T. Charpentier, D. Bertrandie, A. Nonat, J. Virlet, J.C. Petit, Characterization of calcium aluminate hydrates and related hydrates of cement pastes by ^{27}Al MQ-MAS NMR, Inorg. Chem. 37 (1998) 3726–3733.

[277] M.A. Chavda, S.A. Bernal, D.C. Apperley, H. Kinoshita, J.L. Provis, Identification of the hydrate gel phases present in phosphate-modified calcium aluminate binders, Cement Concr. Res. 70 (2015) 21–28.

[278] F. Winnefeld, B. Lothenbach, Phase equilibria in the system $Ca_4Al_6O_{12}$-SO_4–Ca_2SiO_4–$CaSO_4$–H_2O referring to the hydration of calcium sulfoaluminate cements, RILEM Tech. Lett. 1 (2016) 10–16.

[279] F. Bullerjahn, M. Zajac, M. Ben Haha, CSA raw mix design: effect on clinker formation and reactivity, Mater. Struct. 48 (2015) 3895–3911.

[280] T. Hanein, I. Galan, F.P. Glasser, S. Skalamprinos, A. Elhoweris, M.S. Imbabi, et al., Stability of ternesite and the production at scale of ternesite-based clinkers, Cement Concr. Res. 98 (2017) 91–100.

[281] B.Z. Dilnesa, B. Lothenbach, G. Le Saout, G. Renaudin, A. Mesbah, Y. Filinchuk, et al., Iron in carbonate containing AFm phases, Cement Concr. Res. 41 (2011) 311–323.

[282] B.Z. Dilnesa, B. Lothenbach, G. Renaudin, A. Wichser, E. Wieland, Stability of monosulfate in the presence of iron, J. Am. Ceram. Soc. 95 (2012) 3305–3316.

[283] B.Z. Dilnesa, E. Wieland, B. Lothenbach, R. Dähn, K.L. Scrivener, Fe-containing phases in hydrated cements, Cement Concr. Res. 58 (2014) 45–55.

[284] A. Cuesta, A.G. De la Torre, I. Santacruz, P. Trtik, J.C. da Silva, A. Diaz, et al., Chemistry and mass density of aluminum hydroxide gel in eco-cements by ptychographic X-ray computed tomography, J. Phys. Chem. C 121 (2017) 3044–3054.

[285] G. Paul, E. Boccaleri, L. Buzzi, F. Canonico, D. Gastaldi, Friedel's salt formation in sulfoaluminate cements: a combined XRD and ^{27}Al MAS NMR study, Cement Concr. Res. 67 (2015) 93–102.

[286] T. Isobe, T. Watanabe, J.-B. d'Espinose de la Caillerie, A. Legrand, D. Massiot, Solid-state ^{1}H and ^{27}Al NMR studies of amorphous aluminum hydroxides, J. Colloid Interface Sci. 261 (2003) 320–324.

[287] A. Vyalikh, K. Zesewitz, U. Scheler, Hydrogen bonds and local symmetry in the crystal structure of gibbsite, Magn. Reson. Chem. 48 (2010) 877–881.

[288] T. Zhang, L.J. Vandeperre, C.R. Cheeseman, Formation of magnesium silicate hydrate (M-S-H) cement pastes using sodium hexametaphosphate, Cement Concr. Res. 65 (2014) 8–14.

[289] T. Zhang, L.J. Vandeperre, C.R. Cheeseman, Magnesium-silicate-hydrate cements for encapsulating problematic aluminium containing wastes, J. Sustain. Cem. Based Mater. 1 (2012) 34–45.

[290] T. Zhang, C.R. Cheeseman, L.J. Vandeperre, Development of low pH cement systems forming magnesium silicate hydrate (M-S-H), Cement Concr. Res. 41 (2011) 439–442.

[291] C. Roosz, S. Grangeon, P. Blanc, V. Montouillout, B. Lothenbach, P. Henocq, et al., Crystal structure of magnesium silicate hydrates (M-S-H): the relation with 2:1 Mg–Si phyllosilicates, Cement Concr. Res. 73 (2015) 228–237.

[292] D.R.M. Brew, F.P. Glasser, Synthesis and characterisation of magnesium silicate hydrate gels, Cement Concr. Res. 35 (2005) 85–98.

[293] E. Bernard, B. Lothenbach, D. Rentsch, I. Pochard, A. Dauzères, Formation of magnesium silicate hydrates (M-S-H), Phys. Chem. Earth Parts A/B/C 99 (2017) 142–157.

[294] J. Temuujin, K. Okada, K.J. MacKenzie, Formation of layered magnesium silicate during the aging of magnesium hydroxide–silica mixtures, J. Am. Ceram. Soc. 81 (1998) 754–756.

[295] J.-B. d'Espinose de la Caillerie, M. Kermarec, O. Clause, ^{29}Si NMR observation of an amorphous magnesium silicate formed during impregnation of silica with Mg (II) in aqueous solution, J. Phys. Chem. 99 (1995) 17273–17281.

[296] M. Tonelli, F. Martini, L. Calucci, E. Fratini, M. Geppi, F. Ridi, et al., Structural characterization of magnesium silicate hydrate: towards the design of eco-sustainable cements, Dalton Trans. 45 (2016) 3294–3304.

[297] A. Pedone, F. Palazzetti, V. Barone, Models of aged magnesium–silicate–hydrate cements based on the lizardite and talc crystals: a periodic DFT-GIPAW investigation, J. Phys. Chem. C 121 (2017) 7319–7330.

[298] B. Lothenbach, D. Nied, E. L'Hôpital, G. Achiedo, A. Dauzères, Magnesium and calcium silicate hydrates, Cement Concr. Res. 77 (2015) 60–68.

[299] K.J.D. MacKenzie, S. Bradley, J.V. Hanna, M.E. Smith, Magnesium analogues of aluminosilicate inorganic polymers (geopolymers) from magnesium minerals, J. Mater. Sci. 48 (2013) 1787–1793.

[300] A.D. Wilson, J.W. Nicholson, Acid-Base Cements: Their Biomedical and Industrial Applications, Cambridge University Press, 2005.

[301] M. Mathew, L.W. Schroeder, Crystal structure of a struvite analogue, $MgKPO_4 \cdot 6H_2O$, Acta Crystallogr. B 35 (1979) 11–13.

[302] S. Graeser, W. Postl, H.-P. Bojar, P. Berlepsch, T. Armbruster, T. Raber, et al., Struvite-(K), $KMgPO_4 \cdot 6H_2O$, the potassium equivalent of struvite – a new mineral, Eur. J. Mineral. 20 (2008) 629–633.

[303] L.J. Gardner, S.A. Bernal, S.A. Walling, C.L. Corkhill, J.L. Provis, N.C. Hyatt, Characterisation of magnesium potassium phosphate cements blended with fly ash and ground granulated blast furnace slag, Cement Concr. Res. 74 (2015) 78–87.

[304] S.N. Scrimgeour, J.A. Chudek, G.A. Cowper, C.H. Lloyd, ^{31}P solid-state MAS-NMR spectroscopy of the compounds that form in phosphate-bonded dental casting investment materials during setting, Dent. Mater. 23 (2007) 934–943.

[305] D. Laurencin, C. Gervais, H. Stork, S. Krämer, D. Massiot, F. Fayon, ^{25}Mg solid-state NMR of magnesium phosphates: high magnetic field experiments and density functional theory calculations, J. Phys. Chem. C 116 (2012) 19984–19995.

[306] L.J. Gardner, S.A. Walling, S.A. Bernal, C.L. Corkhill, D. Iuga, J.L. Provis, et al., Characterisation of struvite-K, $MgKPO_4 \cdot 6H_2O$, an analogue of struvite (manuscript in preparation), 2019.

[307] B. Lothenbach, F. Winnefeld, Thermodynamic modelling of the hydration of Portland cement, Cement Concr. Res. 36 (2006) 209–226.

[308] S.-Y. Hong, F.P. Glasser, Alkali binding in cement pastes: part I. The C-S-H phase, Cement Concr. Res. 29 (1999) 1893–1903.

[309] H. Zanni, R. Rassem-Bertolo, S. Masse, L. Fernandez, P. Nieto, B. Bresson, A spectroscopic NMR investigation of the calcium silicate hydrates present in cement and concrete, Magn. Reson. Imag. 14 (1996) 827–831.

[310] F. Méducin, B. Bresson, N. Lequeux, M.-N. de Noirfontaine, H. Zanni, Calcium silicate hydrates investigated by solid-state high resolution ^{1}H and ^{29}Si nuclear magnetic resonance, Cement Concr. Res. 37 (2007) 631–638.

[311] E. Scholtzová, L. Kucková, J. Kožíšek, D. Tunega, Structural and spectroscopic characterization of ettringite mineral-combined DFT and experimental study, J. Mol. Struct. 1100 (2015) 215–224.

[312] A. Moore, H. Taylor, Crystal structure of ettringite, Acta Crystallogr. B 26 (1970) 386–393.

[313] F. Goetz-Neunhoeffer, J. Neubauer, Refined ettringite ($Ca_6Al_2(SO_4)_3(OH)_{12} \cdot 26H_2O$) structure for quantitative X-ray diffraction analysis, Powder Diffr. 21 (2006) 4–11.

[314] A. Katz, A. Brough, R. Kirkpatrick, L. Struble, G. Sun, J. Young, Cement solidification of simulated off-gas condensates from vitrification of low-level nuclear waste solutions, Waste Manag. 21 (2001) 543–553.

[315] G. Le Saout, E. Lécolier, A. Rivereau, H. Zanni, Chemical structure of cement aged at normal and elevated temperatures and pressures: part II: low permeability class G oilwell cement, Cement Concr. Res. 36 (2006) 71–78.

[316] M.R. Hansen, M. Brorson, H. Bildsøe, J. Skibsted, H.J. Jakobsen, Sensitivity enhancement in natural-abundance solid-state ^{33}S MAS NMR spectroscopy employing adiabatic inversion pulses to the satellite transitions, J. Magn. Reson. 190 (2008) 316–326.

[317] W. Lukas, Substitution of Si in the lattice of ettringite, Cement Concr. Res. 6 (1976) 225–233.

[318] A.-R. Grimmer, W. Wieker, F.V. Lampe, E. Fechner, R. Peter, G. Molgedey, Hochauflösende ^{29}Si-NMR an festen Silicaten: anisotropie der chemischen Verschiebung im Thaumasit, Z. Chem. 20 (1980) 453.

[319] E. Lippmaa, M. Maegi, A. Samoson, G. Engelhardt, A.R. Grimmer, Structural studies of silicates by solid-state high-resolution silicon-29 NMR, J. Am. Chem. Soc. 102 (1980) 4889–4893.

[320] J. Skibsted, L. Hjorth, H.J. Jakobsen, Quantification of thaumasite in cementitious materials by ^{29}Si{^{1}H} cross-polarization magic-angle spinning NMR spectroscopy, Adv. Cem. Res. 7 (1995) 69–83.

[321] R.A. Edge, H.F.W. Taylor, Crystal structure of thaumasite, $[Ca_3Si(OH)_6 \cdot 12H_2O](SO_4)(CO_3)$, Acta Crystallogr. B 27 (1971) 594–601.

[322] T. Matschei, B. Lothenbach, F.P. Glasser, The AFm phase in Portland cement, Cement Concr. Res. 37 (2007) 118–130.

[323] C. Famy, A. Brough, H. Taylor, The CSH gel of Portland cement mortars: Part I. The interpretation of energy-dispersive X-ray microanalyses from scanning electron microscopy, with some observations on CSH, AFm and AFt phase compositions, Cement Concr. Res. 33 (2003) 1389–1398.

[324] S.D. Wang, K.L. Scrivener, Hydration products of alkali-activated slag cement, Cement Concr. Res. 25 (1995) 561–571.

[325] X. Ke, S.A. Bernal, J.L. Provis, Controlling the reaction kinetics of sodium carbonate-activated slag cements using calcined layered double hydroxides, Cement Concr. Res. 81 (2016) 24–37.

[326] S.A. Bernal, J.L. Provis, R.J. Myers, R. San Nicolas, J.S.J. van Deventer, Role of carbonates in the chemical evolution of sodium carbonate-activated slag binders, Mater. Struct. 48 (2015) 517–529.

[327] R. Allmann, Refinement of the hybrid layer structure $[Ca_2Al(OH)_6]^+ \cdot [^1/_2SO_4 \cdot 3H_2O]^-$, Neues Jahrb. Mineral. Monatsh. 1977 (1977) 136–143.

[328] G. Renaudin, M. Francois, O. Evrard, Order and disorder in the lamellar hydrated tetracalcium monocarboaluminate compound, Cement Concr. Res. 29 (1999) 63–69.

[329] M. François, G. Renaudin, O. Evrard, A cementitious compound with composition $3CaO \cdot Al_2O_3 \cdot CaCO_3 \cdot 11H_2O$, Acta Crystallogr. Sect. C Cryst. Struct. Commun. 54 (1998) 1214–1217.

[330] F. Buttler, L. Dent Glasser, H. Taylor, Studies on $4CaO \cdot Al_2O_3 \cdot 13H_2O$ and the related natural mineral hydrocalumite, J. Am. Ceram. Soc. 42 (1959) 121–126.

[331] B. Lothenbach, G. Le Saoût, E. Gallucci, K. Scrivener, Influence of limestone on the hydration of Portland cements, Cement Concr. Res. 38 (2008) 848–860.

[332] S. Ahmed, H. Taylor, Crystal structures of the lamellar calcium aluminate hydrates, Nature 215 (1967) 622–623.

[333] S. Kwan, J. LaRosa, M.W. Grutzeck, ^{29}Si and ^{27}Al MAS NMR strätlingite, J. Am. Ceram. Soc. 78 (1995) 1921–1926.

[334] R. Rinaldi, M. Sacerdoti, E. Passaglia, Strätlingite: crystal structure, chemistry, and a reexamination of its polytype vertumnite, Eur. J. Mineral. (1990) 841–850.

[335] W. Geßner, D. Müller, Festkörper-NMR-untersuchungen am gehlenithydrat $2CaO \cdot Al_2O_3 \cdot SiO_2 \cdot 8H_2O$, Z. Chem. 29 (1989) 344–345.

[336] R.J. Kirkpatrick, P. Yu, X. Hou, Y. Kim, Interlayer structure, anion dynamics, and phase transitions in mixed-metal layered hydroxides; variable temperature ^{35}Cl NMR spectroscopy of hydrotalcite and Ca-aluminate hydrate (hydrocalumite), Am. Mineral. 84 (1999) 1186–1190.

[337] R. Taylor, I.G. Richardson, R.M.D. Brydson, Composition and microstructure of 20-year-old ordinary Portland cement–ground granulated blast-furnace slag blends containing 0 to 100% slag, Cement Concr. Res. 40 (2010) 971–983.

[338] B. Lothenbach, A. Gruskovnjak, Hydration of alkali-activated slag: thermodynamic modelling, Adv. Cem. Res. 19 (2007) 81–92.

[339] J.L. Provis, J.S.J. van Deventer, Alkali Activated Materials. State-of-the-Art Report, RILEM TC 224-AAM, Springer, Dordrecht, 2014.

[340] H.F.W. Taylor, Sulfate reactions in concrete – microstructural and chemical aspects, Ceram. Trans. 40 (1994) 61–78.

[341] S. Mills, A. Christy, J.-M. Génin, T. Kameda, F. Colombo, Nomenclature of the hydrotalcite supergroup: natural layered double hydroxides, Mineral. Mag. 76 (2012) 1289–1336.

[342] K.J.D. MacKenzie, R.H. Meinhold, B.L. Sherriff, Z. Xu, ^{27}Al and ^{25}Mg solid-state magic-angle spinning nuclear magnetic resonance study of hydrotalcite and its thermal decomposition sequence, J. Mater. Chem. 3 (1993) 1263.

[343] R.K. Allada, J.D. Pless, T.M. Nenoff, A. Navrotsky, Thermochemistry of hydrotalcite-like phases intercalated with CO_3^{2-}, NO_3^-, Cl^-, I^-, and ReO_4^-, Chem. Mater. 17 (2005) 2455–2459.

[344] R. Snellings, T. Paulhiac, K. Scrivener, The effect of Mg on slag reactivity in blended cements, Waste Biomass Valoriz. 5 (2014) 369–383.

[345] H.M. Dyson, I.G. Richardson, A.R. Brough, A combined ^{29}Si MAS NMR and selective dissolution technique for the quantitative evaluation of hydrated blast furnace slag cement blends, J. Am. Ceram. Soc. 90 (2007) 598–602.

[346] R. Brydson, I.G. Richardson, G.W. Groves, Determining the local coordination of aluminium in cement using electron energy loss near-edge structure, Microchim. Acta 114 (1994) 221–229.

[347] I.G. Richardson, Clarification of possible ordered distributions of trivalent cations in layered double hydroxides and an explanation for the observed variation in the lower solid-solution limit, Acta Crystallogr. B 69 (2013) 629–633.

[348] X. Ke, S.A. Bernal, J.L. Provis, Uptake of chloride and carbonate by Mg-Al and Ca-Al layered double hydroxides in simulated pore solutions of alkali-activated slag cement, Cement Concr. Res. 100 (2017) 1–13.

[349] R.J. Myers, B. Lothenbach, S.A. Bernal, J.L. Provis, Thermodynamic modelling of alkali-activated slag cements, Appl. Geochem. 61 (2015) 233–247.

[350] D.M. Roy, E. Sonnenthal, R. Prave, Hydrotalcite observed in mortars exposed to sulfate solutions, Cement Concr. Res. 15 (1985) 914–916.

[351] G. Mascolo, Hydration products of synthetic glasses similar to blast-furnace slags, Cement Concr. Res. 3 (1973) 207–213.

[352] R. Allmann, H. Jepsen, Die struktur des hydrotalkits, Neues Jahrb. Mineral. Monatsh. 1969 (1969) 544–551.

[353] J. Rocha, M. del Arco, V. Rives, M.A. Ulibarri, Reconstruction of layered double hydroxides from calcined precursors: a powder XRD and ^{27}Al MAS NMR study, J. Mater. Chem. 9 (1999) 2499–2503.

[354] P.J. Sideris, F. Blanc, Z. Gan, C.P. Grey, Identification of cation clustering in Mg–Al layered double hydroxides using multinuclear solid state nuclear magnetic resonance spectroscopy, Chem. Mater. 24 (2012) 2449–2461.

[355] L. Zhao, Z. Qi, F. Blanc, G. Yu, M. Wang, N. Xue, et al., Investigating local structure in layered double hydroxides with ^{17}O NMR spectroscopy, Adv. Funct. Mater. 24 (2014) 1696–1702.

[356] B. Lothenbach, E. Wieland, A thermodynamic approach to the hydration of sulphate-resisting Portland cement, Waste Manag. 26 (2006) 706–719.

[357] N.C. Collier, N.B. Milestone, J. Hill, I.H. Godfrey, Immobilisation of Fe floc: part 2, encapsulation of floc in composite cement, J. Nucl. Mater. 393 (2009) 92–101.

[358] G. Le Saout, E. Lécolier, A. Rivereau, H. Zanni, Chemical structure of cement aged at normal and elevated temperatures and pressures: part I. Class G oilwell cement, Cement Concr. Res. 36 (2006) 71–78.

[359] B. Lothenbach, T. Matschei, G. Möschner, F.P. Glasser, Thermodynamic modelling of the effect of temperature on the hydration and porosity of Portland cement, Cement Concr. Res. 38 (2008) 1–18.

[360] N. Neuville, E. Lécolier, G. Aouad, A. Rivereau, D. Damidot, Effect of curing conditions on oilwell cement paste behaviour during leaching: experimental and modelling approaches, Compt. Rendus Chim. 12 (2009) 511–520.

[361] N.C. Collier, N.B. Milestone, J. Hill, I.H. Godfrey, The disposal of radioactive ferric floc, Waste Manag. 26 (2006) 769–775.

[362] J.M. Rivas Mercury, P. Pena, A.H. De Aza, X. Turrillas, I. Sobrados, J. Sanz, Solid-state ^{27}Al and ^{29}Si NMR investigations on Si-substituted hydrogarnets, Acta Mater. 55 (2007) 1183–1191.

[363] J. Mahler, A. Sebald, Deconvolution of ^{29}Si magic-angle spinning nuclear magnetic resonance spectra of silicate glasses revisited – some critical comments, Solid State Nucl. Magn. Reson. 5 (1995) 63–78.

[364] L. Petrakis, Spectral line shapes: Gaussian and Lorentzian functions in magnetic resonance, J. Chem. Educ. 44 (1967) 432.

[365] J.H. Van Vleck, Line-breadths and the theory of magnetism, Il Nuovo Cimento 6 (1957) 993–1014.

[366] B. Walkley, S.J. Page, G.J. Rees, J.L. Provis, J.V. Hanna, Nanostructural development of synthetic CaO-(Na_2O)-Al_2O_3-SiO_2-H_2O gels revealed by multinuclear MQMAS NMR (manuscript in preparation), 2019.

[367] A. Samoson, Satellite transition high-resolution NMR of quadrupolar nuclei in powders, Chem. Phys. Lett. 119 (1985) 29–32.

[368] J. Skibsted, N.C. Nielsen, H. Bildsøe, H.J. Jakobsen, Satellite transitions in MAS NMR spectra of quadrupolar nuclei, J. Magn. Reson. 95 (1991) 88–117.

[369] C. Jäger, Satellite transition spectroscopy of quadrupolar nuclei, in: B. Blumich, R. Kosfeld (Eds.), NMR Basic Principles and Progress: Solid-State NMR II, Springer-Verlag, Berlin, 1994, p. 135.

[370] J. Brus, S. Abbrent, L. Kobera, M. Urbanová, P. Cuba, Advances in ^{27}Al MAS NMR studies of geopolymers, Annu. Rep. NMR Spectrosc. 88 (2016) 79–147.

[371] J.D. Gehman, J.L. Provis, Generalized biaxial shearing of MQMAS NMR spectra, J. Magn. Reson. 200 (2009) 167–172.

[372] T.F. Kemp, M.E. Smith, QuadFit—a new cross-platform computer program for simulation of NMR line shapes from solids with distributions of interaction parameters, Solid State Nucl. Magn. Reson. 35 (2009) 243–252.

[373] J.-B. d'Espinose de Lacaillerie, C. Fretigny, D. Massiot, MAS NMR spectra of quadrupolar nuclei in disordered solids: the Czjzek model, J. Magn. Reson. 192 (2008) 244–251.

[374] P.T. Durdziński, M. Ben Haha, S.A. Bernal, N. De Belie, E. Gruyaert, B. Lothenbach, et al., Outcomes of the RILEM round robin on degree of reaction of slag and fly ash in blended cements, Mater. Struct. 50 (2017) 135.

[375] J. Lumley, R. Gollop, G. Moir, H. Taylor, Degrees of reaction of the slag in some blends with Portland cements, Cement Concr. Res. 26 (1996) 139–151.

[376] J. Rossen, K. Scrivener, Optimization of SEM-EDS to determine the C–A–S–H composition in matured cement paste samples, Mater. Char. 123 (2017) 294–306.

[377] N.V. Scarlett, I.C. Madsen, Quantification of phases with partial or no known crystal structures, Powder Diffr. 21 (2006) 278–284.

[378] C.A. Fyfe, J.L. Bretherton, L.Y. Lam, Detection of the 'invisible aluminium' and characterisation of the multiple aluminium environments in zeolite USY by high-field solid-state NMR, Chem. Commun. (2000) 1575–1576.

[379] R.H. Bogue, The Chemistry of Portland Cement, Reinhold, 1955.

[380] H.F. Taylor, Modification of the Bogue calculation, Adv. Cem. Res. 2 (1989) 73–77.

[381] M. Kaupp, B. Michael, V.G. Malkin, Calculation of NMR and EPR Parameters: Theory and Applications, John Wiley & Sons, 2006.

[382] L.B. Casabianca, A.C. de Dios, Ab initio calculations of NMR chemical shifts, J. Chem. Phys. 128 (2008) 052201.

[383] E.L. Hahn, Spin echoes, Phys. Rev. 80 (1950) 580–594.

[384] D. Nied, K. Enemark-Rasmussen, E. L'Hopital, J. Skibsted, B. Lothenbach, Properties of magnesium silicate hydrates (M-S-H), Cement Concr. Res. 79 (2016) 323–332.

[385] S.R. Hartmann, E.L. Hahn, Nuclear double resonance in the rotating frame, Phys. Rev. 128 (1962) 2042–2053.

[386] Y. Tong, H. Du, L. Fei, CP/MAS NMR studies of the initial hydration processes of activated and ordinary beta-dicalcium silicates, Cement Concr. Res. 20 (1990) 986–991.

[387] X. Cong, R.J. Kirkpatrick, ^{1}H — ^{29}Si CPMAS NMR study of the structure of calcium silicate hydrate, Adv. Cem. Res. 7 (1995) 103–111.

[388] S.A. Rodger, G.W. Groves, N.J. Clayden, C.M. Dobson, Hydration of tricalcium silicate followed by ^{29}Si NMR with cross-polarization, J. Am. Ceram. Soc. 71 (1988) 91–96.

[389] R. Rassem, H. Zanni-Theveneau, I. Schneid, M. Regourd, ^{29}Si high-resolution NMR study of tricalcium silicate hydration, J. Chim. Phys. 86 (1989) 1253–1264.

[390] J.F. Young, Investigations of calcium silicate hydrate structure using silicon-29 nuclear magnetic resonance spectroscopy, J. Am. Ceram. Soc. 71 (1988) C118–C120.

[391] Y. Okada, H. Ishida, T. Mitsuda, ^{29}Si NMR spectroscopy of silicate anions in hydrothermally formed C-S-H, J. Am. Ceram. Soc. 77 (1994) 765–768.

[392] I.G. Richardson, The nature of C-S-H in hardened cements, Cement Concr. Res. 29 (1999) 1131–1147.

[393] J.R. Houston, R.S. Maxwell, S.A. Carroll, Transformation of meta-stable calcium silicate hydrates to tobermorite: reaction kinetics and molecular structure from XRD and NMR spectroscopy, Geochem. Trans. 10 (2009) 1–14.

[394] L. Frydman, J.S. Harwood, Isotropic spectra of half-integer quadrupolar spins from bidimensional magic-angle-spinning NMR, J. Am. Chem. Soc. 117 (1995) 5367–5368.

[395] A. Medek, J.S. Harwood, L. Frydman, Multiple-quantum magic-angle spinning NMR: a new method for the study of quadrupolar nuclei in solids, J. Am. Chem. Soc. 117 (1995) 12779–12787.

[396] T.T. Tran, S.A. Bernal, D. Herfort, J. Skibsted, Characterization of the network structure of alkali-activated aluminosilicate binders by single- and double-resonance ^{29}Si {^{27}Al} MAS NMR experiments, in: M.A.T.M. Broekmans (Ed.), Proceedings of the 10th International Congress for Applied Mineralogy. Trondheim, 2011, pp. 707–715.

[397] T.-J. Park, S.-S. Choi, Y. Kim, ^{27}Al solid-state NMR structural studies of hydrotalcite compounds calcined at different temperatures, Bull. Korean Chem. Soc. 30 (2009).

[398] D. Massiot, B. Touzo, D. Trumeau, J.P. Coutures, J. Virlet, P. Florian, et al., Two-dimensional magic-angle spinning isotropic reconstruction sequences for quadrupolar nuclei, Solid State Nucl. Magn. Reson. 6 (1996) 73–83.

[399] I. Hung, J. Trébosc, G.L. Hoatson, R.L. Vold, J.-P. Amoureux, Z. Gan, Q-shear transformation for MQMAS and STMAS NMR spectra, J. Magn. Reson. 201 (2009) 81–86.

[400] T. Gullion, Measurement of dipolar interactions between spin-12 and quadrupolar nuclei by rotational-echo, adiabatic-passage, double-resonance NMR, Chem. Phys. Lett. 246 (1995) 325–330.

[401] T. Gullion, J. Schaefer, Rotational-echo double-resonance NMR, J. Magn. Reson. (1969) 81 (1989) 196–200.

[402] E.R.H. van Eck, W.S. Veeman, Spin density description of rotational-echo double-resonance, transferred-echo double-resonance and two-dimensional transferred-echo double-resonance solid state nuclear magnetic resonance, Solid State Nucl. Magn. Reson. 2 (1993) 307–315.

[403] E.R.H. van Eck, W.S. Veeman, The determination of the average ^{27}Al-^{31}P distance in aluminophosphate molecular sieves with SEDOR NMR, Solid State Nucl. Magn. Reson. 1 (1992) 1–4.

[404] A.W. Hing, S. Vega, J. Schaefer, Transferred-echo double-resonance NMR, J. Magn. Reson. 96 (1992) 205–209.

[405] A.W. Hing, S. Vega, J. Schaefer, Measurement of heteronuclear dipolar coupling by transferred-echo double-resonance NMR, J. Magn. Reson. A 103 (1993) 151–162.

[406] C.P. Grey, W.S. Veeman, The detection of weak heteronuclear coupling between spin 1 and spin 1/2 nuclei in MAS NMR; ^{14}N/^{13}C/^{1}H triple resonance experiments, Chem. Phys. Lett. 192 (1992) 379–385.

[407] C.P. Grey, W.S. Veeman, A.J. Vega, Rotational echo ^{14}N/1^{3}C/^{1}H triple resonance solid-state nuclear magnetic resonance: a probe of ^{13}C–^{14}N internuclear distances, J. Chem. Phys. 98 (1993) 7711–7724.

[408] T. Gullion, Detecting ^{13}C–^{17}O dipolar interactions by rotational-echo, adiabatic-passage, double-resonance NMR, J. Magn. Reson. A 117 (1995) 326–329.

[409] S. Greiser, G.J.G. Gluth, P. Sturm, C. Jäger, ^{29}Si{^{27}Al}, ^{27}Al{^{29}Si} and ^{27}Al{^{1}H} double-resonance NMR spectroscopy study of cementitious sodium aluminosilicate gels (geopolymers) and gel–zeolite composites, RSC Adv. 8 (2018) 40164–40171.

[410] A. Goldbourt, S. Vega, T. Gullion, A.J. Vega, Interatomic distance measurement in solid-state NMR between a spin-1/2 and a spin-5/2 using a universal REAPDOR curve, J. Am. Chem. Soc. 125 (2003) 11194–11195.

[411] A. Bax, S. Subramanian, Sensitivity-enhanced two-dimensional heteronuclear shift correlation NMR spectroscopy, J. Magn. Reson. 67 (1986) 565–569.

[412] H.J. Jakobsen, J. Skibsted, H. Bildsøe, N.C. Nielsen, Magic-angle spinning NMR spectra of satellite transitions for quadrupolar nuclei in solids, J. Magn. Reson. 85 (1989) 173–180.

[413] J. Rocha, J.D. Pedrosa, D.E. Jesus, ^{27}Al satellite transition MAS-NMR spectroscopy of kaolinite, Clay Miner. 29 (1994) 287–291.

[414] D. Bish, R. Von Dreele, Rietveld refinement of non-hydrogen atomic positions in kaolinite, Clays Clay Miner. 37 (1989) 289–296.

[415] R. Blaine, Proton magnetic resonance (NMR) in hydrated Portland cements, Natl. Bur. Stand. Monogr. 43 (1960) 501–511.

[416] D. Lasic, J. Corbett, J. Jian, J. MacTavish, M. Pintar, R. Blinc, et al., NMR spin grouping in hydrating cement at 200 MHz, Cement Concr. Res. 18 (1988) 649–653.

[417] R. Blinc, M. Burgar, G. Lahajnar, M. Rožmarin, V. Rutar, I. Kocuvan, et al., NMR relaxation study of adsorbed water in cement and C$_3$S pastes, J. Am. Ceram. Soc. 61 (1978) 35–37.

[418] K. Kawachi, M. Murakami, E. Hirahara, The hydration and hardening of cement. The nuclear magnetic resonance absorption of water molecules in cement, Bull. Fac. Eng. Hiroshima Univ. 4 (1955) 95–100.

[419] P. Seligmann, Nuclear magnetic resonance studies of the water in hardened cement paste, Portland Cem. Assoc. Lab. Bull. 222 (1968).

[420] L. Miljkovic, D. Lasic, J. MacTavish, M. Pintar, R. Blinc, G. Lahajnar, NMR studies of hydrating cement: a spin-spin relaxation study of the early hydration stage, Cement Concr. Res. 18 (1988) 951–956.

[421] L. Schreiner, J. Mactavish, L. Miljković, M. Pintar, R. Blinc, G. Lahajnar, et al., NMR line shape-spin-lattice relaxation correlation study of Portland cement hydration, J. Am. Ceram. Soc. 68 (1985) 10–16.

[422] R. Holly, E. Reardon, C. Hansson, H. Peemoeller, Proton spin–spin relaxation study of the effect of temperature on white cement hydration, J. Am. Ceram. Soc. 90 (2007) 570–577.

[423] J. Greener, H. Peemoeller, C. Choi, R. Holly, E.J. Reardon, C.M. Hansson, et al., Monitoring of hydration of white cement paste with proton NMR spin–spin relaxation, J. Am. Ceram. Soc. 83 (2000) 623–627.

[424] R. Holly, H. Peemoeller, M. Zhang, E. Reardon, C. Hansson, Magnetic resonance in situ study of tricalcium aluminate hydration in the presence of gypsum, J. Am. Ceram. Soc. 89 (2006) 1022–1027.

[425] M. Gussoni, F. Greco, F. Bonazzi, A. Vezzoli, D. Botta, G. Dotelli, et al., ^{1}H NMR spin-spin relaxation and imaging in porous systems: an application to the morphological study of white Portland cement during hydration in the presence of organics, Magn. Reson. Imag. 22 (2004) 877–889.

[426] A. Plassais, M.-P. Pomiès, N. Lequeux, J.-P. Korb, D. Petit, F. Barberon, et al., Microstructure evolution of hydrated cement pastes, Phys. Rev. 72 (2005) 041401.

[427] P. McDonald, J.-P. Korb, J. Mitchell, L. Monteilhet, Surface relaxation and chemical exchange in hydrating cement pastes: a two-dimensional NMR relaxation study, Phys. Rev. 72 (2005) 011409.

[428] P.J. McDonald, J. Mitchell, M. Mulheron, P.S. Aptaker, J.-P. Korb, L. Monteilhet, Two-dimensional correlation relaxometry studies of cement pastes performed using a new one-sided NMR magnet, Cement Concr. Res. 37 (2007) 303–309.

[429] P.S. Wang, M. Ferguson, G. Eng, D. Bentz, C. Ferraris, J. Clifton, ^{1}H nuclear magnetic resonance characterization of Portland cement: molecular diffusion of water studied by spin relaxation and relaxation time-weighted imaging, J. Mater. Sci. 33 (1998) 3065–3071.

[430] L. Monteilhet, J.-P. Korb, J. Mitchell, P. McDonald, Observation of exchange of micropore water in cement pastes by two-dimensional T$_2$–T$_2$ nuclear magnetic resonance relaxometry, Phys. Rev. E 74 (2006) 061404.

[431] A. Valori, V. Rodin, P. McDonald, On the interpretation of ^{1}H 2-dimensional NMR relaxation exchange spectra in cements: is there exchange between pores with two characteristic sizes or Fe^{3+} concentrations? Cement Concr. Res. 40 (2010) 1375–1377.

[432] J.-Y. Jehng, D. Sprague, W. Halperin, Pore structure of hydrating cement paste by magnetic resonance relaxation analysis and freezing, Magn. Reson. Imag. 14 (1996) 785–791.

[433] R. Valckenborg, L. Pel, K. Kopinga, Combined NMR cryoporometry and relaxometry, J. Phys. D Appl. Phys. 35 (2002) 249.

[434] A.C.A. Muller, K.L. Scrivener, A.M. Gajewicz, P.J. McDonald, Densification of C–S–H measured by ^{1}H NMR relaxometry, J. Phys. Chem. C 117 (2013) 403–412.

[435] A.C.A. Muller, K.L. Scrivener, A.M. Gajewicz, P.J. McDonald, Use of bench-top NMR to measure the density, composition and desorption isotherm of C–S–H in cement paste, Microporous Mesoporous Mater. 178 (2013) 99–103.

[436] A.C.A. Muller, K.L. Scrivener, A reassessment of mercury intrusion porosimetry by comparison with ^{1}H NMR relaxometry, Cement Concr. Res. 100 (2017) 350–360.

[437] G.H. Fuller, Nuclear spins and moments, J. Phys. Chem. Ref. Data 5 (1976) 835–1092.

[438] B. Walkley, A. Kashani, M.A. Sani, T.D. Ngo, P. Mendis, Examination of alkali-activated material nanostructure during thermal treatment, J. Mater. Sci. 53 (2018) 9486–9503.